공학박사학위논문

Development of a Real-Time Multi-rotor UAV Flight Simulation considering Aerodynamic Interference among the Rotors

로터 간의 공기역학적 간섭을 고려한 실시간 다중로터 UAV 비행 시뮬레이션 개발

2023년 8월

서울대학교 대학원

항공우주공학과

박 선 후

Development of a Real-Time Multi-rotor UAV Flight Simulation considering Aerodynamic Interference among the Rotors

로터 간의 공기역학적 간섭을 고려한 실시간 다중로터 UAV 비행 시뮬레이션 개발

지도교수 신 상 준

이 논문을 공학박사 학위논문으로 제출함

2023년 5월

서울대학교 대학원

항공우주공학과

박 선 후

박선후의 공학박사 학위논문을 인준함

2023년 7월

위 원 장 _____ 이 관 중 _____ (인)

부위원장 _____ 신 상 준 _____ (인)

위　　원 _____ 김 규 홍 _____ (인)

위　　원 _____ 박 재 상 _____ (인)

위　　원 _____ 조 해 성 _____ (인)

Abstract

A multirotor unmanned aerial vehicle (UAV) has advantages such as ease of manufacture and control. Due to those advantages, UAV has been widely used in the civil and military field. Recently, as the demand for operating UAV in urban is increased, the major usage of UAV is changed from personal hobbies to commercial operations which are related to urban infrastructure. However, it is not straightforward to operate UAV in urban because of the risks such as instability of flight and crash accidents due to the gust. For quantifying those risks, it is important to predict the transient behavior of UAV accurately. Thus, this dissertation is focused on the development of a real-time multirotor UAV flight simulation that is capable of ensuring the accuracy of dynamic behavior. The following considerations will be applied in the present flight simulation to enhance its prediction accuracy. First, the rotor aerodynamic analysis will be proposed to predict the aerodynamic loads of the rotor. The dynamic inflow approach and and rigid blade flapping will be considered in this rotor anaylsis. However, since the dynamic inflow approach was developed only for a single rotor, a novel formulation that is efficient and simple will be derived to evaluate the aerodynamic interference among the rotors. Then, the flight dynamics and the proposed rotor aerodynamics will be integrated for establishing the relevant flight simulation. Several constraints such as the rotational speed of the rotor and fuselage tilting angle limitation which are obtained by the trim anaylsis will be applied to the present flight simulation. Furthermore, a straightforward approach to estimate an unidentified gust will be developed and implemented for the present

simulation. The verification procedure for the present flight simulation will be performed step by step. The results obtained by the present rotor aerodynamics will be compared and validated by the experimental result and high-fidelity analysis for both an isolated rotor and multirotor configurations. Then, the components such as the controller, and dynamic characteristics will be evaluated. Based on this, the proposed flight simulation will be compared against the flight test. Particulary, the gust experiment which corresponds to the urban environment will be used to evaluate the present simulation. Further, the influence of the rigid blade flapping, aerodynamic interference, and gust intensity will be investigated and analyzed. It is found that a suitable rotor aerodynamic analysis is an important consideration to estimate the transient behavior of UAV.

Contents

List of Figures

List of Tables

1 Introduction

1.1 Background and Motivation

Multirotor-type unmanned aerial vehicle (UAV) is capable of performing vertical take-off and landing (VTOL) as well as trajectory flight tasks. The lift is generated by multiple rotors and it is varied by the rotational speed of the rotor. In addition, such UAV shows the simplicity of control and ease of fabrication. By those advantages, the multirotor UAV has been used in both military and civilian fields. Recently, owing to the increasing demand for the courier services or surveillance missions in an urban environment, the scope of the usage of multirotor UAV has expanded beyond personal hobbies rather to commercial operation and the construction of urban infrastructure. However, Federal Aviation Administration (FAA) established the regulation that the flight permission of UAV would be denied in populated districts (Ref. [1]). Thus, it is needed to obtain the certification to operate multirotor UAV in urban.

For that, UAV traffic management (UTM) Program (Ref. [2]) was initiated by NASA to operate multirotor UAV in urban. NASA suggested a protocol (Ref. [3]) to manage and quantify the associated potential risks to prevent casualties. Various types of risk were defined and proposed within that program, such as signal loss of positioning system, electrical system failure, and gust effect. Although those risks are

required to be regarded as equally important, it is particularly important to consider the influence of the gust on a UAV. In contrast to the rural area, the gust which is blown in urban shows complex stream features, such as vorticity and shear(Ref. [4]). In addition, the urban canyon (Refs. [5]-[6]) affects the increase of gust strength that may induce instability of flight or even crash accidents of UAV. Due to that risk, it is not straightforward to operate multirotor UAV in urban.

To overcome such difficulty, most of the existing studies for multirotor UAV were focused on the enhancement of the control performance (Refs. [7]-[8]). The nonlinear control approaches such as an L1 adaptive control (Ref. [9]) and sliding mode control based on the backstepping method (Ref. [10]) suggested and showed a good performance to alleviate the disturbance such as gust. Although those control approaches are required to improve the performance of multirotor UAV, an additional investigation for dynamic characteristics of multirotor UAV will be needed to guarantee the safety of UAV operations in urban. Owing to such necessity, the interest in the accuracy of flight simulation for multirotor UAV has been increased. Furthermore, NASA proposed the importance of the accuracy of flight simulation to quantify the possible risk in urban (Ref. [11]).

The relevant studies for multirotor UAV flight simulation will be investigated in the following sections.

1.2 Literature Review

1.2.1 Investigation for a rotor aerodynamics

The previous studies (Refs. [12, 13]) focused on the design of the controller of multirotor UAV by using the simple rotor aerodynamics approach. The relevant approach showed that both the thrust and torque of the rotor were proportional to the square of the rotational speed. Although such formulation were straightforward to be implemented in the flight simulation, it failed to predict the performance of the rotor due to the relative speed and fuselage tilting angle. In addition, that formulation was valid only for the hover. During the forward flight of the UAV, the rotors will experience relative speed which create an advancing and retreating side, leading to an imbalance in lift and non-uniform inflow. Furthermore, in contrast to the conventional rotorcraft, the rotor blade of the small UAV operates in the low-Reynolds number regime. Therefore, such approach based on the simple rotor aerodynamics will not be an appropriate method for obtaining an accurate flight simulation.

High-fidelity anaylsis for rotor aerdoynamics

For those limitations, computational fluid dynamic (CFD) approaches have been utilized to investigate the rotor aerodynamics of multirotor UAV. The characteristics of multirotor UAV in hover were investigated by Thibault et al. (Ref. [14]) and they used the lattice-Boltzmann method. Diaz and Yoon, (Ref. [15]) attempted to analyze the aerodynamic features of a quadrotor under the gust. They found that the

3

thrust of the rear rotor showed a decreased trend when the quadrotor experienced a gust. In addition, such a phenomenon was suggested by Misiorowski et al. (Ref. [16]). First, they analyzed the aerodynamic feature of an isolated rotor. Then the analysis for both the plus- and cross-shaped quadrotors was performed. They found that the thrust of the rearmost rotor for both configurations was reduced by 13%. Barcelos et al. (Ref. [17]) developed a potential flow-based wake methodology to predict the rotor aerodynamics of multirotor UAV. Although the result based on the wake approach was larger than that of the CFD estimation by Misiorowski, it was sufficient to estimate well the rotor aerodynamics. Based on those predictions, the high-fidelity analysis was suitable for capturing the complex flow feature and accurate aerodynamic loads. However, there exist several disadvantages to using high-fidelity analysis in flight simulation. First, such analysis may need a large computational time to obtain the result. Second, it is not straightforward to apply CFD for flight simulation directly. The relative speed and fuselage tilting angle will be varied at each time step. It is crucial to ensure mesh creation and convergence in CFD for each time interval due to the flow conditions that continuously vary. Furthermore, when the wake methodology is used, it will be necessary to take into account additional factors such as the size of the vortex core to enhance the precision of predictions. Therefore, using CFD or wake techniques for flight simulation would still be complicated, as stated in Ref. [84].

Low-fidelity anaylsis based on the blade element momentum theory

Due to such limitation of a high-fidelity anaylsis, the most investigations for multirotor UAV (Refs. [19, 20, 21, 22, 23, 24, 25]) attempted to use the blade element momentum

theory (BEMT). McCrink and Gregory (Ref. [26]) examined the variations in thrust and power coefficient during axial climb using BEMT and accounted for the impact of low Reynolds number. Shetty and Selig (Ref. [27]) empirically demonstrated the vortex ring state of a multirotor UAV rotor blade. In addition, they investigated the effect of the induced velocity. Theys et al. (Ref. [28]) performed a wind tunnel test to observe the trend of thrust, torque, and drag of an isolated rotor in forward flight conditions. They used the vortex lattice method (VLM) and BEMT to predict such a trend of an isolated rotor. Despite a significant difference in the drag results, both BEMT and VLM predictions were quite similar to the experimental results. However, the following reasons indicate that BEMT is not a sufficient method to be applied in flight simulations. First, the mathematical formulation of BEMT is only valid for both hover and axial flight, as stated in reference [29]. Furthermore, information on the linear inflow is required to analyze the forward flight. Second, the aerodynamic force and moment should be expressed in terms of an azimuthal angle, but BEMT can not provide those quantities in terms of an azimuthal angle. Therefore, to improve the accuracy of the flight simulation, it is essential to reinforce BEMT with an appropriate rotor aerodynamic analysis.

1.2.2 Aerodynamic interference among the rotors

In contrast to the conventional rotorcraft, the multirotor UAV shows unique phenomena such as the aerodynamic interference among the rotors. However, the low-fidelity approach such as BEMT cannot capture such interference. It is because BEMT was developed for the aerodynamics of an isolated rotor. Although high-fidelity analysis

is capable of capturing such interference, that analysis will not be appropriate to be implemented in flight simulation, which is mentioned in the previous sections. Thus, additional investigations to consider the aerodynamic interference among the rotors will be required to predict the accurate aerodynamic feature of the multirotor UAV. Furthermore, the aerodynamic interference among the rotors shows dominant features of noise and vibration issues (Ref. [30, 31, 32]). Due to those reasons, it is important to predict the noise level of multirotor UAV for urban operations.

Experimental investigation for the aerodynamic interference

Several experimental studies (Refs. [33]-[35]) have aimed to explore the aerodynamic interference among the rotors. Russell et al. (Ref. [36]) conducted a hover test on a multirotor UAV in a wind tunnel. The test showed that the thrust generated by an isolated rotor slightly increased, but the trend was similar to the result for a complete UAV, which had the other rotors nearby. By that experiment, the entire aerodynamic force of UAV was acquired, but the load of the individual rotors was not measured. To compensate for such an experimental facility, Russell and Conley (Ref. [37]) established the multirotor test bed which was capable of measuring the aerodynamic forces of an individual rotor. They proposed that the thrust of the rear rotor was lower than that of an isolated rotor during forward flight. In addition, a side-by-side configuration showed an increased thrust, when the hub location between the rotors was nearby. The aerodynamic interference of both plus- and cross-shaped quadrotors was investigated by Atte et al. (Ref. [38]). The result showed a similar trend obtained by Russell. The thrust of the rear rotors was smaller than that of an

isolated rotor. By those experimental investigations, the aerodynamic interference was significant when multirotor UAV performed forward flight. Although the experiment is capable of capturing the trend of aerodynamic interference, many experimental databases are required for the flight simulation. Due to that, it is not straightforward to use the approach based on the experiment for the implementation in the flight simulation.

Finite state-space inflow approaches for the aerodynamic interference

To overcome such limitations, the finite state-space inflow analysis has been used to consider aerodynamic interference among the rotors. Advanced Rotorcraft Technology (ART) proposed the augmentation (Ref. [39]) and reduced-order method (Refs. [40, 41]) using the high-fidelity analysis such as the free-vortex wake or viscous vortex particle method (VVPM). By those approaches, the aerodynamic interference of the coaxial rotor configuration was compared and validated. Rand et al. (Refs. [42, 43]) suggested the method based on the system identification which estimated the linear inflow parameter obtained by the result of a free-wake analysis. Keller et al. (Refs. [44, 45]) performed similar works and they implemented that approach to the flight dynamic simulation. Although such approaches have shown promising results for a coaxial rotor configuration, the result of the high-fidelity analysis would still be required to identify the interference among the rotors. Prasad et al. (Ref. [46]) and Kong et al. (Refs. [47]-[49]) proposed the pressure potential superposition inflow model (PPSIM) which was derived from the finite-state dynamic inflow. They added the real flow effect into PPSIM and it showed a good agreement with high-fidelity analysis (Ref. [50]). Furthermore, PPSIM was extended by Guner et al. (Refs.

7

[51]) and they proposed the velocity potential superposition inflow model (VPSIM). Although such approaches based on the finite state-space inflow showed a good agreement with high-fidelity analysis, most verifications were focused on the coaxial configuration. Due to that, there is still room for the validation for non-overlapping multirotor configurations such as a quadrotor.

Analytic approache based on the simple vortex theory

In addition to the aforementioned investigations, analytical approaches have been carried out to analyze the interference among the rotors using the simple vortex theory for application in the flight simulation. Luo et al. (Ref. [52]) proposed a simplified approach that combined the momentum theory and interference factors (Ref. [55]) to consider the mutual interference of a quadrotor UAV. That approach was validated against CFD results and showed a satisfactory correlation. Nguyen et al. (Ref. [53]) suggested a simple approach which was combined with the momentum theory and a simple horseshoe vortex. They performed an experiment and such experiment was compared against the simple approach. That approach was generalized as a matrix form for a multirotor UAV by Han et al. (Ref. [54]). The formulation proposed by Han was capable of considering an aerodynamic interference for arbitrarily UAV configuration. However, that approach was not suitable for flight simulations because a simple horseshoe vortex was assumed from a circular wing approximation (Ref. [29]). That approximation is not guaranteed when the advance ratio of the rotor is smaller than 0.1. For that reason, such simplified formulation showed a significant discrepancy compared with the experimental result (Ref. [53]). To overcome those

8

limitations, Guner and Prasad (Ref. [60]) proposed a combined approach which was based on the azimuthal vorticity distribution derived by Heyson (Ref. [57]). They attempted to validate the coaxial and tandem rotor configuration and such approach exhibited good agreement with both experimental results and high-fidelity analysis. Usov et al (Ref. [59]) proposed a combined approach that was based on Beddose's generalized wake. They investigated the non-overlapping (at a hub-to-hub separation distance $d > 2R$) tandem rotor configuration. Although those combined inflow approaches were capable of considering the aerodynamic interference, there was still room for evaluation and validation for a non-overlapping multirotor such as a quadrotor. Atte et al. (Ref. [38]) exhibited a unique interference trend of quadrotor configuration, which was not shown in the tandem configuration. First, the rear rotor thrust of the tandem configuration was smaller than that of the quadrotor when the rotor spacing was close to 2R. Second, the discrepancy between the isolated rotor and tandem configuration was larger than that for the quadrotor. Finally, in contrast to the quadrotor, it was not straightforward to find the correct trend from the result of the tandem rotor configuration. Furthermore, such an approach based on the combined inflow approach did not complete the validation of the aerodynamic interference for a small UAV. Due to that, it is necessary to identify the aerodynamic features of a non-overlapping multirotor.

1.2.3 Flight dynamics with the rotor aerodynamcis

Based on the following studies, the aerodynamic characteristics of the multirotor UAV have been investigated. However, there are still issues to be addressed for applying

the rotor aerodynamic in the flight simulation. In addition, it is needed to identify the effect of the gust when UAV operates in urban. Due to those requirements, relevant studies were performed to combine flight dynamics with rotor aerodynamics.

Flight simulation using the high-fideltiy anaylsis or experimental result

Sutherland et al.(Ref. [62]) attempted to identify the flow feature nearby a building based on CFD analysis. Then, the relevant flow result obtained by CFD was used for the flight simulation. However, that approach had the following limitations. First, a significant amount of time to obtain the flow field results around the buildings would still be required. In addition, the flight simulation suggested by Sutherland used a simplified rotor aerodynamics. Due to that, the flight simulation based on the database of the experiment was attempted. Foster and Hartman (Ref. [11]) developed a high-fidelity flight simulation. They performed the wind tunnel test for an isolated rotor. That result was converted into a look-up table and applied to flight simulation. Foster et al.(Ref. [63]) extended the test procedure of an isolated rotor to an entire multirotor UAV. They analyzed both forward and descending flight conditions to identify the aerodynamic feature of a multirotor UAV. Such results were used to improve the accuracy of the aforementioned high-fidelity flight simulation. Although the approach based on the experiment showed a good correction with experiment, that approach would also need a significant amount of time and effort to cover various flight situations. Further, the aerodynamic performance of the rotor was varied by the parameters such as the airfoil, built-in twist, and chord distribution in terms of the spanwise station. As mentioned in Sections 1.2.1, and 1.2.2, high-fidelity analysis or experiment approach will still need more effort to be applied in the flight simulation.

10

Combined approach with the low-fidelity rotor anaylsis

Due to those limitations, low-fidelity rotor analysis has been adopted for the flight simulation. Davoudi et al.(Ref. [64]) proposed the flight simulation which was coupled with BEMT. They investigated the gust effect using CFD and Dryden turbulence methodology (Ref. [65]). Using the result of the gust analysis, a significant discrepancy was observed between the simplified rotor aerodynamics and that predicted by BEMT. As a similar perspective, Sharsty et al.(Ref. [66]) suggested the concept of combining the flight dynamics and BEMT. They performed flight tests such as hover and forward flight and those results were compared with the relevant flight simulations. The comparison result for hover exhibited a consistent trend. However, the comparison result for the forward flight showed a considerable discrepancy between the experiments and simulations. Such result showed that BEMT would not be a proper method to predict the dynamic response of multirotor UAV due to the gust. In addition, although the previous studies tried to investigate such responses, those results were not compared with the experimental result with gust. In urban, the unique infrastructure such as urban canyons intensified the gust strength because of the venturi effect. Due to that effect, the strength of the gust would be greater than 8 m/s, particularly when a UAV passed through the venturi effect region (Ref. [67], [68]). However, the existing experiments (Refs. [9], [69], [70], [71], [96], [73]) were performed within the 2–6 m/s range of the gust. Therefore, it was important to evaluate and validate the rotor aerodynamics which was proper to predict the gust effect. Therefore, it will be required to verify the gust experiment to safely operate UAVs in an urban area.

1.3 Objectives and Scopes

As described in Sections 1.2.1 - 1.2.3, it is not straightforward to select an appropriate rotor aerodynamics analysis useful for UAV flight simulation. The analysis for the rotor aerodynamics should maintain accuracy, and it consumes reasonable computational time to obtain the aerodynamic load for simulation. In addition, it is important to verify the flight simulation by the experimental result for guaranteeing accuracy.

For that, this dissertation will focus on the development of a real-time multirotor UAV flight simulation considering aerodynamic interference among the rotors. To establish such flight simulation successfully, the analysis module which needs to enhance the accuracy is classified and shown in Fig. 1.1. Based on the hierarchy shown in Fig. 1.1, the major research scopes of this dissertation are listed as follows.

(a) The formulation for an isolated rotor aerodynamics which is a suitable method for flight simulation will be proposed. In addition, such formulation will be extended to consider the aerodynamic interference among the rotors (Refs. [74, 75]).

(b) The proposed rotor aerodynamics analysis will be integrated with the flight dynamics. To evaluate the accuracy of the flight simulation, the validation by the flight test will be performed (Refs. [76]).

(c) The proposed flight simulation will be compared and verified with the gust experiment result. Furthermore, the importance of the aerodynamic rotor analysis will be investigated and found in terms of intensity of the gust (Refs. [77, 78]).
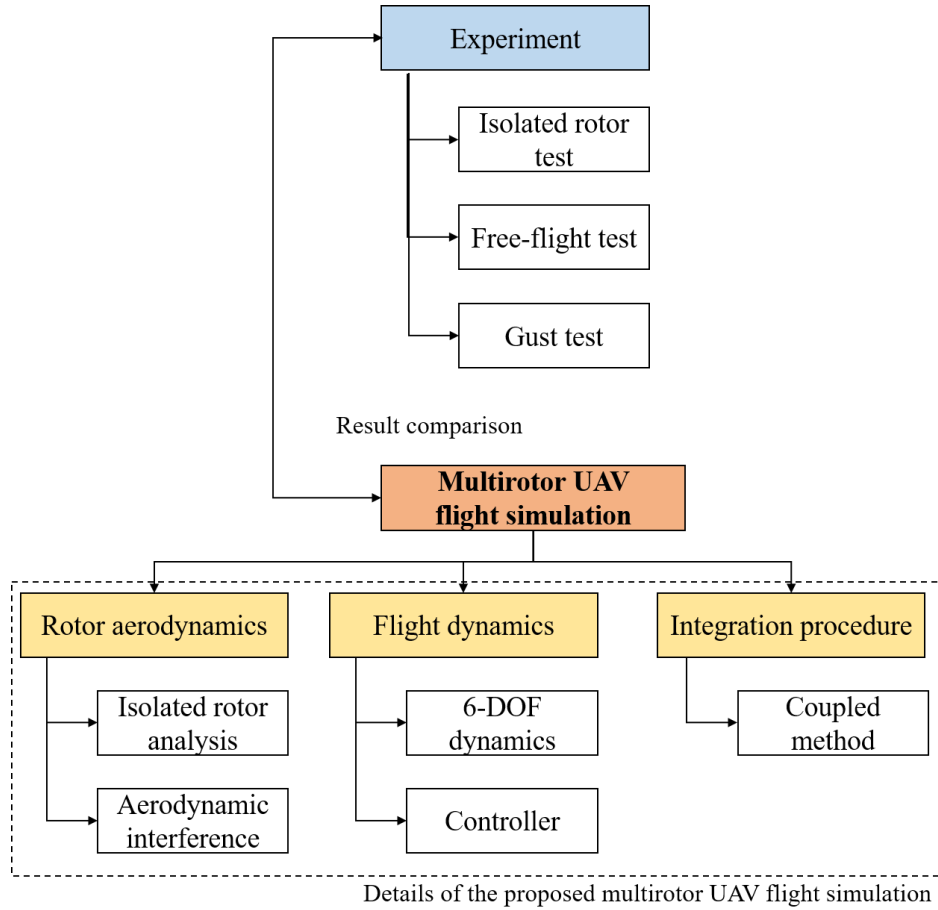
Figure 1.1   Hierarchy of the proposed multirotor UAV flight simulation

13

1.4   Outline of Dissertation

In this section, the outline of this dissertation is described as follows.

In Chapter 2, the rotor aerodynamics which is suitable to be applied in flight simulation will be proposed. The rotor aerodynamic analysis for an isolated rotor will be introduced and this formulation will be extended to consider aerodynamic interference among the rotors. The details of a novel approach will be introduced.

Chapter 3 will describe the present flight simulation for a multirotor UAV. The details of integration with the flight dynamics and rotor aerodynamics will be introduced. In addition, approaches such as trim analysis, system identification, and gust estimation will be presented to validate the present flight simulation systematically.

Chapter 4 will suggest the accuracy of the proposed rotor aerodynamics. The comparison for an isolated rotor under hover, climb, and forward flight conditions will be performed and validated by the experimental result. Furthermore, the relevant results for the aerodynamic interference among the rotors will be described for multirotor configuration which has no overlapping area. These results obtained by the present analysis will be compared against the experimental result and high-fidelity analysis.

In Chapter 5, the details of a systematic procedure will be introduced and validated by the experiment results of the target UAV. The results predicted by the present flight

simulation will be compared and validated against the free-flight test. In addition, the gust experiment that corresponds to urban gust conditions will be used to evaluate the credibility of the proposed simulation. Further investigations will be performed to find the dynamic characteristics of the target UAV.

Finally, the remarkable conclusion and recommended future works will be described in Chapter 6.

2 Rotor Aerodynamic Analysis considering Aerodynamic Interference

2.1 Formulation for an isolated rotor

In this section, brief introduction and limitation of BEMT will be presented. Then, an enhanced formulation for the flight simulation will be proposed.

2.1.1 Brief investigation of BEMT

BEMT, which stands for the blade element momentum theory, is a method that combines the blade element theory (BET) and momentum theory (Ref. [29]). The momentum theory cannot take into account the effect of the profile drag. To address this limitation, BET will be selected. The relevant description of BET is as follows. Two-dimensional lift and drag, as illustrated in Fig. 2.1 (a), will be obtained using the circulation theory. The perpendicular and tangential velocity components to the airfoil are denoted as U_p and U_T, respectively, while the radial velocity component is denoted as U_R, as shown in Fig. 2.1 (b). The sectional normal and tangential forces acting on the airfoil are combined with the momentum theory to obtain the equation expressed as follows:

$$dC_T = 4F\lambda(\lambda - \lambda_c)rdr$$

$$dC_T \cong \tfrac{1}{2}\sigma C_l r^2 dr = \tfrac{1}{2}\sigma(C_{l\alpha}(\theta - \phi))r^2 dr$$

$$F = \begin{cases} \frac{2}{\pi}\cos^{-1}(e^{-f_{root}}), f_{root} = \frac{N_b}{2}\frac{r}{(1-r)\phi} & \text{if } r < 0.5 \\ \\ \frac{2}{\pi}\cos^{-1}(e^{-f_{tip}}), f_{tip} = \frac{N_b}{2}\frac{1-r}{r\phi} & \text{if } r \geq 0.5 \end{cases}$$
<div style="text-align:right">(2.1)</div>

$$\lambda_c = \frac{-U_z}{\Omega R} = \frac{V_c}{\Omega R}, r = \frac{y}{R}, \sigma(r) = \frac{N_b c(r)}{\pi R}$$

The tip loss effect for both the blade root and tip is applied, and it is based on Prandtl tip loss function denoted by F. The non-dimensional span-wise position of the blade is represented by the parameter r, and the number of the blades is given by N_b. An iterative approach is employed to achieve convergence of the inflow values in Eq. 2.1. The aerodynamic forces and moments are expressed as functions of the azimuth angle Ψ.

$$U = \sqrt{U_P^2 + U_T^2 + U_R^2}$$

$$T = \frac{N_b}{2\pi}\int_0^{2\pi}\int_0^R dF_z \Psi d\Psi$$

$$H = \frac{N_b}{2\pi}\int_0^{2\pi}\int_0^R (dF_r \cos\Psi + dF_x \sin\Psi)d\Psi$$

$$Y = \frac{N_b}{2\pi}\int_0^{2\pi}\int_0^R (dF_r \sin\Psi - dF_x \cos\Psi)d\Psi$$
<div style="text-align:right">(2.2)</div>

$$Q = \frac{N_b}{2\pi}\int_0^{2\pi}\int_0^R rdF_x d\Psi$$

$$M_x = \frac{N_b}{2\pi}\int_0^{2\pi}\int_0^R (dM \cos\Psi + rdF_z \sin\Psi)d\Psi$$

$$M_y = \frac{N_b}{2\pi}\int_0^{2\pi}\int_0^R (dF_r \sin\Psi - dF_z \cos\Psi)d\Psi$$

BEMT can accurately predict the aerodynamic loads in both hover and axial flight conditions, as demonstrated by the experimental results (Refs. [19, 25, 26]). However, there exist certain limitations for applying BEMT to the flight simulation.

17

First, BEMT cannot predict the aerodynamic loads induced in forward flight due to an imbalance in lift and inflow. BEMT assumes that inflow is the same for all azimuth angles, based on the annulus disk assumption. Then, the aerodynamic loads obtained by BEMT will be an average result over one revolution which is expressed in Eq. 2.2. This suggests that the aerodynamic loads will be a quasi-steady quantity and additional dynamic analysis be needed for the flight simulation. Finally, the accuracy of drag prediction is significantly affected by the rigid blade flapping angle because the forward and sideward forces (H,Y) in Eq. 2.2 are considerably influenced by it (Ref. [79]). Therefore, it is necessary to consider the blade flapping which will improve the accuracy of drag prediction.
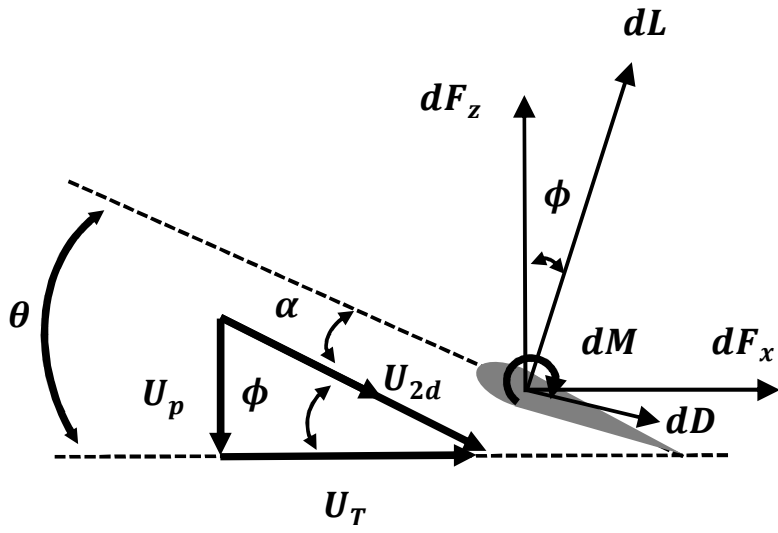
(a) Blade element
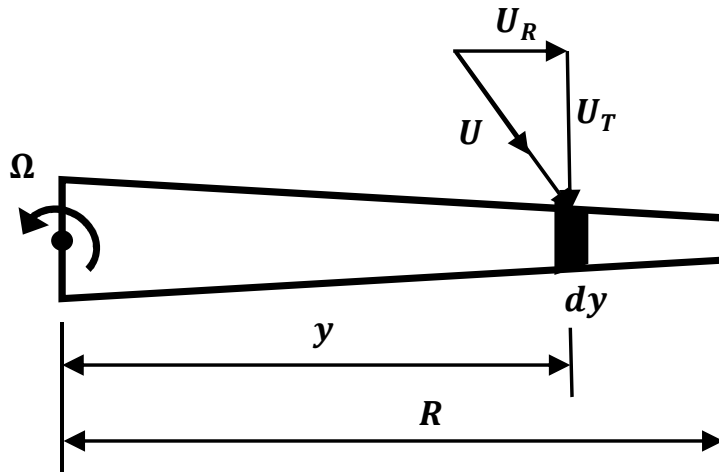
(b) Top view of the blade

Figure 2.1   Blade element aerodynamic load

2.1.2 Enhancement for the rotor aerodynamic analysis

The previous section outlined the limitations of using BEMT for the flight simulation. To overcome those limitations and improve the accuracy of aerodynamic analysis for the flight simulation, three proposed enhancements will be proposed as follows: (1) incorporating a dynamic inflow for forward flight, (2) accounting for the rigid blade flapping, and (3) estimating the aerodynamic load based on the azimuth angle. This section presents a rotor aerodynamic analysis using such three improvements, as shown in Fig. 2.2. The proposed analysis will be performed as follows. First, the angle of attack of the blade at the initial azimuth position is determined based on the induced inflow and flapping. This angle of attack will then be used as an input to BET to deduce the aerodynamic load. The load will finally be fed back to the dynamic inflow and rigid blade flapping module for the next step of the azimuth position. Such iterative process will be performed at each time step.

1) Dynamic inflow

The inflow approach used in the proposed analysis is based on the development of Pitt and Peters (Refs. [80, 81]), which was a well-established and widely used analysis in rotorcraft flight simulations. That approach was derived from the actuator–disk theory developed by Mangler (Ref. [82]). Despite the availability of more advanced methods such as CFD and VLM-based panel methods, the dynamic inflow approach proposed by Pitt and Peters remains popular due to its simplicity and relatively improved accuracy. As such, it has been adopted in many flight simulations (Ref. [84]), including the present study. Pitt and Peters utilized a pressure function to

determine the distribution at the rotor disk. The relevant formulation is expressed as follows:

$$P(\nu, \eta, \bar{\Psi}) = \sum_{n,m} P_n^m(\nu) Q_n^m(i\eta)[C_n^m cos(m\Psi) + D_n^m sin(m\Psi)] \qquad (2.3)$$

The symbols such as $\nu, \eta, \bar{\Psi}$ are ellipsoidal coordinates. Associated Legendre function of the first and second kind is represented as P_n^m and Q_n^m respectively. C_n^m and D_n^m are the constant coefficients and such terms were investigated by Pitt and Peters. Further details can be found in Ref. [83]. The inflow equation proposed by them is expressed in Eq. 2.4.

$$\lambda(r, \Psi) = \lambda_0 + \lambda_s r \sin(\Psi) + \lambda_c r \cos\Psi \qquad (2.4)$$

Using such equations, the following formulation is proposed and expressed as follows.

$$\overline{\overline{M}} \begin{bmatrix} \dot{\lambda_0} \\ \dot{\lambda_c} \\ \dot{\lambda_s} \end{bmatrix} + \hat{\overline{\overline{L}}}^{-1} \begin{bmatrix} \lambda_0 \\ \lambda_c \\ \lambda_s \end{bmatrix} = \begin{bmatrix} C_T \\ -C_L \\ -C_M \end{bmatrix} \qquad (2.5)$$

$\overline{\overline{M}}$ and $\hat{\overline{\overline{L}}}$ are the apparent mass and gain matrices to predict the inflow vector. C_T denotes the thrust coefficient. C_L and C_M denote the rolling and pitching moments, respectively. The details of $\hat{\overline{\overline{L}}}$ matrix is described in Eq. 2.6.

21

$$\hat{\bar{\bar{L}}} = \overline{LV}^{-1} = \begin{bmatrix} \frac{1}{2} & 0 & -\frac{15\pi}{64}\sqrt{\frac{1-\sin\alpha}{1+\sin\alpha}} \\ 0 & \frac{4}{1+\sin\alpha} & 0 \\ \frac{15\pi}{64}\sqrt{\frac{1-\sin\alpha}{1+\sin\alpha}} & 0 & \frac{4\sin\alpha}{1+\sin\alpha} \end{bmatrix} \tag{2.6}$$

where,

$$V_T = \sqrt{\lambda^2 + \mu^2}, \alpha = \tan^{-1}\frac{\lambda}{\mu}, V = \frac{\mu^2 + \lambda(\lambda + \lambda_i)}{V_T}$$

In the given equation, α refers to the angle of tilt of the disk, while both V_T and V are estimated using the momentum theory proposed by Glauert [85]. The mass matrix is based on the information of a conventional rotorcraft, but a modification of the matrix will be necessary to apply the concept to a UAV. This is mainly due to the varied rotational speed of the UAV rotor when compared to that of a typical helicopter. To resolve such issue, the unsteady momentum theory will be utilized, and the mass matrix will be altered by referring to the method proposed by Leishman [29].

$$\overline{M_{pitt}} = \begin{bmatrix} \frac{128}{75\pi} & & \\ & \frac{-16}{45\pi} & \\ & & \frac{-16}{45\pi} \end{bmatrix} \rightarrow \overline{M_{Fixed}} = \begin{bmatrix} \frac{8}{3\pi\Omega} & & \\ & \frac{-16}{45\pi\Omega} & \\ & & \frac{-16}{45\pi\Omega} \end{bmatrix} \tag{2.7}$$

2) Rigid blade flapping

An asymmetric lift will be generated when the rotor is operated in forward flight conditions. Although the blade of UAV is shorter and stiffer than that of a conventional rotorcraft, the rigid blade flapping will still occur. This phenomenon was observed

by Hoffmann et al. [86], who found that the flapping angle of a UAV blade was increased significantly with the wind speed. They measured the rigid flapping angle of a blade at a wind speed of 3 m/s and found it to be approximately 1.3°. However, BEMT analysis is quasi-steady and does not account for the flapping effect such as perturbation in thrust and an increase in drag, which may lead to inaccuracies in determining the aerodynamic forces and moments. To obtain the accurate results, the rigid blade flapping will need to be considered.

During forward flight, a blade will experience various forces such as the aerodynamic, inertial, and centrifugal forces, as illustrated in Figure 2.3. To account for this, an equivalent hinge offset is assumed, and the governing equation of the rigid blade flapping is expressed as follows.

$$\ddot{\beta}_f + \nu^2{}_{\beta_f}\Omega^2\beta_f = \frac{1}{\beta_f}\int_e^R (r-e)dF_z + \frac{k_\beta}{I_\beta}\beta_p \tag{2.8}$$

where,

$$I_\beta = \int_e^R (r-e)^2 m \, dr, \ S_{\beta_f} = \int_e^R (r-e)m \, dr, \ \nu_\beta = \sqrt{1 + \frac{eS_{\beta_f}}{I_{\beta_f}} + \frac{k_{\beta_f}}{I_{\beta_f}\Omega^2}}$$

ν_{β_f} and e are the non-dimensionalized flapping natural frequency and equivalent hinge offset. The pre-con angle of the rigid blade flapping and moment of inertia at the hinge are denoted as β_p and I_β, respectively. There exist two methods to obtain the soultion of Eq. 2.8: the time domain method and azimuth angle method. The time domain method uses dF_z obtained from BET directly. However, to simplify the equations, certain assumptions are added, such as assuming the blade is a uniform and slender beam, the twist angle of the blade is a first-order linear equation, and

23

using average values of the slope for the lift and chord length for each section. After applying these assumptions, Equation 2.8 will be summarized as follows.

$$\frac{\partial^2 \beta_f}{\partial \Psi^2} + \nu_{\beta_f}^2 \beta_f = \gamma M_\beta + \frac{\omega^2_{\beta_0}}{\Omega} \beta_p \tag{2.9}$$

where,

$$M_\beta = \frac{1}{\rho a c \Omega^2 R^4} \int_e^R (r-e) dFz, \ \gamma = \frac{\rho a c R^4}{I_b}$$

Since the pre-con angle of the rigid blade flapping is equal to zero for a UAV in this case, the term will be neglected. Based on that, Eq. 2.9 will be rearranged as follows.

$$\frac{\partial^2 \beta_f}{\partial \Psi^2} - \gamma \beta_{p_{dot}} \frac{\partial \beta_f}{\partial \Psi} + (\nu^2_{\beta_f} - \gamma \beta_p)\beta_f = \beta_{\theta_0} + \beta_{\theta_t w} + \beta_\lambda \tag{2.10}$$

where,

$$\left.\begin{aligned}
\beta_{\theta_0} &= [\tfrac{1}{8}r^4 + (\tfrac{\mu}{3}\sin\Psi - \tfrac{e}{6})r^3 + (\tfrac{1}{4}\mu^2\sin\Psi^2 - \tfrac{e}{2}\mu\sin(\Psi)r^2 - \tfrac{e\mu^2\sin\Psi^2}{2})r]_e^1 \theta_0 \\
\beta_{\theta_t w} &= [\tfrac{1}{10}r^5 + (\tfrac{\mu}{4}\sin\Psi - \tfrac{e}{8})r^4 + (\tfrac{1}{6}\mu^2\sin\Psi^2 - \tfrac{e}{3}\mu\sin(\Psi)r^3 - \tfrac{e\mu^2\sin\Psi^2}{4})r]_e^1 \theta_{tw} \\
\beta_\lambda &= -\tfrac{1}{2}\lambda[\tfrac{1}{3}r^3 + (\tfrac{1}{2}\mu\sin(\Psi) - \tfrac{e}{2})r^2 - e\mu\sin\Psi r]_e^1 \\
\beta_{p_{dot}} &= -\tfrac{1}{2}[\tfrac{1}{4}r^4 + (\tfrac{1}{3}\mu\sin(\Psi) - \tfrac{e}{3})r^3 - \tfrac{e\mu\sin\Psi r^2}{2}]_e^1 \\
\beta_p &= -\tfrac{1}{2}\mu\cos\Psi[\tfrac{1}{3}r^3 + (\tfrac{1}{2}\mu\sin(\Psi) - \tfrac{e}{2})r^2 - e\mu\sin\Psi r]_e^1
\end{aligned}\right\}$$

3) Blade element theory

In this section, the result obtained from the dynamic inflow and rigid blade flapping is combined into BET. The relevant equation is expressed as follows.

24

$$U_P(t, \Psi) = (\lambda_i + \lambda_c)\Omega R \cos(\beta_f) + r\dot{\beta}_f + \mu\Omega R \cos(\Psi)\cos(\beta_f) \Bigg\rbrace$$
$$U_T(t, \Psi) = \Omega R + \mu\Omega R \sin(\Psi)$$
$$dF_z(t, \Psi) = (dL\cos\Phi - dD sin\phi)\cos(\beta_f) \qquad (2.11)$$
$$dF_r(t, \Psi) = -dL\sin(\beta_f) + d\sin(\Gamma)$$

The induced inflow predicted by the dynamic inflow, denoted by λ_i (the first term of U_P), is affected by the rigid blade flapping angle β_f. Furthermore, the rotor tip-path-plane is affected in the perpendicular direction by $\dot{\beta}_f$, which will also affect U_P. The primary difference from BEMT is the modification of the force in the radial direction, as shown in Equation 2.12. In the absence of the blade flapping, the formulations will only consider the profile drag of the blade. However, when the rigid blade flapping is taken into account, a term such as $-dL\sin(\beta_f)$ will be added to the equation, allowing for additional forces to be considered. Therefore, Equation 2.2 can be re-expressed as follows.

$$T(t, \Psi) = \sum_{k=1}^{n} \int_0^R dF_z(t, \Psi)_{blade@k}$$
$$Q(t, \Psi) = \sum_{k=1}^{n} \int_0^R r dF_x(t, \Psi)_{blade@k}$$
$$H(t, \Psi) = \sum_{k=1}^{n} \int_0^R (dF_r(t, \Psi)\cos(\Psi) + dF_x(t, \Psi)\sin\Psi)_{blade@k}$$
$$Y(t, \Psi) = \sum_{k=1}^{n} \int_0^R (dF_r(t, \Psi)\cos(\Psi) - dF_x(t, \Psi)\sin\Psi)_{blade@k} \qquad (2.12)$$
$$M_x(t, \Psi) = \sum_{k=1}^{n} \int_0^R (dM(t, \Psi)\cos(\Psi) + r dF_z(t, \Psi))_{blade@k}$$
$$M_y(t, \Psi) = \sum_{k=1}^{n} \int_0^R (dM(t, \Psi)\sin\Psi - r dF_z(t, \Psi))_{blade@k}$$
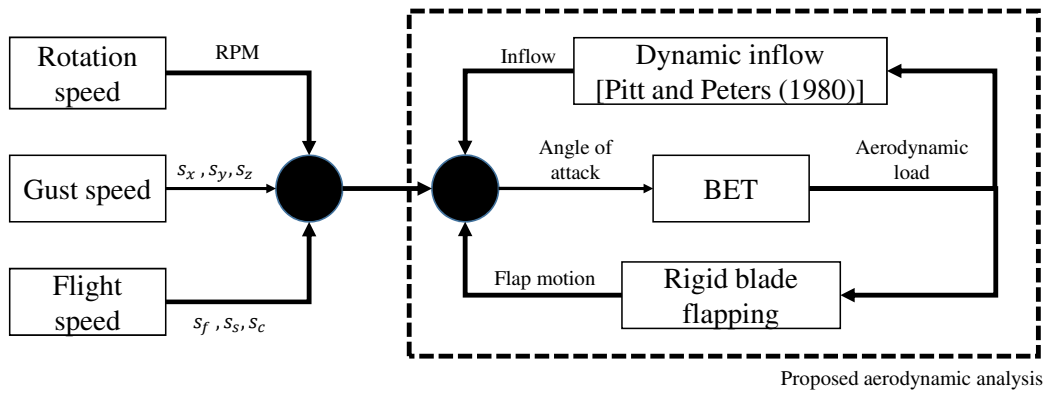
Figure 2.2   Proposed aerodynamic analysis for the UAV flight simulation
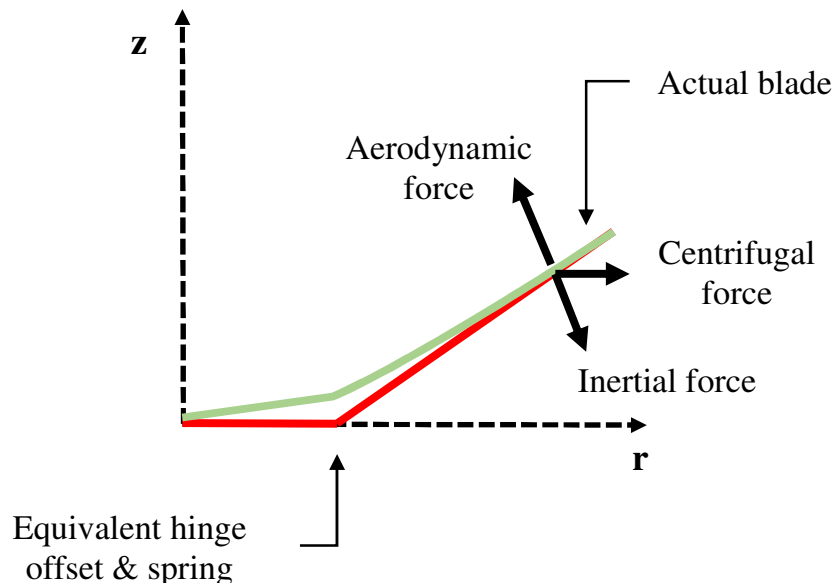
Figure 2.3   Rigid blade flapping

2.2 Extened formulation for the aerodynamic interference among the rotors

This section will present the existing analytical methods used for evaluating the aerodynamic interference. Afterward, a modified formulation based on the dynamic vortex tube approach will be introduced to consider the aerodynamic interference among non-overlapping rotors. The analytic formulation using the Taylor series will be suggested to reduce the computational complexity. Finally, the proposed formulation and dynamic inflow approach will be combined for the multirotor UAV flight simulation.

2.2.1 Existing analytical approaches using the simple vortex theory

Various analytical approaches that utilize the simple vortex theory have been suggested to account for the interference among the rotors (Refs. [52]-[54]). Those formulations use the Biot-Savart law to consider the aerodynamic interference. According to those approaches, the rotor wake is regarded as a simple horseshoe vortex. Han et al. (Ref. [54]) generalized such formulation and introduced an aerodynamic interference factor as follows:

$$k_i = \frac{v_{iP}}{v_{iO}} = \frac{1}{2}\Big[\frac{(\bar{y}_p + 1)(1 + \bar{x}_p cos(\pi - \chi)/\sqrt{\bar{x}_p{}^2 + (\bar{y}_p + 1)^2})}{(\bar{y}_p + 1)^2 + sin^2(\pi - \chi)\bar{x}_p{}^2} - \frac{(\bar{y}_p - 1)(1 + \bar{x}_p cos(\pi - \chi)/\sqrt{\bar{x}_p{}^2 + (\bar{y}_p - 1)^2})}{(\bar{y}_p - 1)^2 + sin^2(\pi - \chi)\bar{x}_p{}^2}\Big] \quad (2.13)$$

The coordinates of a point P are represented by non-dimensional coordinates $\bar{x}_p$ and $\bar{y}_p$ which are normalized by the rotor radius. The induced velocities at points O and P, which are the hub centers of each rotor, are represented by v_{iO} and v_{iP},

respectively. The skew angle is denoted by χ. A more detailed explanation can be found in Ref. [54]. Based on that method, it is straightforward to take into account the aerodynamic interference among the rotors. However, that method will not be appropriate for the flight simulation. The approach derived by Han uses the circular wing approximation, which is inaccurate for an advance ratio of less than 0.1. Furthermore, Eq. 2.13 only considers the uniform and steady features.

Guner and Prasad (Ref. [60]) presented an improved method to address the limitations of the previous approaches. Instead of a simple horseshoe vortex, they utilized an azimuthal vorticity distribution. They defined the inflow distribution, which was composed of two components: self-induced inflow (λ^S) and interference inflow (λ^I). The relevant formulation is expressed in Eq. 2.14. They used the interference formulation (Ref. [57]) which is expressed in Eq. 2.15. The vortex strength of the rotor which consists of a uniform and first-harmonic components are expressed as γ_0, γ_{1c}, and γ_{1s}. The locations affected by the rotor wake are expressed as Cartesian coordinates such as x, y, and z. The details of that approach is described in Ref. [60].

$$\lambda(\bar{r}, \Psi) = (\lambda_0^S + \lambda_0^I) + (\lambda_{1c}^S + \lambda_{1c}^I)\bar{r}cos(\Psi) + (\lambda_{1s}^S + \lambda_{1s}^I)\bar{r}sin(\Psi) \tag{2.14}$$

$$\lambda^I(\bar{r}, \Psi) = \frac{-1}{4\pi} \int_0^{2\pi} F(\Psi)\frac{1-(xcos(\Psi)+ysin(\Psi))+R_csin(\chi)cos(\Psi)}{[R_c+(cos(\Psi)-x)sin(\chi)+zcos(\chi)]R_c}d\Psi$$
$$F(\Psi) = \gamma_0 + \gamma_{1c}cos(\Psi) + \gamma_{1s}sin(\Psi), \tag{2.15}$$
$$R_c = \sqrt{1 + x^2 + y^2 + z^2 - 2(xcos(\Psi) + ysin(\Psi))}$$

28

Guner proposed an advanced approach that combined the momentum theory and Heyson formulation for interference inflow, using an azimuthal vorticity distribution to replace the simple horseshoe vortex. The method was shown to have good agreement with experimental results and high-fidelity analysis. In addition, Guner tried to expand that method applicable for the flight simulation (Ref. [60]). He attempted to use wake contraction for capturing the correct interference in the coaxial rotor configuration (Ref. [61]). While that approach is well-established for predicting the aerodynamic interference among the rotors, further evaluation and validation will be needed for general quadrotor configurations, as the aerodynamic trends differ between the tandem and quadrotor configurations (Ref. [38]). Therefore additional investigation will be required to expand those approaches for application in the flight simulation of a general multirotor configuration.

2.2.2 Aerodynamic interference based on the dynamic vortex tube

In the previous section, the existing analytical approaches for the aerodynamic interference among the rotors are investigated. In this section, the enhancements to enable those approaches to be applicable to multirotor flight simulation will be proposed. The following components such as the side-slip angle and rotational direction will be considered in the proposed formulation. Then, this formulation will be combined with the proposed rotor aerodynamics approach which is derived in Section 2.1.2.

Formulation of the aerodynamic interference among the rotors

The present formulation for considering the aerodynamic interference among the rotors adopts the concept of a dynamic vortex tube, as described in the previous studies (Refs. [87]-[89]). Prior to introducing the present formulation, several assumptions for the proposed approach will be listed. First, it is assumed that the vortices generated around the rotor blades wrap around a continuous vorticity tube, representing the outer surface of the rotor wake. This assumption allows for the induced inflow to be obtained using Biot-Savart law. Second, the rotor-bound circulation is assumed as a Fourier cosine-sine series, with a frequency of 1 per/rev. Third, to take into account the aerodynamic interference among the rotors, only the tip vortex will be used and the inner vortex not be considered. Fourth, the hypothetical rotors suggested by Zhao et al. (Refs. [87]-[88]) are used to consider the cyclic loading effect. Fifth, as the dynamic inflow assumes a rigid cylindrical wake, the distortion of the wake and vortex interaction among the wakes will be neglected. Finally, the proposed formulation does not consider the wake contraction and diffusion.

Although the proposed formulation is capable of predicting the aerodynamic interference among the rotors, it has limitations due to the low-fidelity approach. First, the accuracy of the proposed formulation is not ensured for hover and climb. This is because the cylindrical wake assumption used in this dissertation does not consider the effect of the aerodynamic interference for such flight status [57]. In addition, the proposed formulation does not take into account the effect of the obstacle behind the rotor. Finally, the prediction accuracy of the rotational direction effect [58] will depend on the configuration. As the proposed formulation neglects the interference

among the wake, the aerodynamic interference of the certain configuration which experiences significant interference among the wake may be not straightforward to be captured by the proposed approach. Thus, additional effort may be needed to use this formulation for the certain multirotor configuration correctly.

The wakes among the rotors are defined based on the dynamic vortex tube concept, as illustrated in Fig. 2.4(a). The tip vortex consists of the following two parts: the outer and inner vortex tubes, which represent the uniform and cyclic loading of the rotor, respectively. The outer vortex tube has a vorticity strength of γ_0, while the inner vortex tube has vorticity strengths of γ_{1c} and γ_{1s}. Furthermore, the side-slip angle θ_{xy} is included to account for the changes in the wake geometry caused by the sideward gusts. The velocity induced at point P_P is determined by the vorticity strength at point P_O of the k-th rotor, which is illustrated in Figure 2.4(b). The formulation for the aerodynamic interference will be established separately for the outer and inner vortex tubes in two stages.

First, the derivation of the outer vortex tube will be performed. To define the outer vortex tube, Eq. 2.16 will be used to define points P_O^0 and P_P^0. In Ref. [87], the definition of the vorticity strength is given, and based on this definition, the distribution of vorticity is expressed in Eq. 2.17.

$$
\boldsymbol{P_O^0} = \begin{bmatrix} \eta sin(\chi)cos(\theta_{xy}) + cos(\Psi_0(-1)^{r_c}) \\ \eta sin(\chi)sin(\theta_{xy}) + sin(\Psi_0(-1)^{r_c}) \\ -\eta cos(\chi) \end{bmatrix}, \ \boldsymbol{P_P} = \begin{bmatrix} r_1 cos(\Psi(-1)^{r_n}) + lcos(\alpha_{xy}) \\ r_1 sin(\Psi(-1)^{r_n}) + lsin(\alpha_{xy}) \\ 0 \end{bmatrix}
$$

$$(2.16)$$

$$\gamma_0 = \bar{\gamma}_0 \left[sin(\Psi_0(-1)^{r_c}), -cos(\Psi_0(-1)^{r_c}), 0 \right] \qquad (2.17)$$

In this equation, the wake length is denoted by η, and it is normalized by the radius of the k-th rotor. The angle between the rotors is represented by α_{xy}, while l is the distance between the centers of the rotors. Ψ_0 and Ψ correspond to the azimuthal angles of the k-th rotor vortex tube and the n-th rotor, respectively. It is important to take into account the rotational directions of the rotors because the sign of the vorticity strength may vary depending on the direction of the rotation. Hence, to account for the effect of the rotational direction, Eq. 2.16 will incorporate the variable r_c and r_n, where r_c and r_n denote the rotational directions of the k-th and n-th rotors, respectively. For the counterclockwise rotation, r_c and r_n will be zero. For the clockwise rotation, r_c and r_n will be one. The radial position of the n-th rotor is represented by r_1, which is normalized. The constant vorticity strength is represented by $\bar{\gamma}_0$. Using Eqs. 2.16 and 2.17, and Biot–Savart law, the induced velocity will be expressed as:

$$\begin{aligned} dV_z^0 &= \frac{\gamma_0 \times (P_P - P_O^0)}{(\sum (P_P - P_O^0)^2)^{3/2}}, V_z^0 = \frac{1}{4\pi} \int_0^{2\pi} \int_0^{\infty} dV_z^0 d\eta d\Psi_0 = \\ &\frac{\bar{\gamma}_0}{4\pi} \int_0^{2\pi} \int_0^{\infty} \frac{a_1^0 \eta + b_1^0}{(\eta^2 + a^0 \eta + b^0)^{3/2}} d\eta d\Psi_0 \end{aligned} \qquad (2.18)$$

where

$$cos \to c, \ sin \to s$$

$$a_1^0 = -c(\Psi_0(-1)^{r_c})s(\chi)c(\theta_{xy}) - s(\Psi_0(-1)^{r_c})s(\chi)s(\theta_{xy})$$

$$b_1^0 = c((-1)^{r_c}\Psi_0)(lc(\alpha_{xy}) - c((-1)^{r_c}\Psi_0) + r_1c((-1)^{r_n}\Psi))$$

$$+s((-1)^{r_c}\Psi_0)(ls(\alpha_{xy}) - s((-1)^{r_c}\Psi_0) + r_1s((-1)^{r_n}\Psi))$$

$$a^0 = (2c((-1)^{r_c}\Psi_0)s(\chi)c(\theta_{xy}) + 2s((-1)^{r_c}\Psi_0)s(\chi)s(\theta_{xy}) - 2lc(\alpha_{xy})s(\chi)c(\theta_{xy})$$

$$-2ls(\alpha_{xy})s(\chi)s(\theta_{xy}) - 2r_1c((-1)^{r_n}\Psi)s(\chi)c(\theta_{xy}) - 2r_1s((-1)^{r_n}\Psi)s(\chi)s(\theta_{xy}))$$

$$b^0 = l^2 + r_1^2 - 2lc((-1)^{r_c}\Psi_0)c(\alpha_{xy}) - 2ls((-1)^{r_c}\Psi_0)s(\alpha_{xy}) - 2r_1c((-1)^{r_c}\Psi_0)c((-1)^{r_n}\Psi)$$

$$-2r_1s((-1)^{r_c}\Psi_0)s((-1)^{r_n}\Psi) + 2lr_1c((-1)^{r_n}\Psi)c(\alpha_{xy}) + 2lr_1s((-1)^{r_n}\Psi)s(\alpha_{xy}) + 1$$

The integral for $d\eta$ can be transformed as an analytical formulation (Ref. [90]) and it is described in Eq. 2.19. But for the azimuth angle Ψ_0, there will be no analytical solution (Ref. [57]). To address such limitation, Zhao (Ref. [87]) proposed an alternative solution by utilizing a Taylor series expansion to account for the skew angle and wake curvature up to the second order. However, that approach was only applicable for the small wake curvatures and near-zero skew angles.

$$\int_0^\infty \frac{a_1^0 \eta + b_1^0}{(\eta^2 + a^0\eta + b^0)^{3/2}} d\eta = f^0 = \frac{(2b_1^0 + 2a_1^0\sqrt{b^0})}{(2b^0 + a^0\sqrt{b^0})}, \quad V_z^0 = \frac{\bar{\gamma}_0}{4\pi}\int_0^{2\pi} f^0 d\Psi_0 \quad (2.19)$$

To reduce the computational time of flight simulation, it will be necessary to convert Eq. 2.19 into an analytical formulation. This is achieved by including the azimuth angle Ψ_0 as a variable in Taylor series, and selecting the multiple nominal locations to compensate for the limitations of the expansion. In this case, 12 nominal locations will be considered, as depicted in Fig. 2.5. Furthermore, since the difference

between the first- and second-order expansions is negligible in Eq. 2.19, the first-order
expansion will be used. As a result, Eq. 2.19 will be rewritten as follows:

$$V_z^0 = \frac{\bar{\gamma}_0}{4\pi} \int_0^{2\pi} f^0 d\Psi_0 = \frac{\bar{\gamma}_0}{4\pi} (\int_0^{\frac{\pi}{6}} f^0 d\Psi_0 + \int_{\frac{\pi}{6}}^{\frac{\pi}{3}} f^0 d\Psi_0 + \ldots + \int_{\frac{11\pi}{6}}^{2\pi} f^0 d\Psi_0) =$$
$$\frac{\bar{\gamma}_0}{4\pi} \sum_{k=1}^{12} f_{taylor}^{k,0}(r_1, \Psi)$$

(2.20)

$$f_{taylor}^{k,0} = -\frac{\pi(s(\chi+\theta_{xy}-K_4^{k,0})K_1^{k,0}-K_2^{k,0}+s(\chi+\theta_{xy}+K_4^{k,0})K_1^{k,0}-K_3^{k,0}+2)}{12(l^2-K_3^{k,0}-K_2^{k,0}+r_1^2+lr_1c(\alpha_{xy}-K_5^{k,0})2-s(\chi)(r_1c(\theta_{xy}-K_5^{k,0})-c(\theta_{xy}-K_4^{k,0})+lc(\alpha_{xy}-\theta_{xy}))K_1^{k,0}+1)}$$

(2.21)

where

$$K_1^{k,0} = \sqrt{l^2+c(\alpha_{xy}-K_5^{k,0})lr_12-2lc(\alpha_{xy}-K_4^{k,0})+r_1^2-2c(K_4^{k,0}-K_5^{k,0})r_1+1}$$

$$K_2^{k,0} = 2lc(\alpha_{xy}-K_4^{k,0}), \quad K_3^{k,0} = 2r_1c(K_4^{k,0}-K_5^{k,0}), \quad K_4^{k,0} = \frac{\pi(-1)^{rc}(2k-1)}{12}, \quad K_5^{k,0} = (-1)^{rn}\psi$$

Equation 2.20 divides the integral range into twelve parts, and each part is
expressed as the sum of Taylor series at a nominal azimuth angle. The number of the
nominal locations is represented by k. The formulation of Taylor series expansion is
described in more detail in Eq. 2.21.

The following step will involve developing a formulation for inner vortex tubes.
The process for deriving this formulation will be similar to that for the outer
vortex tube but will require additional factors to be taken into account. The inner
components are comprised of the following two vortex tubes, one with positive
vorticity strength and the other with negative strength, and its radius is half that
of the outer vortex tube. Based on these considerations, the relevant formulations

34

for the inner vortex tubes will be described as follows. Further explanations are summarized in Appendix:

$$
\begin{cases}
V_z^{1c+} = \frac{\gamma_{\bar{1}c}}{4\pi} \sum_{k=1}^{12} f_{taylor}^{k,1c+}(r_1, \Psi), & V_z^{1c-} = \frac{\gamma_{\bar{1}c}}{4\pi} \sum_{k=1}^{12} f_{taylor}^{k,1c-}(r_1, \Psi) \\
V_z^{1s+} = \frac{\gamma_{\bar{1}s}}{4\pi} \sum_{k=1}^{12} f_{taylor}^{k,1s+}(r_1, \Psi), & V_z^{1s-} = \frac{\gamma_{\bar{1}s}}{4\pi} \sum_{k=1}^{12} f_{taylor}^{k,1s-}(r_1, \Psi)
\end{cases}
\tag{2.22}
$$

The total induced velocity, which is induced by the aerodynamic interference among the rotors, is expressed in Eq. 2.23 based on Eqs. 2.20 and 2.22.

$$
V_z^{it} = V_z^0 + V_z^{1c+} + V_z^{1c-} + V_z^{1s+} + V_z^{1s-}
\tag{2.23}
$$

Integration into the dynamic-inflow-based rotor aerodynamics analysis

This section describes the integration of the proposed interference formulation into a dynamic inflow-based rotor aerodynamic analysis. To achieve this, modifications to the dynamic inflow analysis derived in Section 2.1.2 are required to account for the rotational direction and side-slip angle. The dynamic inflow approach, such as Pitt-Peters method, was developed for the counterclockwise (CCW) rotating frame only. Thus, it needs to be validated for a clockwise (CW) rotating frame. To address that, an assumption will be made based on the previous investigation (Ref. [91]) that showed a similar magnitude for the sectional thrust in both CCW and CW rotors. That result suggested that the time lag and gain matrices of the dynamic inflow woulds not need to be modified. However, since the thrust distribution is axis-symmetric, an additional sign will be included to consider the rotational direction. Additionally, the angle of the wind, expressed as Ψ_{wind}, will be included to account

for the side-slip effect in the dynamic inflow. The modified dynamic inflow equation is expressed in Eq. 2.24.

$$\lambda(r, \Psi) = \lambda_0 + \lambda_c r \cos((-1)^{r_c}\Psi - \Psi_{wind}) + \lambda_s r \sin((-1)^{r_c}\Psi - \Psi_{wind}) \quad (2.24)$$

where

$$\Psi_{wind} = tan^{-1}(\frac{\mu_y}{\mu_x})$$

To represent Equation 2.23 in the form of a three-state inflow, several steps will bes taken. First, the rotor-bound circulation is defined. Equation 2.23 is based on the dynamic vortex tube proposed by Zhao (Ref. [87]). The mean-bound circulation of the rotor is defined as the bound circulation of the rotor in Equation 2.25, denoted as $\bar{\Gamma}_0$. The bound circulation of the rotor varies longitudinally and laterally, denoted as $\bar{\Gamma}_{1c}$ and $\bar{\Gamma}_{1s}$, respectively. Zhao suggested the strength of the vortex tube defined in Equation 2.26 by using Equation 2.25.

$$\bar{\Gamma}(\Psi) = \bar{\Gamma}_0 + \bar{\Gamma}_{1c}cos(\Psi) + \bar{\Gamma}_{1s}sin(\Psi) \quad (2.25)$$

$$\begin{bmatrix} \bar{\gamma}_0 \\ \bar{\gamma}_{1c} \\ \bar{\gamma}_{1s} \end{bmatrix} = \bar{\bar{V}}^{-1} \begin{bmatrix} \bar{\Gamma}_0 \\ \bar{\Gamma}_{1c} \\ \bar{\Gamma}_{1s} \end{bmatrix} = \bar{\bar{V}}^{-1} \begin{bmatrix} \frac{C_T}{1-\frac{3}{2}\mu^2} + \frac{3\mu C_L}{1-\frac{3}{2}\mu^2} \\ -3C_M \\ -\frac{3C_L}{1-\frac{3}{2}\mu^2} - \frac{\frac{3}{2}\mu C_T}{1-\frac{3}{2}\mu^2} \end{bmatrix} \quad (2.26)$$

In Eq. 2.26, μ is the advance ratio. The method to obtain this result is elaborated on in detail in Ref. [88]. Equation 2.26 will have a singularity point when the term $(1 - 3/2\mu^2)$ approaches zero. Although this term frequently appears in the vortex

theory, it will be disregarded when considering the axial wake vorticity (Ref. [55]).

The present formulation takes into account a tip vortex that includes the axial wake

vorticity. As a result, the factor $(1 - 3/2\mu^2)$ will be left out based on the physical

reasoning. Moreover, when the advance ratio is less than 0.6, the aerodynamic forces

will exhibit an insignificant discrepancy regarding this factor. Therefore, as a non-

overlapping multirotor cannot be operated as the high-speed forward flight, this

thesis will incorporate that factor. Using the orthotropic properties of trigonometric

functions, Eq. 2.27 will represent the three-state inflow.

$$
\begin{cases}
\lambda_0^{it} = \dfrac{1}{\pi} \int_0^{2\pi} \int_0^1 V_z^{it} r_1 dr_1 d\psi \\
\lambda_{1c}^{it} = \dfrac{4}{\pi} \int_0^{2\pi} \int_0^1 V_z^{it} r_1^2 cos(\psi) dr_1 d\psi \\
\lambda_{1s}^{it} = \dfrac{4}{\pi} \int_0^{2\pi} \int_0^1 V_z^{it} r_1^2 sin(\psi) dr_1 d\psi
\end{cases}
\tag{2.27}
$$

The symbol λ_0^{it} represents the average inflow component, while the cyclic com-

ponents are indicated by λ_{1c}^{it} and λ_{1s}^{it}. To simplify the expression in Eq. 2.27, Eqs.

2.20 to 2.23 will be inserted into it. Beyond this substitution, the formulation will

be expressed in Eq. 2.28.

37

$$\left\{ \begin{array}{l} \lambda_{0,0}^{it} = \frac{\bar{\gamma_0}}{4\pi^2} \int_0^{2\pi} \int_0^1 \sum_{k=1}^{12} f_{taylor}^{k,0} r_1 dr_1 d\psi = \bar{\gamma_0} f_{0,0} \\[2mm] \lambda_{0,1c}^{it} = \frac{\bar{\gamma_0}}{\pi^2} \int_0^{2\pi} \int_0^1 \sum_{k=1}^{12} f_{taylor}^{k,0} r_1^2 c(\psi) dr_1 d\psi = \bar{\gamma_0} f_{0,1c} \\[2mm] \lambda_{0,1s}^{it} = \frac{\bar{\gamma_0}}{\pi^2} \int_0^{2\pi} \int_0^1 \sum_{k=1}^{12} f_{taylor}^{k,0} r_1^2 s(\psi) dr_1 d\psi = \bar{\gamma_0} f_{0,1s} \\[2mm] \lambda_{1c,0}^{it} = \frac{\bar{\gamma_{1c}}}{4\pi^2} \int_0^{2\pi} \int_0^1 (\sum_{k=1}^{12} f_{taylor}^{k,1c+} + \sum_{k=1}^{12} f_{taylor}^{k,1c-}) r_1 dr_1 d\psi = \bar{\gamma_{1c}} f_{1c,0} \\[2mm] \lambda_{1c,1c}^{it} = \frac{\bar{\gamma_{1c}}}{\pi^2} \int_0^{2\pi} \int_0^1 (\sum_{k=1}^{12} f_{taylor}^{k,1c+} + \sum_{k=1}^{12} f_{taylor}^{k,1c-}) r_1^2 c(\psi) dr_1 d\psi = \bar{\gamma_{1c}} f_{1c,1c} \quad (2.28) \\[2mm] \lambda_{1c,1s}^{it} = \frac{\bar{\gamma_{1c}}}{\pi^2} \int_0^{2\pi} \int_0^1 (\sum_{k=1}^{12} f_{taylor}^{k,1c+} + \sum_{k=1}^{12} f_{taylor}^{k,1c-}) r_1^2 s(\psi) dr_1 d\psi = \bar{\gamma_{1c}} f_{1c,1s} \\[2mm] \lambda_{1s,0}^{it} = \frac{\bar{\gamma_{1s}}}{4\pi^2} \int_0^{2\pi} \int_0^1 (\sum_{k=1}^{12} f_{taylor}^{k,1s+} + \sum_{k=1}^{12} f_{taylor}^{k,1s-}) r_1 dr_1 d\psi = \bar{\gamma_{1s}} f_{1s,0} \\[2mm] \lambda_{1s,1c}^{it} = \frac{\bar{\gamma_{1s}}}{\pi^2} \int_0^{2\pi} \int_0^1 (\sum_{k=1}^{12} f_{taylor}^{k,1s+} + \sum_{k=1}^{12} f_{taylor}^{k,1s-}) r_1^2 c(\psi) dr_1 d\psi = \bar{\gamma_{1s}} f_{1s,1c} \\[2mm] \lambda_{1s,1s}^{it} = \frac{\bar{\gamma_{1s}}}{\pi^2} \int_0^{2\pi} \int_0^1 (\sum_{k=1}^{12} f_{taylor}^{k,1s+} + \sum_{k=1}^{12} f_{taylor}^{k,1s-}) r_1^2 s(\psi) dr_1 d\psi = \bar{\gamma_{1s}} f_{1s,1s} \end{array} \right.$$

The inflow component λ_0^{it} is comprised of the following three different components: $\lambda_{0,0}^{it}$, $\lambda_{1c,0}^{it}$, and $\lambda_{1s,0}^{it}$, all of which contain the mean vortex strength $\bar{\gamma_0}$ obtained from the bound circulation of the k-th rotor as defined in Eq. 2.26. The two other components, λ_{1c}^{it} and λ_{1s}^{it}, also have three components each, denoted by $\bar{\gamma_{1c}}$ and $\bar{\gamma_{1s}}$, respectively. These components are simplified and represented by the symbols $f_{0,0}$, $f_{0,1c}$, $f_{0,1s}$, $f_{1c,0}$, $f_{1c,1c}$, $f_{1c,1s}$, $f_{1s,0}$, $f_{1s,1c}$, and $f_{1s,1s}$. To obtain a straightforward form of Eq. 2.27, Eq. 2.26 can be substituted into Eq. 2.28, yielding the following formulation:

$$\boldsymbol{\lambda^{it}}_{k \to n} = \begin{bmatrix} \lambda_0^{it} \\ \lambda_{1c}^{it} \\ \lambda_{1s}^{it} \end{bmatrix}_{k \to n} = \overline{\overline{V}}_{k^{th}}^{-1} \overline{\overline{L_{int}}} \begin{bmatrix} C_T \\ -C_L \\ -C_M \end{bmatrix}_{k^{th}} \quad (2.29)$$

where,

$$\overline{\overline{L_{int}}} = \overline{\overline{L_{0,int}}} + \overline{\overline{L_{1c,int}}} + \overline{\overline{L_{1s,int}}}$$

$$\overline{\overline{L_{0,int}}} = \begin{bmatrix} \frac{f_{0,0}}{1-\frac{3}{2}\mu^2} & \frac{-3\mu f_{0,0}}{1-\frac{3}{2}\mu^2} & 0 \\[2mm] \frac{f_{0,1c}}{1-\frac{3}{2}\mu^2} & \frac{-3\mu f_{0,1c}}{1-\frac{3}{2}\mu^2} & 0 \\[2mm] \frac{f_{0,1s}}{1-\frac{3}{2}\mu^2} & \frac{-3\mu f_{0,1s}}{1-\frac{3}{2}\mu^2} & 0 \end{bmatrix}, \quad \overline{\overline{L_{1c,int}}} = \begin{bmatrix} 0 & 0 & 3f_{1c,0} \\[2mm] 0 & 0 & 3f_{1c,1c} \\[2mm] 0 & 0 & 3f_{1c,1s} \end{bmatrix},$$

$$\overline{\overline{L_{1s,int}}} = \begin{bmatrix} -\frac{3}{2}\mu f_{1s,0} & 3f_{1s,0} & 0 \\[2mm] -\frac{3}{2}\mu f_{1s,1c} & 3f_{1s,1c} & 0 \\[2mm] -\frac{3}{2}\mu f_{1s,1s} & 3f_{1s,1s} & 0 \end{bmatrix}$$

Using Equation 2.29, the interference inflow $\boldsymbol{\lambda^{it}}$ will be derived. For applying this formulation to the dynamic inflow, the following formulation will be defined as follows:

$$\boldsymbol{\lambda^n} = \boldsymbol{\lambda^{n_s}} + \boldsymbol{\lambda^{it}}, \ \boldsymbol{\dot{\lambda}^n} = \boldsymbol{\lambda^{\dot{n}_s}} \ \rightarrow \boldsymbol{\lambda^{n_s}} = \boldsymbol{\lambda^n} - \boldsymbol{\lambda^{it}} = \boldsymbol{\lambda^n} - \overline{\overline{V}}_{k^{th}}^{-1} \overline{\overline{L_{int}^{kn}}} \ \overline{\overline{V}}_{k^{th}} \ \overline{\overline{L_{in}^{kk}}}^{-1} \boldsymbol{\lambda^k} \quad (2.30)$$

The self-induced inflow of the n-th rotor is represented by $\boldsymbol{\lambda^{n_s}}$ and it is predicted using the dynamic inflow equation. The total induced inflow of the n-th rotor, denoted by $\boldsymbol{\lambda^n}$, is the sum of the self-induced inflow and the interference inflow generated by the k-th rotor. In this derivation, the time delay in the interference inflow is not taken into account, and the derivative terms of the self-and resultant-induced inflows are assumed to be the same. While neglecting the time delay may affect the transient response of the rotor aerodynamics, the behavior of rotor aerodynamics will be mainly influenced by the gain matrix. If consideration of such response is

39

required, an effective form suggested by Guner (Ref. [60]) will address this issue. By using this relationship, the self-induced inflow of the n-th rotor will be expressed in terms of $\boldsymbol{\lambda^n}$ and $\boldsymbol{\lambda^k}$. To apply this equation to the multiple number of the rotors, a decoupled matrix form is defined as follows:

$$
\begin{bmatrix}
\overline{\overline{M^{11}}} & 0 & \cdots & 0 \\
0 & \overline{\overline{M^{22}}} & \cdots & 0 \\
\vdots & \vdots & \overline{\overline{M^{kk}}} & \vdots \\
0 & 0 & \cdots & \overline{\overline{M^{NN}}}
\end{bmatrix}
\begin{bmatrix}
\dot{\boldsymbol{\lambda}}^{1_s} \\
\boldsymbol{\lambda}^{2_s} \\
\vdots \\
\boldsymbol{\lambda}^{N_s}
\end{bmatrix}
+
\begin{bmatrix}
\overline{\overline{L^{11}}} & 0 & \cdots & 0 \\
0 & \overline{\overline{L^{22}}} & \cdots & 0 \\
\vdots & \vdots & \overline{\overline{L^{kk}}} & \vdots \\
0 & 0 & \cdots & \overline{\overline{L^{NN}}}
\end{bmatrix}
\begin{bmatrix}
\boldsymbol{\lambda}^{1_s} \\
\boldsymbol{\lambda}^{2_s} \\
\vdots \\
\boldsymbol{\lambda}^{N_s}
\end{bmatrix}
=
\begin{bmatrix}
\boldsymbol{C}^1_{T,L,M} \\
\boldsymbol{C}^2_{T,L,M} \\
\vdots \\
\boldsymbol{C}^N_{T,L,M}
\end{bmatrix}
$$
(2.31)

N represents the number of the rotors. As Eq. 2.31 only takes into account the self-induced inflow state, aerodynamic interference will not be factored in. To incorporate the aerodynamic interference in the equation for the multiple number of the rotors, the self-induced inflow state in Eq. 2.31 will be redefined in terms of $\boldsymbol{\lambda^n}$ and $\boldsymbol{\lambda^k}$ as defined in Eq. 2.30. Thus, the generalized matrix expression that considers the aerodynamic interference will be represented by Eq. 2.32.

$$
\begin{bmatrix}
\overline{\overline{M^{11}_{in}}} & 0 & \cdots & 0 \\
0 & \overline{\overline{M^{22}_{in}}} & \cdots & 0 \\
\vdots & \vdots & \overline{\overline{M^{kk}_{in}}} & \vdots \\
0 & 0 & \cdots & \overline{\overline{M^{NN}_{in}}}
\end{bmatrix}
\begin{bmatrix}
\dot{\boldsymbol{\lambda}}^{1} \\
\boldsymbol{\lambda}^{2} \\
\vdots \\
\boldsymbol{\lambda}^{N}
\end{bmatrix}
+
\begin{bmatrix}
\overline{\overline{L^{11}}} & \overline{\overline{L^{21}}} & \cdots & \overline{\overline{L^{N1}}} \\
\overline{\overline{L^{12}}} & \overline{\overline{L^{22}}} & \cdots & \overline{\overline{L^{N2}}} \\
\vdots & \vdots & \overline{\overline{L^{kn}}} & \vdots \\
\overline{\overline{L^{1N}}} & \overline{\overline{L^{2N}}} & \cdots & \overline{\overline{L^{NN}}}
\end{bmatrix}
\begin{bmatrix}
\boldsymbol{\lambda}^{1} \\
\boldsymbol{\lambda}^{2} \\
\vdots \\
\boldsymbol{\lambda}^{N}
\end{bmatrix}
=
\begin{bmatrix}
\boldsymbol{C}^1_{T,L,M} \\
\boldsymbol{C}^2_{T,L,M} \\
\vdots \\
\boldsymbol{C}^N_{T,L,M}
\end{bmatrix}
$$
(2.32)

where

$$\begin{cases} k = n \rightarrow \overline{\overline{L^{kn}}} = \overline{\overline{L_{in}^{kk}}} \\ k \neq n \rightarrow \overline{\overline{L^{kn}}} = -\overline{\overline{V_{n^{th}}}} \, \overline{\overline{L_{in}^{nn}}}^{-1} \overline{\overline{V}}_{k^{th}}^{-1} \overline{\overline{L_{int}^{kn}}} \, \overline{\overline{V_{k^{th}}}} \, \overline{\overline{L_{in}^{kk}}}^{-1} \end{cases}$$

The gain matrix of the rotor inflow is expressed as $\overline{\overline{L^{kn}}}$. When k and n are the same, the original form of dynamic inflow will be inserted in the component of the matrix. However, when k and n are not the same, considering aerodynamic interference will become necessary. The interference among the rotors is suggested in the formulation in Eq. 2.32
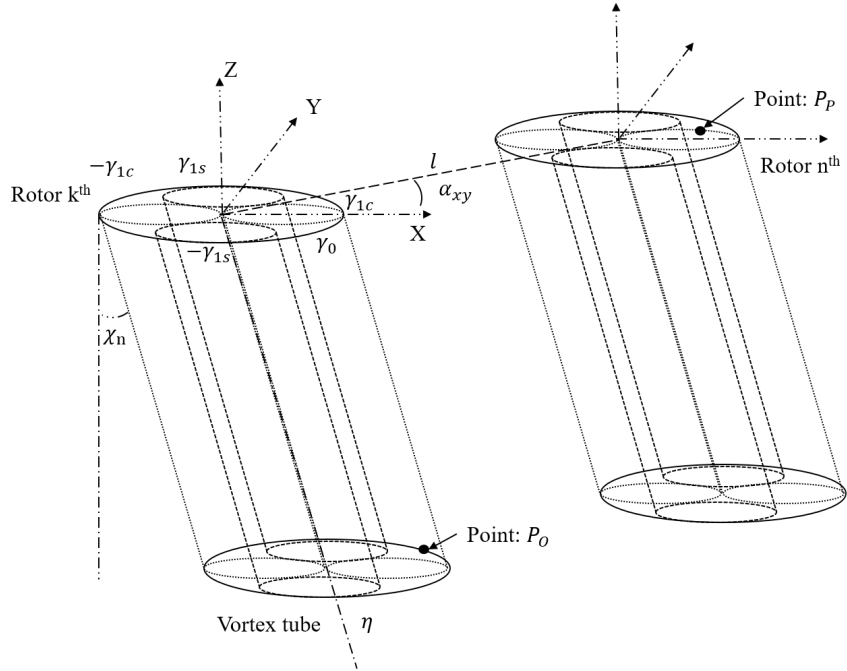
(a) Three-dimensional geometry of a dynamic vortex tube
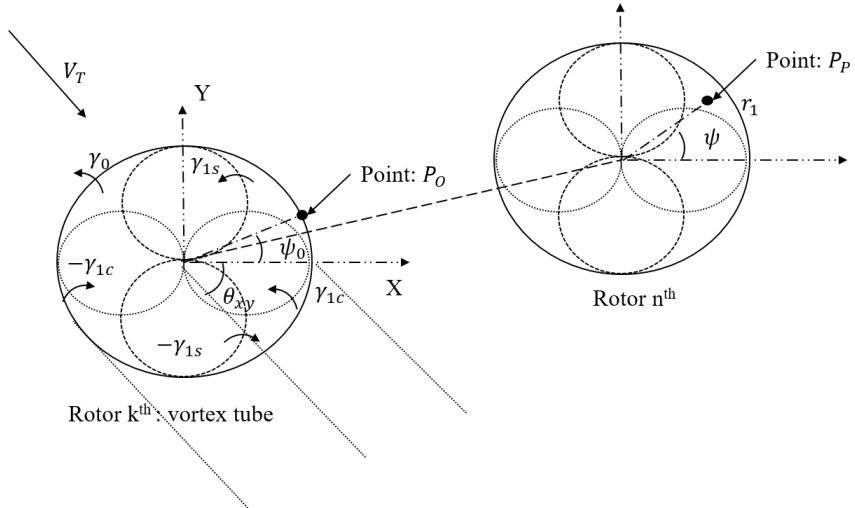
(b) Cross-sectional view of a dynamic vortex tube

Figure 2.4   Concept of a dynamic vortex tube for evaluating the aerodynamic interference among the rotors
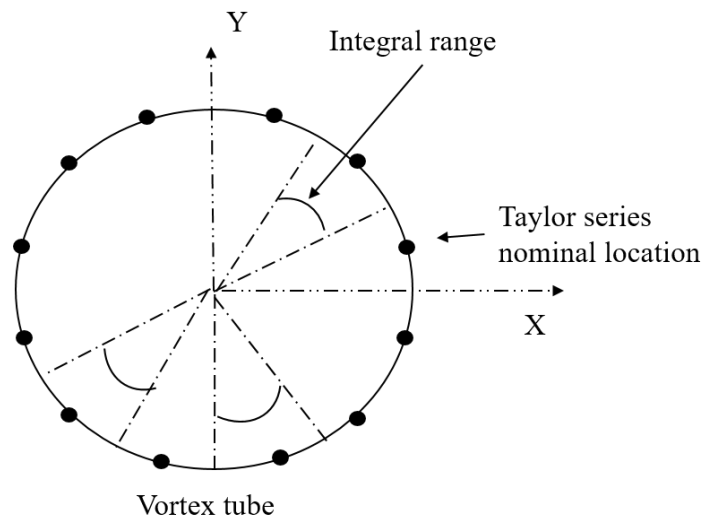
Figure 2.5 Nominal locations for Taylor series expansion

3 Establishment for the Multirotor UAV Flight Simulation

3.1 Mathmatical description of the flight dynamics

In this section, an introduction to the conventional UAV flight simulation will be presented. Then, a mathematical description of the present flight simulation with the proposed rotor aerodynamics analysis will be described.

3.1.1 limitation of the conventional UAV flight simulation

The various UAV flight simulations adopt the conventional method. That method was introduced by Hartman et al. (Ref. [92]) and has been adopted by numerous researchers (Refs. [93, 94, 95]). The conventional simulation employed Newton-Euler method, as described by Eq. 3.1, where $\{I\}$ is an inertial frame and $\{B\}$ is the fuselage frame at the center of gravity (CG) of UAV.

$$
\left.
\begin{aligned}
\dot{V}_B + \Omega_I \times V_B &= \frac{G_B}{m} + \frac{F_{Rotor}}{m} + \frac{F_{fuselage-aero}}{m} \\
\dot{H}_B + \Omega_I \times H_B &= M_{Rotor} + M_{gy}
\end{aligned}
\right\}, \tag{3.1}
$$

44

$$\mathbf{\Omega_I} = \boldsymbol{\omega_B} = \begin{bmatrix} p \\ q \\ r \end{bmatrix}, \mathbf{V_B} = \begin{bmatrix} u \\ v \\ w \end{bmatrix}, \mathbf{H_B} = \begin{bmatrix} \overline{\overline{I}} \end{bmatrix} \boldsymbol{\omega_B} \qquad (3.2)$$

$$\mathbf{M_{gy}} = \mathbf{H_{mI}} = \mathbf{\Omega_I} \times \mathbf{H_{mB}}, \mathbf{H_{mB}} = \begin{bmatrix} \overline{\overline{J_m}} \end{bmatrix} \boldsymbol{\omega_{mB}}, \omega_{mB} = \begin{bmatrix} 0 \\ 0 \\ \omega_m \end{bmatrix}. \qquad (3.3)$$

The velocity vectors of the UAV in the fuselage and inertia coordinates are repre-sented by $\mathbf{V_B}$ and $\mathbf{V_I}$, respectively. The gravitational force acting on the quadrotor in the fuselage frame is denoted by $\mathbf{G_B}$. The moments acting on UAV are represented by $\mathbf{H_i}$ and $\mathbf{H_B}$, while $\mathbf{M_{gy}}$ stands for the gyroscopic moment. The moment of inertia matrix of the rotor is represented by $\overline{\overline{J_m}}$, and the rotational speed of the rotor is expressed as $\boldsymbol{\omega_{mB}}$ in Eq. 3.3. The aerodynamic forces and moments, including the rotor thrust, torque, and fuselage aerodynamic forces, are denoted by $\mathbf{F_{Rotor}}$, $\mathbf{M_{Rotor}}$, and $\mathbf{F_{fuselage-aero}}$. The thrust and torque of the rotor are assumed to be proportional to the square of the rotor rotational speed.

However, the conventional simulation suggested by Hartman (Ref. [92]) has some limitations. The rotor aerodynamic analysis used in the conventional simulation did not take into account the variation of aerodynamic loads due to the flight speed or fuselage tilting attitude. Such analysis is only suitable for hover and will not be appropriate for a forward flight condition. Due to that, the accuracy of the convetional simulation may be decreased when UAV performs forward flight condition.

45

In addition, that inaccuracy will lead a significant discrepancy in the trim analysis and may produce unrealistic results.

3.1.2 Flight dynamics combined with the present rotor aerodynamics

In the previous section, the drawbacks of the conventional flight simulation proposed by Hartman were described. This section proposes an integrated flight dynamics approach that takes into account the proposed aerodynamics considering aerodynamic interference among the rotors. To achieve this, the reference frames will be defined. Furthermore, additional considerations such as fuselage aerodynamics and trim approach will be described. Finally, an integration procedure between the flight dynamics and proposed rotor aerodynamics will be attempted.

Frame of reference description

As previously mentioned in Section 3.1.1, most studies on a multirotor UAV have utilized the rigid body dynamics (Ref. [96]). Those studies have mainly employed two frames of reference: the inertial frame $\{I\}$ and the fuselage frame $\{B\}$. However, to account for the rotor aerodynamics in a multirotor UAV, an additional reference frame will be necessary. As illustrated in Fig. 3.1, the rotor hub $\{H\}$ and blade $\{b\}$ frames have been added for both clockwise (CW) and counterclockwise (CCW) directions. Due to the difference in the distribution of the rotor inflow depending on the rotational direction, both CW and CCW frames of reference have been defined. The transformation matrices between the frames of reference are explained in Eqs. 3.4- 3.7:

$$(\boldsymbol{V_H})_i = (\overline{\overline{T_B^H}})_i \ \overline{\overline{T_I^B}} \boldsymbol{V_I}, \ (\boldsymbol{V_b})_i = (\overline{\overline{T_H^b}})_i \ (\overline{\overline{T_B^H}})_i \ \overline{\overline{T_I^B}} \boldsymbol{V_I}, \qquad (3.4)$$

$$\begin{cases} \overline{\overline{T_I^B}} = \begin{bmatrix} c(\psi)c(\theta) & -s(\psi)c(\phi) + c(\psi)s(\theta)s(\phi) & s(\psi)s(\phi) + c(\psi)s(\theta)c(\phi) \\ s(\psi)c(\theta) & c(\psi)c(\phi) + s(\psi)s(\theta)s(\phi) & -c(\psi)s(\phi) + s(\psi)s(\theta)c(\phi) \\ -s(\theta) & c(\theta)s(\phi) & c(\theta)c(\phi) \end{bmatrix}, \\[2em] \overline{\overline{R_I^B}} = \begin{bmatrix} 1 & t(\theta)s(\phi) & t(\theta)c(\phi) \\ 0 & c(\phi) & -s(\phi) \\ 0 & \frac{s(\phi)}{c(\theta)} & \frac{c(\phi)}{c(\theta)} \end{bmatrix} \end{cases}$$

$$(3.5)$$

$$(\overline{\overline{T_B^H}})_{i \ (i=1,3)} = \begin{bmatrix} c(\pi) & s(\pi) & 0 \\ -s(\pi) & c(\pi) & 0 \\ 0 & 0 & 1 \end{bmatrix}, (\overline{\overline{T_B^H}})_{i \ (i=2,4)} = \begin{bmatrix} c(\pi) & 0 & -s(\pi) \\ 0 & 1 & 0 \\ s(\pi) & 0 & c(\pi) \end{bmatrix}, \qquad (3.6)$$

$$(\overline{\overline{T_H^b}})_{i \ (i=1,3)} = \begin{bmatrix} c(\psi_i) & s(\psi_i) & 0 \\ -s(\psi_i) & c(\psi_i) & 0 \\ 0 & 0 & 1 \end{bmatrix}, (\overline{\overline{T_H^b}})_{i \ (i=2,4)} = \begin{bmatrix} c(\psi_i) & s(\psi_i) & 0 \\ s(\psi_i) & -c(\psi_i) & 0 \\ 0 & 0 & -1 \end{bmatrix}, \qquad (3.7)$$

The velocity vectors, denoted as $\boldsymbol{V_H}$, $\boldsymbol{V_b}$, and $\boldsymbol{V_I}$, are defined in the rotor hub, blade, and inertial frame of reference, respectively. The index i is used to indicate the rotational direction, and the numbers 1 and 3 are used for CCW while 2 and 4

47

are used for CW. The transformation matrix from the inertial frame to the fuselage frame is denoted as $\overline{\overline{T_I^B}}$, while $(\overline{\overline{T_B^H}})i$ denotes the transformation matrix from the fuselage frame to the rotor hub frame. In addition, the transformation matrix from the rotor hub frame to the blade frame is $(\overline{\overline{TH^b}})_i$. The blade azimuthal angle is represented as ψ.

Fuselage aerodynamics

Regarding flight dynamics, the flight conditions are affected by both the aerodynamics of the rotor and the fuselage. In the case of a conventional rotorcraft (Ref. [97]), the drag and lift forces are defined using the angle of attack (AOA) of the entire rotorcraft and its equivalent flat plate area, as described in Eqs. 3.8 and 3.9.

$$\boldsymbol{F_{fuselage_{drag}}} = \begin{bmatrix} \frac{1}{2}\rho A_X D_{X_B}(\alpha, V_u)u^2 \\[2mm] \frac{1}{2}\rho A_Y D_{Y_B}(\alpha, V_v)v^2 \\[2mm] \frac{1}{2}\rho A_Z D_{Z_B}(\alpha, V_w)w^2 \end{bmatrix} \tag{3.8}$$

$$\boldsymbol{F_{fuselage_{lift}}} = \begin{bmatrix} \frac{1}{2}\rho A_X L_{X_B}(\alpha, V_u)u^2 \\[2mm] \frac{1}{2}\rho A_Y L_{Y_B}(\alpha, V_v)v^2 \\[2mm] \frac{1}{2}\rho A_Z L_{Z_B}(\alpha, V_w)w^2 \end{bmatrix} \tag{3.9}$$

There is a lack of aerodynamic formulations that are specifically designed for multirotor UAVs in the existing literature. Previous studies (Refs. [7, 10, 98]) attempted to develop an aerodynamic force expression for the fuselage using a linearized expression. Those approaches showed reasonable accuracy at lower flight speeds but decreased accuracy as the forward speed increased. To improve on those

approaches, the following method will be proposed. For UAV, only drag is considered as the fuselage generates very little lift. Russell et al. (Ref. [36]) conducted the aerodynamic experiments on various UAVs in a wind tunnel and found that the UAV fuselage scarcely generated lift. Schiano et al. (Ref. [99]) performed similar wind tunnel experiments and obtained similar results. Schiano found that when the fuselage tilting angle was within 20-30,°, the drag coefficient would remain constant. Equation 3.10 was derived using this relationship, and the coefficient was obtained from the flight results. K_E represents the fuselage drag coefficient.

$$\boldsymbol{F_{fuselage_{aero}}} = \begin{bmatrix} K_E u^2 \\ K_E v^2 \\ K_E w^2 \end{bmatrix} \tag{3.10}$$

Trim analysis

According to Ref. [97], trim is defined as the process of finding the control inputs necessary to maintain a rotorcraft in equilibrium. That process is well-established for a manned rotorcraft, but it is less important for UAV since they do not need to consider equilibrium during operation. Instead, the design of the nonlinear controller will be more critical. However, for UAV operating in urban regions, it will be essential to conduct a trim analysis to determine the physical limitations of the multirotor. There do not exist many studies available that discussed trim analysis for UAVs. Niemic and Gandhi (Ref. [100]) introduced a trim procedure for quadrotors that had a plus- or cross-shape. They conducted a trim analysis by considering the dynamic

49

inflow and steady-state solution. Based on such investigation, the present study will perform the trim analysis based on such method. It should be noted that the flight dynamics formulation of a quadrotor UAV is an under-determined system because it has six degrees of freedom but only four inputs. Due to that, multiple solutions may exist that can satisfy a specific flight condition. Additionally, it is challenging to account for nonlinear constraints in a general Jacobian-based trim analysis. Therefore, to address those difficulties, Austin et al. (Ref. [101]) suggested using an optimization approach to perform the trim analysis.

The present trim procedure utilizes Eq. 3.11 as an objective function with the design variables including the flight speed, angular speed, fuselage tilting attitude, and rotor rotational speed. The optimization process selects the "fmincon" function included in MATLAB and utilizes an interior-point algorithm based on Hessian approximation.

$$J = min[\sqrt{F_x^2 + F_y^2 + F_z^3 + M_x^2 + M_y^2 + M_z^2}] \qquad (3.11)$$

The forces and moments obtained from Eq. 3.1 when there is no linear or angular acceleration will be represented by F_x, F_y, F_z, M_x, M_y, and M_z. The rotational speed of the rotor is the variable being designed, and the forward speed is expressed in the global frame. This approach is used to obtain constraints within an operation, which are implemented in the present flight simulation.

Integration into the flight dynamics

As investigated in Section 3.1.1, the formulation of the conventional flight dynamics is introduced. To combine the proposed rotor aerodynamics, the formulation of conventional flight dynamics will be rewritten as follows:

$$\dot{\boldsymbol{S}_B} + \boldsymbol{\Omega_I} \times \boldsymbol{S_B} = \boldsymbol{L_B} \tag{3.12}$$

$$\boldsymbol{S_I} = \begin{bmatrix} \overline{\overline{T_I^B}} & 0 \\ 0 & \overline{\overline{R_I^B}} \end{bmatrix} \boldsymbol{S_B}, \ \boldsymbol{S_I} = \begin{bmatrix} \boldsymbol{V_I} \\ \boldsymbol{\omega_I} \end{bmatrix}, \ \boldsymbol{S_B} = \begin{bmatrix} \boldsymbol{V_B} \\ \boldsymbol{W_B} \end{bmatrix}, \ \boldsymbol{L_B} = \begin{bmatrix} \frac{\boldsymbol{G_B}}{m} + \frac{\boldsymbol{F_R}}{m} + \frac{\boldsymbol{F_F}}{m} \\ \boldsymbol{M_R} + \boldsymbol{M_{gy}} \end{bmatrix}$$
$$\tag{3.13}$$

The state vector of the translational and rotational velocities is denoted by $\boldsymbol{S}$, and the load that affects the multirotor behavior is represented by $\boldsymbol{L_B}$. Gravity is expressed as $\boldsymbol{G_B}$ with respect to the fuselage frame of reference. The aerodynamic force acting on the fuselage is represented as $\boldsymbol{F_F}$ and is based on the expression given in Eq. 3.10. Furthermore, the aerodynamic forces and moment vectors due to the rotors are denoted by $\boldsymbol{F_R}$ and $\boldsymbol{M_R}$, respectively. Those aerodynamic loads are expressed as a matrix form in Eq. 3.14.

$$\begin{bmatrix} \boldsymbol{F_R} \\ \boldsymbol{M_R} \end{bmatrix} = \sum_{i=1}^{4} (\boldsymbol{T_{map}})_i \begin{bmatrix} \overline{\overline{(T_H^B)}}_i & \overline{\overline{0_{3\times3}}} \\ \overline{\overline{0_{3\times3}}} & \overline{\overline{(T_H^B)}}_i \end{bmatrix} (\boldsymbol{R_{rot}})_i \tag{3.14}$$

where,

$$
(\boldsymbol{T_{map}})_i =
\begin{bmatrix}
1 & 0 & 0 & 0 & 0 & 0 \\
0 & 1 & 0 & 0 & 0 & 0 \\
0 & 0 & 1 & 0 & 0 & 0 \\
0 & -d_z & (-1)^i l & 1 & 0 & 0 \\
d_z & 0 & \frac{i-2.5}{|i-2.5|} l & 0 & 1 & 0 \\
-(1)^{\left(\frac{1}{2}(i^2 - i + 4)\right)} l & \frac{i-2.5}{|i-2.5|} l & 0 & 0 & 0 & 1
\end{bmatrix}
, \quad (\boldsymbol{R_{rot}})_i =
\begin{bmatrix}
(F_x)_i \\
(F_y)_i \\
(F_z)_i \\
(M_x)_i \\
(M_y)_i \\
(M_z)_i
\end{bmatrix}
$$

The aerodynamic force and moment of the rotor are represented by $\boldsymbol{R_{rot}}$ and are defined in the rotor hub frame. The details of the rotor aerodynamics is described in Section 2. The present rotor aerodynamics can be express as follows:

$$
(\boldsymbol{R_{rot}})_i = f(RPM_i, g_u, g_v, g_w, \phi, \theta, \psi, (\boldsymbol{V_b})_i, (\boldsymbol{V_H})_i, t) \ (i = 1 - 4) \tag{3.15}
$$

The transformation matrix $\overline{\overline{T_H^B}}$ is utilized to apply the rotor aerodynamics to the fuselage frame. The mapping matrix $\boldsymbol{T_{map}}$ maps the aerodynamic force and moment of the rotor to the fuselage frame, in which l represents the horizontal distance from the center of gravity (C.G.) of the vehicle to the rotor, and d_z is the height of the rotor. The mapping matrix is based on the cross-configuration and can be adjusted for other configurations.

The fourth-order Runge-Kutta approach will be employed to solve Eq. 3.12, and the state variables, such as the flight speed and fuselage tilting angle, are fed back to Eqs. 3.14 and 3.15, respectively. By using this procedure, an integration procedure for the proposed flight simulation is established as shown in Fig. 3.2.

52
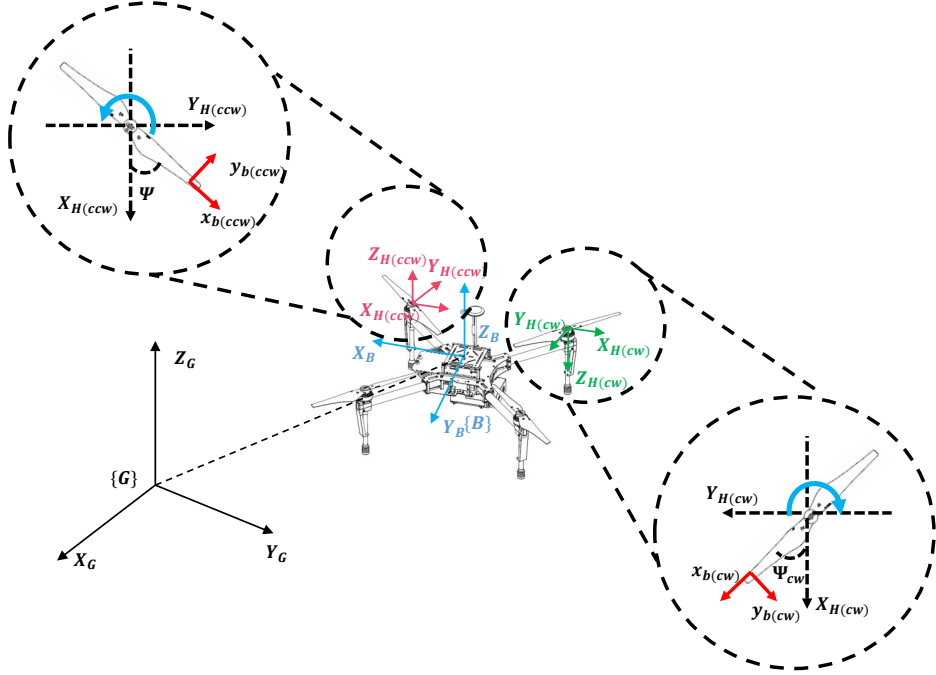
Figure 3.1   Frame of reference description for the multirotor UAV analysis
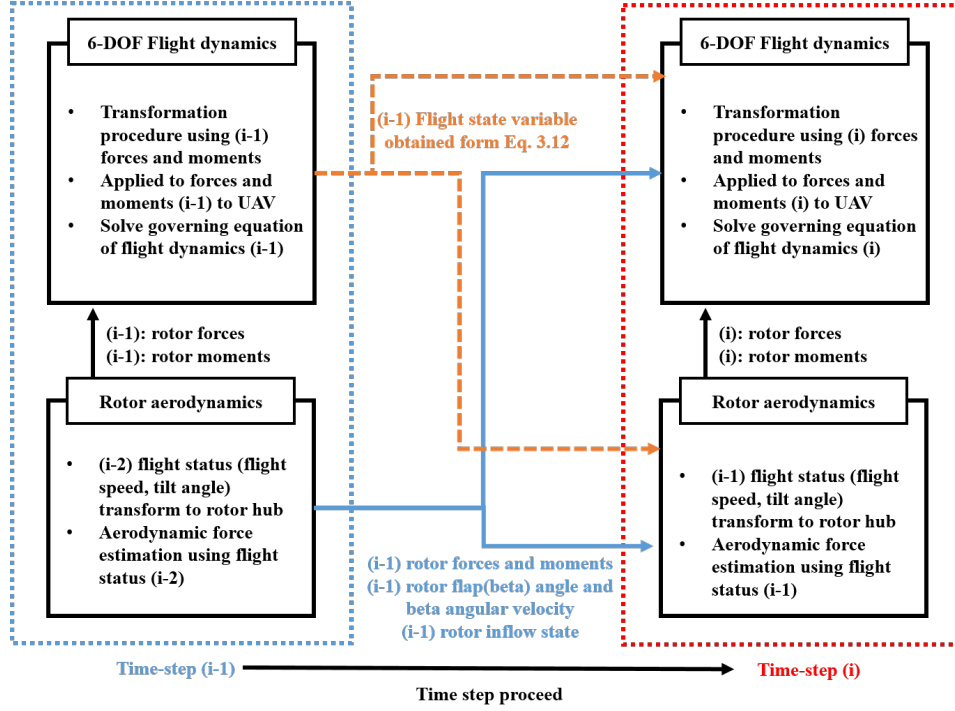
Figure 3.2 Integration procedure for the present simulation

3.2 Definition of the Control Law and Gust Estimation

In this section, the control law used in this dissertation will be introduced. Then, the gust estimation approach will be proposed to improve the accuracy of flight simulation.

3.2.1 Control law

System identification to predict the controller

The flight simulation proposed in this dissertation is compatible with various types of the control laws. Among those control laws, a proportional-integral-differential (PID) is selected. The control law used in a general multirotor UAV includes the following components: position, attitude, altitude, and rate. However, the attitude and altitude control laws of the target UAV used in this dissertation have not been publicized. To estimate those control laws, system identification will be applied to identify the dynamic properties of the target UAV. The frequency sweep method is usually used for such identification. The relevant formulations are described as follows:

$$\delta_{sw} = A_{sw}\sin(\omega_{sw}t) \tag{3.16}$$

$$\omega_{sw} = \omega_{sw_{min}} + K(\omega_{sw_{max}} - \omega_{sw_{min}}) \tag{3.17}$$

A_{sw} denotes the magnitude of sweep, and ω_{sw} is the frequency of function. K indicates the weight factor for the sweep method which is defined in Ref. [102]. By

that, δ_{sw} will be inserted into the target UAV to obtain the dynamic characteristics. Based on this procedure, the transfer functions of each axis such as roll, pitch, yaw, and altitude will be obtained. However, there is still room to find the gain of PID control law. For that, the parametric estimation approach performed by Park (Ref. [103]) will be used to predict the result of gain. The relevant formulation is expressed as follows:

$$J = min\sqrt{\sum (TF_{output} - O_{pre})^2} \qquad (3.18)$$

J is the objective function and the "fmincon" function in MATLAB is adopted to minimize that function. TF_{output} represents the output of the transfer function, while O_{pre} represents the result obtained from the present flight simulations. Its details will be discussed later.

3.2.2 Gust estimation

Necessity for gust estimation

Multirotor UAVs may face unexpected and unsteady gusts during the practical flight, which may lead to inaccuracies in the simulation that does not account for such gusts. Previous studies (Refs. [104],[105],[106]) have employed both direct and indirect methods to address that difficulty. The direct method utilizes a flow sensor to measure the gust strength. However, that method was challenging to be applied in a multirotor UAV due to aerodynamic interference caused by the rotors, which degraded flow sensor precision (Ref. [106]). Therefore, an indirect method that estimates gust strength using an inertial measurement unit (IMU) and GPS was proposed. Indirect

methods, such as the fuselage tilting angle prediction (Ref. [107]), state observer (Ref. [73]), and data-driven approach (Ref. [104]), were constructed. Although those approaches showed good prediction results, they have mostly been validated for hover. Since the gust experiments involve forward flight segments (Ref. [77]), it will be necessary to predict and evaluate such gust profiles during forward flight. Therefore, a straightforward estimation approach, such as the prediction of fuselage tilting angle (Ref. [107]), will be needed.

Gust estimation based on the nonlinear flight dynamics

The flight dynamics of a multirotor UAV are utilized to estimate the gust, excluding the gust in the vertical direction. This dissertation focuses on estimating the longitudinal and lateral gusts, using the fuselage tilting angle and flight speed, which are measured by IMU sensor. By applying Eq. 3.12, a correlation between the fuselage tilting angle and flight speed will be derived. As both the fuselage tilting angle and flight speed are affected by the gust, the following process will be implemented to determine gust strength. First, the fuselage tilting angles measured by the experiment can be expressed in Eq. 3.19.

$$
\begin{bmatrix} \phi_{exp}(t) \\ \theta_{exp}(t) \\ \psi_{exp}(t) \end{bmatrix} = \begin{bmatrix} \phi_{ideal}(t) + \delta\phi(t) \\ \theta_{ideal}(t) + \delta\theta(t) \\ \psi_{ideal}(t) + \delta\psi(t) \end{bmatrix}
\tag{3.19}
$$

The subscripts *exp* and *ideal* are used to distinguish the practical and ideal values without the gust, respectively. δ represents the difference between the two values.

Then, Eq 3.19 will be inserted into Eq 3.12 which only considers the attitude control law and does not include the position control law. As a result, the flight speed of UAV is obtained and described in Eq. 3.20. When UAV performs hover, ϕ_{ideal}, θ_{ideal}, and ψ_{ideal} will be adjusted to zero. The proposed flight simulation is then carried out using Eqs. 3.19 and 3.20 to estimate the flight speed of a multirotor UAV, which can be considered as the gust strength. Eq. 3.20 describes this expression.

$$
\begin{bmatrix} \dot{\hat{X}}(t) \\ \dot{\hat{Y}}(t) \end{bmatrix} = \begin{bmatrix} -g_X \\ -g_Y \end{bmatrix}
\tag{3.20}
$$

However, since the relationship is only applicable for a hover, an additional process will be needed for forward flight. This process consists of the following two parts. The first part involves predicting the steady response for forward flight. During the steady flight, the difference in the fuselage tilting angle between practical and ideal values will not be significant. However, the flight speed measured by IMU still differs from that predicted by the flight simulation. As a result, Eq. 3.20 is an insufficient formulation for forward flight. Thus, Eq. 3.20 will be modified to accommodate this, and the resulting formulation is described in Eq. 3.21. Furthermore, Eq. 3.21 is capable of predicting the gust in hover.

$$
\begin{bmatrix} \dot{X(t)}_{exp} - \dot{\hat{X}}(t) \\ \dot{Y(t)}_{exp} - \dot{\hat{Y}}(t) \end{bmatrix} = \begin{bmatrix} g_X \\ g_Y \end{bmatrix}
\tag{3.21}
$$

To accurately estimate the gust profile during forward flight, an additional procedure will be required. Although there exist several approaches to finding the gust profile, this thesis will employ a simple method. An iterative approach is used

to minimize the discrepancy of the flight speed between the practical and simulation for improving the accuracy of prediction. The following procedure will be carried out to obtain the gust profile. First, Eq. 3.21 will be inserted in Eq. 3.12 to obtain the ideal trajectories and gust profile. Based on that, the difference in flight speed between the simulation and practical cases will be determined. Then, this difference will be used to improve the accuracy of the proposed gust estimation. This process will be repeated until the root mean square error (RMSE) in the flight speed between the simulation and practical values converges. Algorithm 1 summarizes the proposed estimation procedure.

Algorithm 1 Proposed gust estimation algorithm

Require: $\phi_{exp}(t)$, $\theta_{exp}(t)$, $\psi_{exp}(t)$, $\dot{X}(t)_{exp}$, $\dot{Y}(t)_{exp}$, X_{ideal}, Y_{ideal}

1: Insert $\phi_{exp}(t)$, $\theta_{exp}(t)$, $\psi_{exp}(t) \rightarrow$ Eq. 3.12 without the position controller

2: Acquire $\dot{\hat{X}}(t)$, $\dot{\hat{Y}}(t)$

3: Set an initial gust $(g_X)_{in}$, $(g_Y)_{in}$ by Eq. 3.21

4: **if** forward flight flag $= 0$ **then**   ▷ flight flag 0 denotes the hovering

5:      Construct $g_X = (g_X)_{in}$, $g_Y = (g_Y)_{in}$

6: **else**   ▷ forward flight

7:      **for** *iteration i* **do**

8:          Acquire $(dg_X)_i = \dot{X}(t)_{exp} - (\dot{\hat{X}}(t))_i$, $(dg_Y)_i = \dot{Y}(t)_{exp} - (\dot{\hat{Y}}(t))_i$

9:          Acquire $(g_X)_{i+1} = (g_X)_i + (dg_X)_i$, $(g_Y)_{i+1} = (g_Y)_i + (dg_Y)_i$

10:         Insert X_{ideal}, Y_{ideal} $(g_X)_{i+1}, (g_Y)_{i+1} \rightarrow$ Eq. 3.12 with the position controller

11:         **if** $(RMSE(i+1) - RMSE(i) < 1e^{-5})$ **then**

12:            Construct $g_X = (g_X)_{i+1}$, $g_Y = (g_Y)_{i+1}$

13:            Brake

14:         **end if**

15:      **end for**

16: **end if**

---

4 Verification for the Rotor Aerodynamics

4.1 Results for an isolated rotor aerodynamics

This section describes comparing and validating the proposed aerodynamic analysis, which considers both dynamic inflow and rigid blade flapping. The aim of this section is to evaluate the effect of the rigid blade flapping during forward flight.

4.1.1 Predictions of the force, moment, and drag

The proposed aerodynamic analysis will be evaluated using a forward flight experiment performed by Theys et al. (Ref. [28]). The experiment involved varying the fuselage tilting angle at a freestream condition of 6 m/s, and measuring the thrust, torque, and drag. They measured the specification of the blade such as the chord length and twist angle. In addition, they assumed the cross-sectional shape of the airfoil as a NACA5510. In this thesis, XFOIL software (Ref. [108]) is used to obtain the aerodynamic coefficients of the airfoil. Prior to analyzing forward flight, the steady-state thrust and torque during the hover experiment will be compared with the proposed aerodynamic analysis. Figure 4.1 shows that the present analysis accurately predicts both results when compared against the experiment.

Thrust, torque, and drag are compared for forward flight under different conditions of the fuselage tilting angle such as 0°, 30°, 60°, and 90°, which corresponds to a freestream speed of 6 m/s. 90° fuselage tilting angle represents an axial flight condition. Figure 4.2 presents the results obtained from the present thesis and the experimental results for a climbing flight condition. Results of both thrust and torque show a maximum discrepancy of 5% compared against the experimental results, indicating a similar trend. Although the predicted trend for the drag is not observed, the lower drag values will bring it to be negligible. During forward flight, the rigid blade flapping takes place regardless of the blade stiffness, as discussed in Section 2.1.2. To predict non-dimensionalized flapping natural frequency in Eq. 2.9, it will be necessary to determine the equivalent hinge offset and non-rotating natural frequency. For that, the material properties of the blade will need to be verified through the experiments, as demonstrated by Russell et al. (Ref. [109]). However, such experimental method will need expanded cost to obtain the result. Therefore, a parametric analysis will be carried out in this dissertation. Non-rotating natural frequencies and the position of the equivalent hinge offset will be determined in several cases. Initially, it is necessary to identify which of the two, equivalent hinge offset and non-rotating natural frequency, has a more significant effect on the drag prediction. Figure 4.3 (a) illustrates the parametric study concerning the non-rotating frequency. The equivalent hinge offset is fixed at 5%, and the non-rotating natural frequency increases from 20 Hz to 100 Hz in increment of 20 Hz. Figure 4.3 (b) shows the effect of the equivalent hinge offset. The non-rotating frequency is set at 20 Hz, and the equivalent hinge offset is increased from 5% to 45% in increment of 10%. Both

cases consider a fuselage tilting angle of 30,° and a freestream speed of 6 m/s for the forward flight condition. Figure 4.3 (a) demonstrates that the non-rotating frequency agrees with the experimental results at lower rotational speed, but underestimates them as it increases. Figure 4.3 (b) shows that the result at 5% equivalent hinge offset location is comparable to the experimental result, but the discrepancy will increase with respect to RPM. Theys (Ref. [28]) reported an average discrepancy of over 30% when compared to the experimental data. However, when considering the rigid blade flapping in this dissertation, the discrepancy will be significantly reduced to be less than 10%. By the present parametric analyses, the following parameters such as the equivalent hinge offset of 5% and a non-rotating frequency of 20 Hz exhibit the most similarities to the experimental results. To confirm the validity of these findings, the experiment (Ref. [110]) measuring the coning angle with the similar blade dimensions is to be compared. DJI Phantom3 9×4.5 blade is used, and at 9,000 RPM, the average coning angle was 1.7°. In comparison, Graupner 9×5 blade used in this dissertation is predicted to have a coning angle of 1.4° at 9,000 RPM. Although the discrepancy between the two measurements is 18%, it should be noted that the material properties and blade shape are not identical. Therefore, the accuracy may be improved with more precise characteristics of the blade.

In Fig. 4.4, the experimental results for the thrust, drag, and torque are compared against the proposed analysis which uses ν_{β_f} obtained from the parametric analysis for the rigid blade flapping. The average difference between the predicted and experimental results for the drag is below 10%, which is significantly lower than the discrepancy without considering the rigid blade flapping, which exceeds 30%.

Although the discrepancy between the predicted and experimental values increases as the rotational speed increases, the average discrepancy will still be less than 10%. Furthermore, the trend is found to be consistent. Therefore, considering the rigid blade flapping will be crucial for more precise drag prediction.
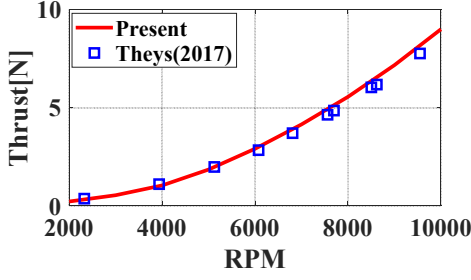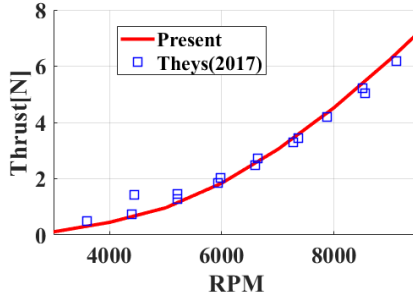
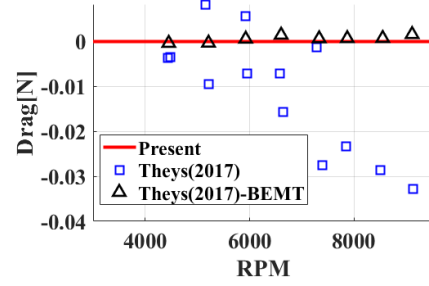**(a)** Comparison between the proposed aerodynamic analysis and experimental thrust
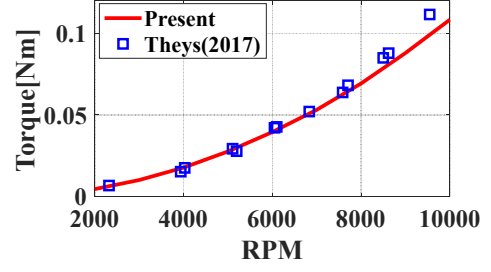
(b) Comparison between the proposed aerodynamic analysis and experimental torque
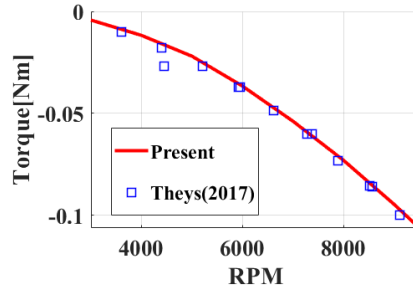
Figure 4.1 Comparison between the proposed aerodynamic analysis and experimental results in hover for Graupner 9×5
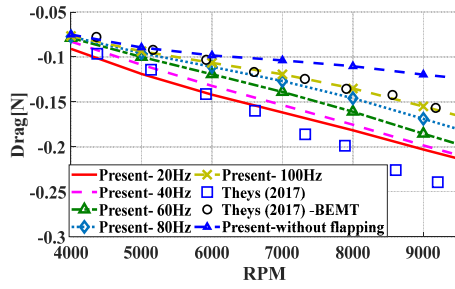

(a) Thrust (fuselage tilting angle = $90°$)
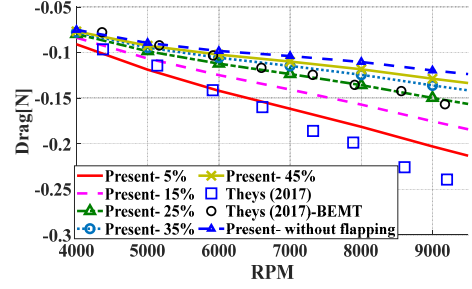
(b) Drag (fuselage tilting angle = $90°$)

(c) Torque (fuselage tilting angle = $90°$)

Figure 4.2 Comparison between the proposed aerodynamic analysis and experimental results in climb for Graupner 9×5
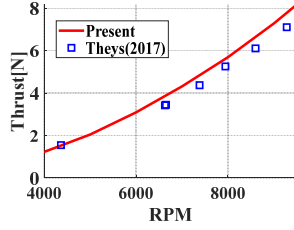
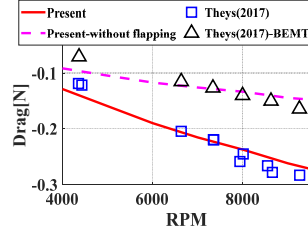**(a)** Comparison of the drag for different non-rotating frequencies

(b) Comparison of the drag for different equivalent hinge offset locations

Figure 4.3 Parametric results for the rigid blade flapping in forward flight

(a) Thrust (fuselage tilting angle $= 0\,^\circ$)

(b) Drag (fuselage tilting angle $= 0\,^\circ$)
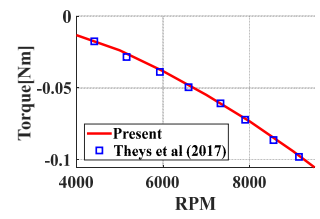
(c) Torque (fuselage tilting angle $= 0\,^\circ$)

(d) Thrust (fuselage tilting angle $= 30\,^\circ$)

(e) Drag (fuselage tilting angle $= 30\,^\circ$)

(f) Torque (fuselage tilting angle $= 30\,^\circ$)

(g) Thrust (fuselage tilting angle $= 60\,^\circ$)

(h) Drag (fuselage tilting angle $= 60\,^\circ$)

(i) Torque (fuselage tilting angle $= 60\,^\circ$)

Figure 4.4 Comparison between the proposed aerodynamic analysis and experimental results in forward flight

4.1.2 Effect of the rigid blade flapping on forward flight
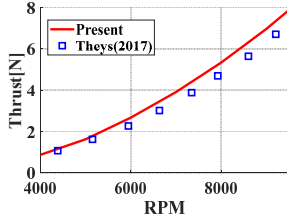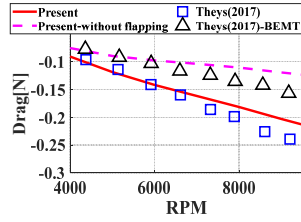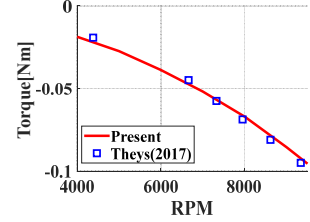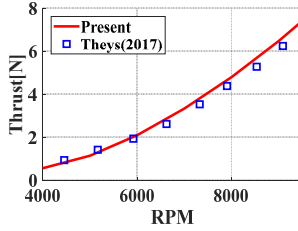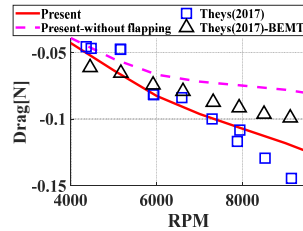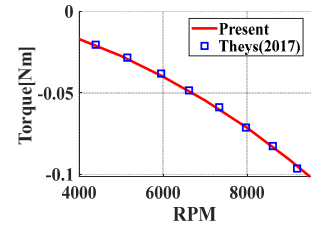
The previous section compared and validated the improvement of the rotor aerodynamic analysis. The existing studies (Ref. [86, 111]) described that the rigid blade flapping would affect the flight performance of multirotor UAV. To identify such effect, this section aims to investigate the effect of the rigid blade flapping on UAV during various forward flight condition. First, the sectional thrust and drag of the rotor disk will be compared to evaluate the effect of the rigid blade flapping under two forward flight conditions. The rotational speed of the rotor is kept constant because the dimensionless forward speed μ changes based on the rotational speed of the rotor. Graupner 9×5 blade is typically used for a 1.2 kg multirotor UAV, and it requires about 7,000 RPM to generate a thrust of 0.3 kg. Due to that, this particular RPM value is selected. The analysis is performed for a fuselage tilting angle of 0° and at two different forward speeds of 6 m/s and 30 m/s.

The results for a lower advance ratio of 0.0716 are depicted in Fig. 4.5. Sectional thrust shows a similar trend regardless of the flapping, while the overall drag distribution prediction with the rigid blade flapping estimates more drag than that of the result without the flapping. In Fig. 4.6, the advance ratio is 0.3581. In contrast to Fig. 4.5, the sectional thrust exhibits a significant discrepancy based on the presence of the rigid blade flapping. Figure 4.6 (a) and (b) demonstrate that the sectional thrust is reduced when the rigid blade flapping is taken into account. Additionally, the discrepancy in the drag becomes more prominent as the forward flight speed increases. Consequently, it is inferred that the inclusion of the rigid blade flapping will
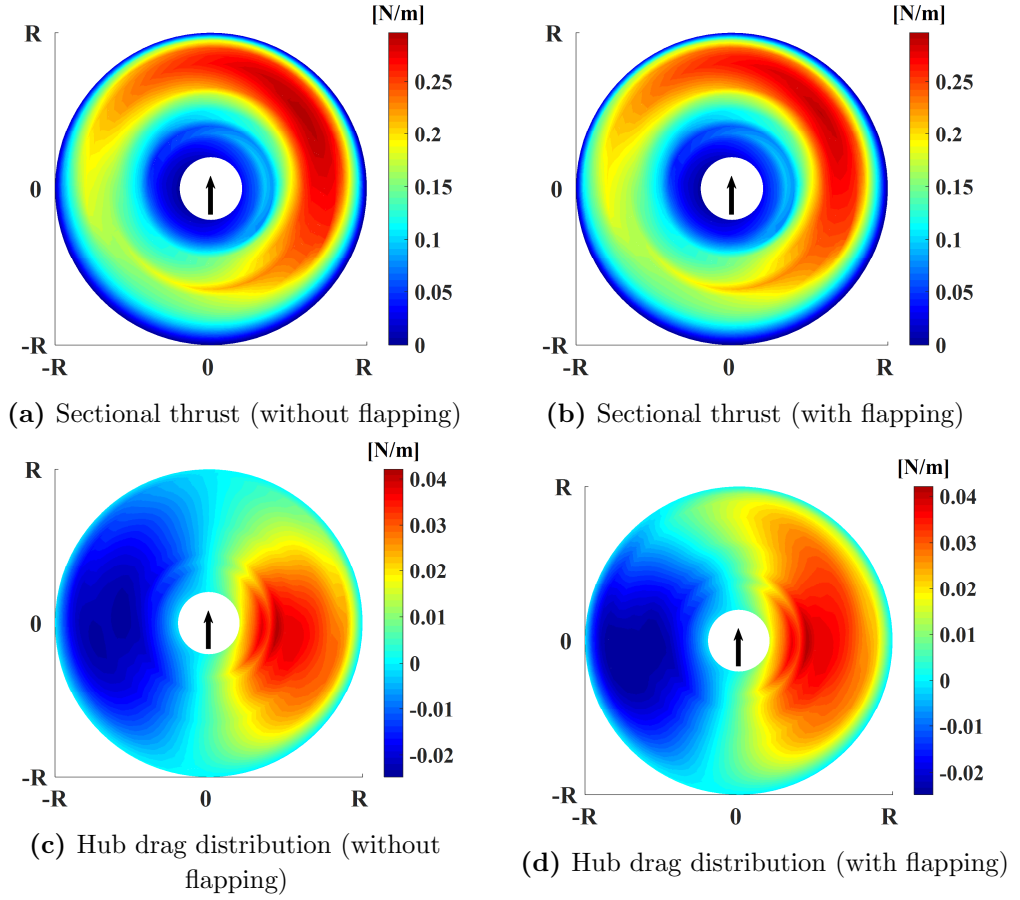
be crucial in the flight simulation of a multirotor UAV that operates at a high advance ratio, as it influences the flight performance when the forward speed increases.

The wind tunnel experimental results provided by Kolaei et al. (Ref. [112]) are used to compare and verify the forward flight condition. They used T–MOTOR 18×6.1 blade. Barcelos (Ref. [113]) obtained the cross-sectional shape at 25%, 50%, and 75% span-wise positions, and linear interpolation was utilized to approximate the airfoil for the non-measured region. The results based on three rotational speeds and four fuselage tilting angles are used to be compared with the proposed analysis. While the experimental results will be obtainable for thrust, there are no results available for the drag. Hence, the comparison of the drag is performed using only the prosed analysis with the presence and absence of the rigid blade flapping, as illustrated in Fig. 4.7.

The result exhibits that the thrust will be increased when the fuselage tilting angle is lower than $15\,^\circ$ regardless of the rigid blade flapping. Additionally, concerning larger tilting angles of $30,^\circ$ and $60,^\circ$, thrust appears to decrease as the advance ratio increases. By the following observation, the thrust of the rotor shows a decreased trend when it reaches a certain angle. As the fuselage tilting angle increases, the perpendicular speed increases, thereby decreasing the thrust. Therefore, the findings suggest that the wind in the vertical direction has a more pronounced effect on thrust. Furthermore, the effect of the rigid blade flapping is less significant when the fuselage tilting angle is increased. The proposed analysis tends to overestimate the experimental results, despite having a similar trend. This discrepancy is primarily due to insufficient information on the airfoil section over the span. Therefore, it is

expected that the difference will decrease if more precise specification on the airfoil and aerodynamic coefficient is provided. As the advance ratio of the freestream increases, the result of drag will show a decreasing trend. In contrast to the thrust, the prediction for the drag is significantly affected by the rigid blade flapping. At 5,° and 0.25 advance ratio, the predicted results exhibit a three times larger discrepancy. These results indicate that the rigid blade flapping will be crucial to predict the drag during forward flight, particularly in the case of the sideward and forward winds.

(a) Sectional thrust (without flapping)

(b) Sectional thrust (with flapping)

(c) Hub drag distribution (without flapping)

(d) Hub drag distribution (with flapping)

Figure 4.5 Forward flight condition (1) $\mu = 0.0716$ (V = 6 m/s, fuselage tilting angle = $0\,^{\circ}$)

(a) Sectional thrust (without flapping)

(b) Sectional thrust (with flapping)

(c) Hub drag distribution (without flapping)

(d) Hub drag distribution (with flapping)
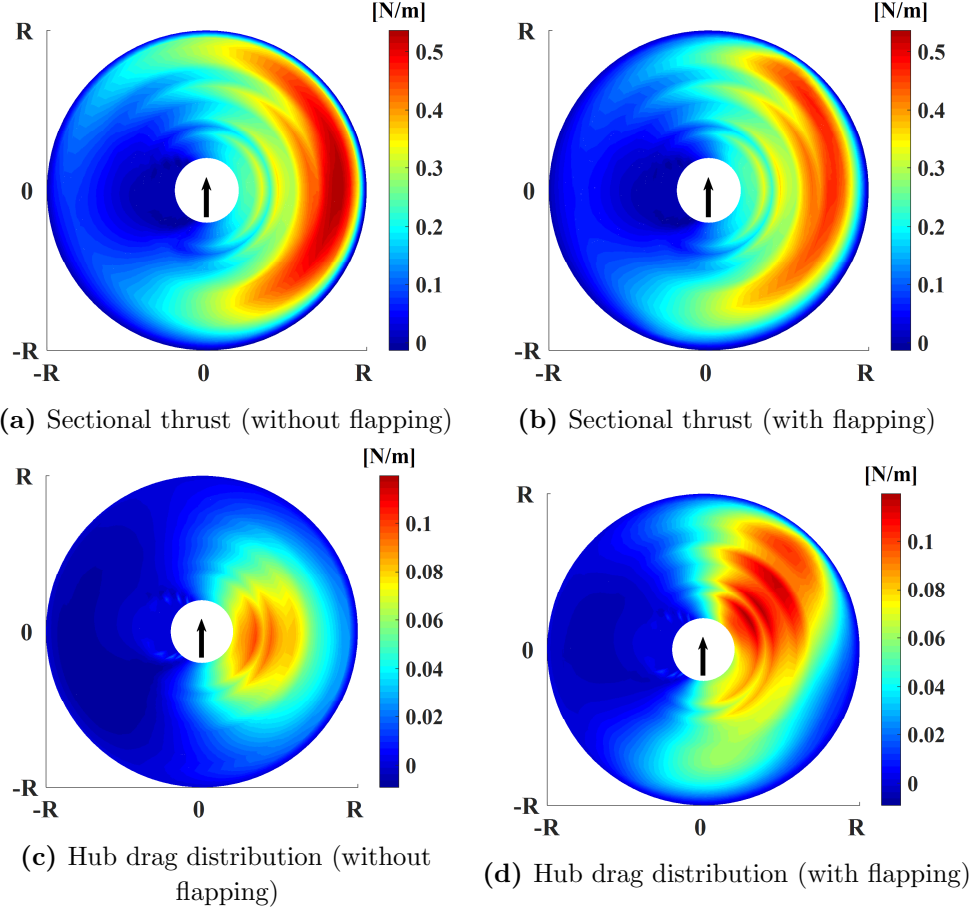
Figure 4.6   Forward flight condition (2) μ =0.3581 (V = 30 m/s, fuselage tilting angle = 0 °)
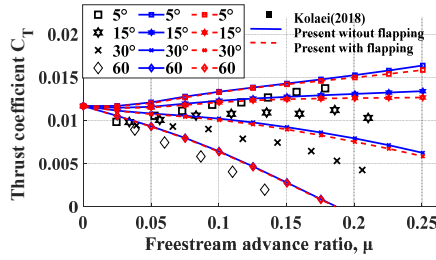
(a) Thrust coefficient comparison at 3,000 RPM
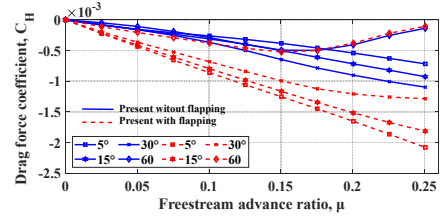
(b) Drag coefficient comparison at 3,000 RPM
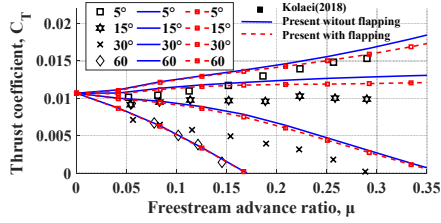
(c) Thrust coefficient comparison at 4,000 RPM
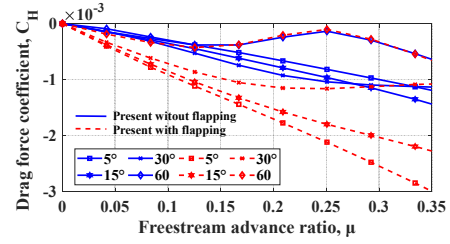
(d) Drag coefficient comparison at 4,000 RPM
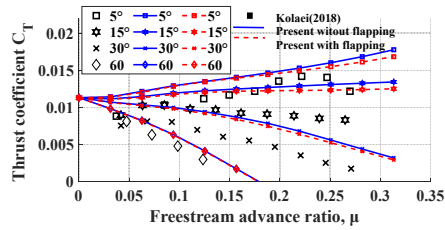
(e) Thrust coefficient comparison at 5,000 RPM
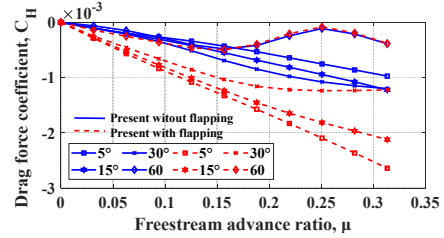
(f) Drag coefficient comparison at 5,000 RPM

Figure 4.7   Comparison of the thrust and drag coefficient when including the rigid blade flapping at various fuselage tilting angles

73

4.2 Results for the aerodynamic interference among the rotors

This section will explain the results of the aerodynamic interference among the rotors. Initially, the proposed approach based on Taylor series with the multiple nominal points will be evaluated and investigated. Subsequently, the comparison and validation will be performed for non-overlapping multirotor configurations such as the tandem, quadrotor, and hexarotor.

4.2.1 Evaluation of the analytical formulation

The analytic formulation for the aerodynamic interference among the rotor is derived in Section 2.2. This formulation based on the dynamic vortex tube (Ref. [88]) is applied and extended. The approach such as the dynamic vortex tube was only developed for a single rotor configuration. Due to that, an additional evaluation should be needed for a multirotor configuration. Additionally, to decrease the computational time required for the flight simulation, Taylor series expansion will be performed at multiple locations. Selecting an appropriate number of the locations will be necessary since the accuracy of the expansion depends on it. Additionally, an extra procedure will be carried out to implement Eq. 2.28. Numerical integration to obtain the solution of Eq. 2.28 will increase the computational time at each time step during the simulation. As a result, an offline method will be adopted to create a table of the result of Eq. 2.28 in terms of the skew angle and side-slip angle. Although the time required for producing the tabulated result is increased in terms of the number

of the rotors, this method will become more efficient than carrying out numerical integration at each time step during the simulation.

To evaluate the present formulation, the relevant investigations will be performed. The major focus of this analysis is investigating the trend of the interference among the rotors. It will be crucial to consider the aerodynamic interference among the multiple rotors under all flight conditions. However, the interference between the front and rear rotors plays a crucial role in forward flight (Refs. [114, 15]). That interference will be evaluated using the parameters such as the hub distance. The trend will be investigated using two rotor blades: one for a tandem configuration based on the 9-inch propeller used by Nguyen (Ref. [53]), and another for a side-by-side configuration using a 24.5-inch propeller that was examined by Russell (Ref. [37]). Table 4.1 summarizes the details of the investigation.

Figure 4.8(a) illustrates the investigation of the mean inflow component λ_0 in terms of the hub distance, denoted as Situation H. Situations H1 and H2 have zero side-slip angles, indicating that the wake of the front rotor passes through the rear rotor. In Table 4.1, the difference between Situations H1 and H2 are specified. As the distance between the hub is 2.5, the magnitude of the rear rotor inflow is large, while the discrepancy of the inflow for the front rotor is less significant. The predicted results of both the front and rear rotor inflow show a small discrepancy when the hub distance increases. Situation H2 exhibits a greater discrepancy in mean inflow compared to Situation H1 because the wake of the front rotor is closed to the disk of the rear rotor due to the increasing advance ratio. Figures 4.8 (b) and (c) illustrates the trend of the cyclic inflows. According to the obtained results, the total inflow of

the rear rotor relies on the hub distance, and the amount of inflow is more significant than that of an isolated rotor. A similar trend was observed in an existing study (Ref. [59]). Consequently, the proposed method is capable of estimating the inflow of the tandem configuration which is non-overlapping. The detailed verification for the tandem configuration will be described in the next section.

The next investigation is conducted for the side-by-side configuration. As summarized in Table 4.1, the side-slip angle of both Situations H3 and H4 is 90 °. Prior to investigating the effect of the side-by-side configuration, it is necessary to validate such configuration to observe a meaningful trend. To validate that configuration, the thrust and torque results based on the experiment (Ref. [37]) are compared in terms of the hub distance. The flight condition such as the edgewise is applied to compare the present approach. Russell suggested the three cases of hub distance denoted as wide, middle, and inner location. Each distance range, wide, middle, and inner location, is normalized by the radius of the rotor blade and has values of 3.16, 2.67, and 2.02 respectively. Further validation for that blade will be performed in the next section. Figure 4.9 exhibits the comparison results of the side-by-side configuration. The estimated results such as isolated, wide, and mid situations show good agreement with the experiment. However, there is a large discrepancy in the inner location. This is due to the proposed formulation being based on the rigid cylindrical wake, which does not consider vortex interaction among the wake. As the hub distance approaches 2, the intensity of vortex interaction increases, resulting in decreased accuracy of the present formulation. Based on these results, the distance range such as 2.6 to 3.2 is sufficient to be estimated by the proposed formulation.

Thus, the minimum hub distance is set as 2.5 for the investigation of side-by-side configuration. The findings show that the net inflow of the side-by-side configuration is lower than that of the result without interference, as shown in Fig. 4.10. Previous analyses with high fidelity (Refs. [115, 114]) have demonstrated that the thrust in the side-by-side configuration increases. Although the proposed formulation may not be completely accurate when the hub distance is near 2, the present analysis will be capable of predicting the relevant trend of the aerodynamic interference among the rotors.
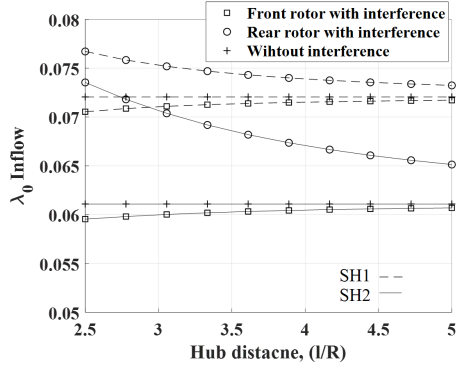
(a) Mean component of the inflow
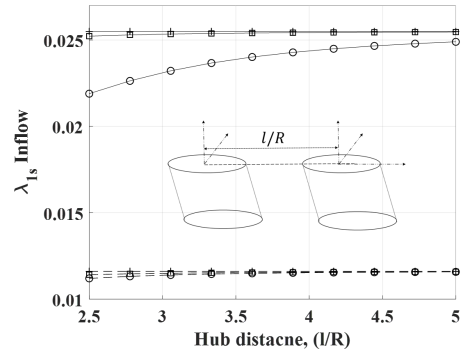
(b) Lateral component of the inflow
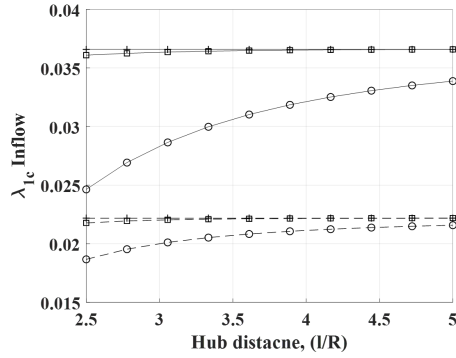
(c) Longitudinal component of the inflow

Figure 4.8   Inflow trend of the tandem configuration in terms of the hub distance
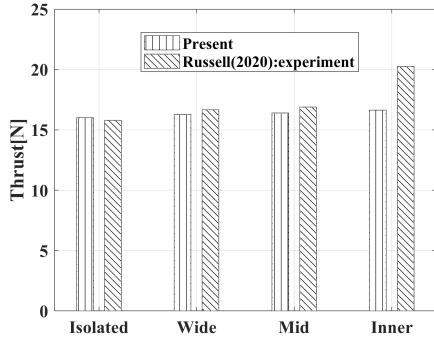
(a) Thurst in terms of the hub distance
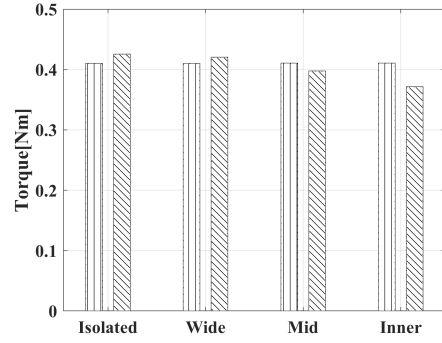
(b) Torque in terms of the hub distance

Figure 4.9   Comparison between the proposed analysis and experimental result: side-by-side configuration
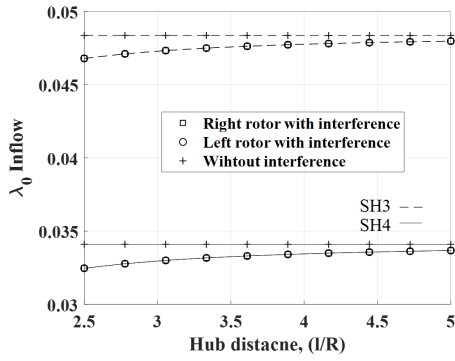
(a) Mean component of the inflow
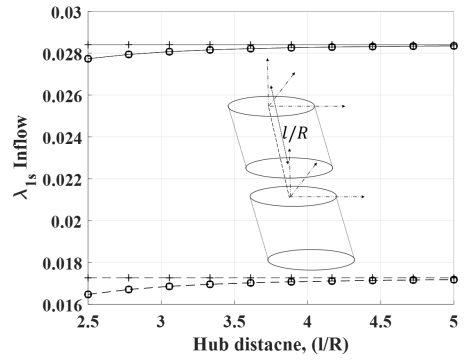
(b) Lateral component of the inflow
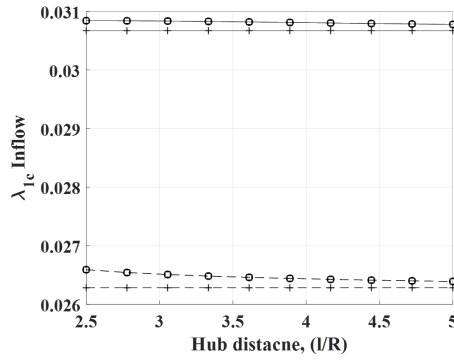
(c) Longitudinal component of the inflow

Figure 4.10   Inflow trend of the side-by-side configuration in terms of the hub distance

Table 4.1 Properties of the proposed interference analysis in terms of the hub distance

	Hub distance, l/R	Advance ratio, μ	Side-slip angle, °	Rotor blade diameter, in
Situation H1 (SH1)	2.5 to 5	0.06 (Ref. [53])	0	9 (Ref. [53])
Situation H2 (SH2)	2.5 to 5	0.12 (Ref. [53])	0	9 (Ref. [53])
Situation H3 (SH3)	2.5 to 5	0.09 (Ref. [37])	90	24.5 (Ref. [37])
Situation H4 (SH4)	2.5 to 5	0.19 (Ref. [37])	90	24.5 (Ref. [37])

4.2.2   Further numerical results

In Section 4.2.1, it is confirmed that the present approach can consider and predict aerodynamic interference among the rotors. Using this formulation and the proposed rotor analysis based on the dynamic inflow, multirotor configurations including the tandem, quadrotor, and hexarotor will be examined and compared against the previous experimental studies and high-fidelity analyses.

Results for the tandem rotors

The analysis of the tandem rotor configuration is performed prior to comparing the results of the quadrotor UAV. While the conventional tandem rotors have overlapping areas, multirotor UAV will not. The tandem configuration examined in this dissertation does not have any overlapping areas.

The proposed formulation and rotor aerodynamics are combined for analysis and compared against the experimental results (Ref. [53]). Nguyen et al.(Ref. [53]) investigated the characteristics of the aerodynamic interference based on the wind tunnel test. Table 4.2 provides the detailed experiment conditions. They did not describe the detailed configuration of the airfoil. To compensate for such limitation, the similar airfoil configuration suggested by other researchers (Ref. [103]) is used to estimate the aerodynamic coefficient. That aerodynamic coefficient is obtained by XFOIL (Ref. [108]) software.

Table 4.2 explains the details of the experimental results. Nguyen only provided thrust results without the torque, pitching, and rolling moments. Due to that, the proposed analysis is compared against the thrust result only. First, the result for an

isolated rotor is compared, shown in Fig. 4.11(a). The comparison result indicates that the average discrepancy between the present analysis and experiments is 6%. This discrepancy can be decreased by specifying the cross-section of the airfoil according to span location. Then, Experiment 2 denoted in Table 5.2 is used to comparing the proposed analysis for a tandem rotor configuration. The experimental conditions are as follows: fixed hub distance, varying rotational speed, and -5° fuselage tilting angle. In Fig. 4.11 (b), the comparison of thrust difference ratio including such a simple approach described in Introduction is performed. When there is no interference between the rotors, the thrust difference ratio will be equal to one. Both present analysis and a simple approach demonstrate good consistency against the experimental results. Nevertheless, a simple approach is incapable of accurately predicting the trend of the aerodynamic interference in terms of the hub distance. Fig. 4.11(c) reveals that the simple method shows a significant discrepancy except for a specific range between 2.8 and 3.3. The approach proposed by Nguyen was based on the several assumptions. 1) The interference formulation was only considered at the center of the rear rotor, thereby disregarding the entire disk area of the rear rotor. 2) Nguyen only considered the uniform inflow components without accounting for the cyclic inflow. 3) Nguyen neglected the bound circulation of the rotor. Those assumptions rendered the accuracy of the approach suggested by Nguyen the unreliable outside a certain range. In contrast, the proposed analysis demonstrates good agreement with the experimental results. The average discrepancy between the proposed analysis and experimental results is only 2%, which can be attributed to the fact that the proposed analysis takes into account the cyclic inflow, entire rotor disk,

82

and bound circulation of the rotor. These considerations lead to improved prediction accuracy, as evidenced by the results. However, both proposed analysis and simplified approach have limitations in their consideration of the vortex interaction among the wakes, and a certain range should be maintained to ensure accuracy. Although such limitation is a weakness of the proposed analysis, the trend of aerodynamic interference for a tandem rotor configuration will be estimated sufficiently by the proposed analysis.
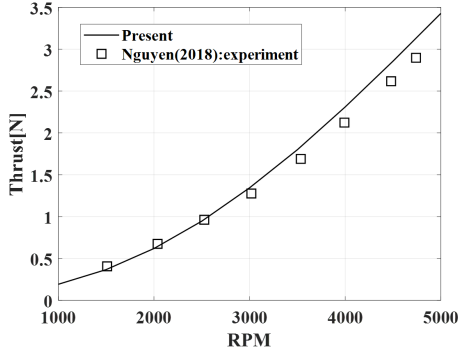
(a) Thrust for an isolated rotor in terms
of the rotational speed
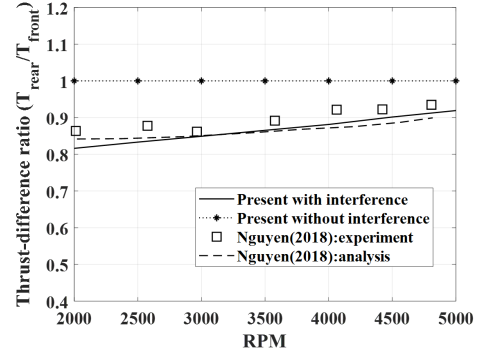
(b) Thrust difference ratio for a tandem
rotor in terms of the rotational speed
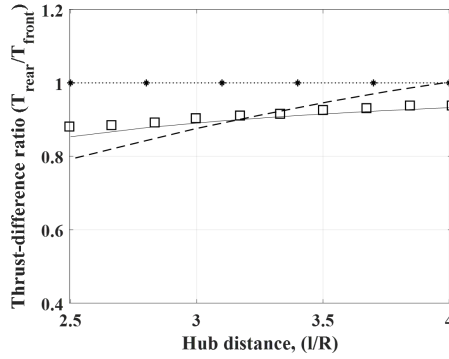
(c) Thrust difference ratio for a tandem
rotor in terms of the hub distance

Figure 4.11   Comparison between the proposed analysis and experimental results:
tandem configuration

Table 4.2 Details of the experimental conditions for the tandem rotor configuration (Ref. [53])

Experiment	1	2	3
Configuration	Isolated rotor	Tandem rotor	Tandem rotor
Hub distance, (l/R)	-	2.83	2.5 to 4.5
Rotational speed, RPM	1,500 to 5,000	1,500 to 5,000	3,960
Free stream speed, m/s	6	6	6
Tilting angle (nose up: +), °	0	-5	-5

Results for a quadrotor and hexarotor configuration

This section examines various multirotor configurations, including the quadrotors and hexarotors. The result obtained by the present analysis compares the results from the studies conducted by Misiorowski et al. (Ref. [91]) and Russell et al. (Ref. [37]). Misiorowski utilized a CFD method to observe the aerodynamic interference of a quadrotor UAV. Two configurations such as the cross- and plus- type were investigated and they proposed the following analysis conditions: (1) The rotor blade for analysis is selected as APC 12×5.5. They described the details of the rotor blade geometry in Ref. [91]. (2) Geometry of the quadrotor and operating conditions are summarized in Table 4.3. The configuration of both cross- and plus- types are shown in Fig. 4.12. In the experimental study, the facility for the multirotor was established by Russell and Conley (Ref. [37]). Such facility was capable of measuring the aerodynamic forces of the individual rotors. The following conditions were proposed by Russell for the experiment of the multirotor. (1) KDE 24.5×8.1 blade was used for the experiment. However, they did not provide the detailed information on that blade. Due to that, the result obtained by Jung et al. (Ref. [116]) is used in this dissertation. (2) Table 4.4 describes the experimental parameters such as the operating free stream and fuselage tilting angle. In Fig. 4.12 (c), the configuration of the multirotor facility is illustrated.

First, the proposed analysis is compared with CFD predictions by Misiorowski and the relevant results are evaluated. The initial comparison is conducted for an isolated rotor, where the free-stream speed and fuselage tilting angle are based on Table 4.3. The thrust and torque results of the proposed analysis showed good agreement

against the CFD predictions shown in Figs. 4.13(a) and (b). Figures 4.13(c) and (d) illustrate that the pitching and rolling moments have an average discrepancy of 10% and 20%, respectively. Despite the presence of significant discrepancies, the proposed analysis can correctly identify the trend of those moments. Moreover, those discrepancies are not critical concerning a quadrotor UAV. During the forward flight of a multirotor UAV, there is a variation in thrust between the front and rear rotors. This causes the entire pitching and rolling moments of UAV, which are larger in magnitude than that of the moments created by the rotors. Then, both cross- and plus-quadrotor configurations are evaluated and compared, as demonstrated in Fig. 4.12(a) and (b). Barcelos et al. (Ref. [17]) developed a distributed vorticity element to consider interference for a multirotor UAV. They attempted to compare that method using CFD prediction presented by Misiorowski. Figure 4.14 exhibits the comparison of those two methods and the present analysis. The proposed analysis is in good agreement with CFD prediction, and the discrepancy is 5% and 8% for both the front and rear rotors. The relevant result is shown in Fig. 4.14(a). The results obtained by Barcelos show good accuracy in capturing the thrust of the front rotors, but significant discrepancies are observed in the results for the rear rotor. In Fig. 4.14(b), the proposed analysis shows good agreement with CFD prediction for torque results. As shown in Fig. 4.14 (c), the pitching moment result is illustrated. Barcelos overestimated significantly further than CFD prediction. Although the present analysis shows a discrepancy, it is more closed to CFD prediction. The pitching moment results for all rotors exhibit significant discrepancies in the results presented by Barcelos, whereas the proposed analysis shows less significant

87

discrepancies in the pitching moment results for the front rotors. However, the proposed analysis cannot accurately predict the trend of pitching moments for the rear rotors. Furthermore, Fig. 4.14(d) shows that both proposed analysis and approach proposed by Barcelos exhibit significant discrepancies in the results for the rolling moments of the rear rotors. Those discrepancies are explained by the sectional thrust result, as shown in Fig. 4.15, where the sectional thrust results of both the proposed analysis and CFD prediction are compared. Although the proposed analysis overestimates the sectional thrust, a similar trend of thrust distribution is observed at the front rotor. The analysis results for the rear rotor highlight the reason for the increased discrepancies in the pitching and rolling moments. In contrast to CFD prediction, the proposed analysis predicts a large value of sectional thrust at $180,^\circ$ azimuth angle for the rear rotor. That overestimation increases the pitching moment discrepancy. Furthermore, a significant discrepancy is exhibited in the region of the retreating side. The present analysis is limited in its ability to capture the interference among the rotors since it is based on the simple vortex theory. In addition, such theory does not grasp the vortex interaction which can be captured by a high-fidelity analysis. As a result, the accuracy of the prediction is reduced compared against CFD approach, and the proposed analysis has certain limitations. The evaluation of the plus-shaped configuration is shown in Fig. 4.16. The thrust and torque results in Figs. 4.16(a) and 4.16(b) agree well with CFD prediction. Although there are discrepancies for the pitching and rolling moments, those results will become smaller than those for the cross-shaped configuration. Since the distance between the North and South rotors is greater than that between the Northwest and Southwest rotors,

the effect of the aerodynamic interference is less pronounced. Tables 4.5 and 4.6 described the detailed results for both cross- and plus-shaped configurations.
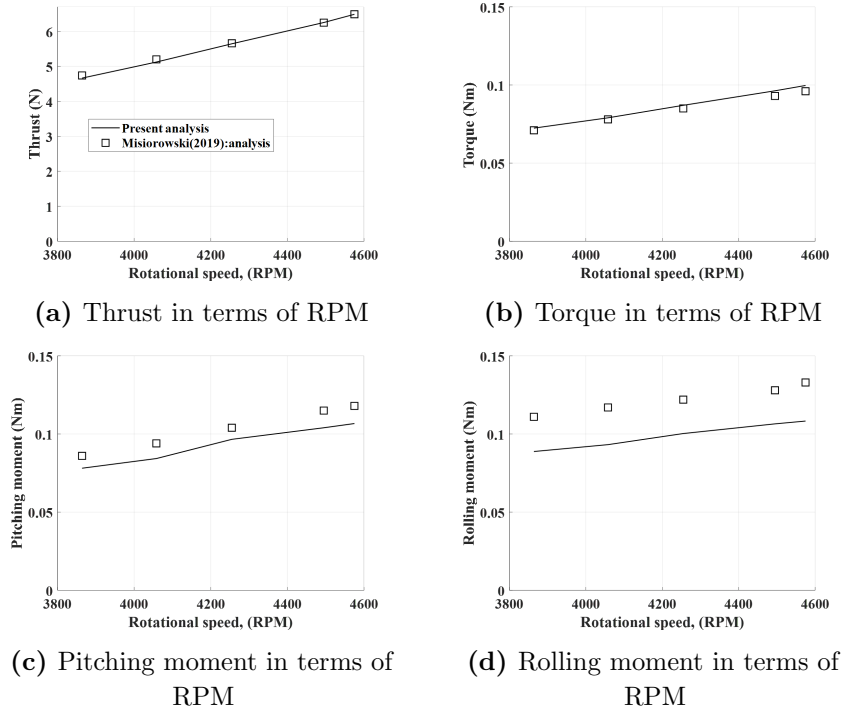
Next, a comparison between the proposed analysis and experimental results presented by Russell is performed. The experimental result of the quadrotor configuration only measured the thrust and torque of the rear rotor, Rotor 3, which was defined by Russell (Ref. [37]). The free-stream speed values are summarized in Table 4.4. The comparison results of both isolated and quadrotor configurations are illustrated in Fig. 4.17. That result shows that the average discrepancies of the thrust for both configurations are smaller than 5%. The predicted results of torque show an underestimation than that of the experiment, but the proposed analysis exhibits the capability of capturing such trend. Furthermore, the average discrepancy is less than that of 6%. Subsequently, the hexarotor configuration is compared. In addition, two different free-stream conditions are utilized for the experimental study to measure the thrust and torque of each rotor, Rotors 1 to 6, individually, as listed in Table 4.4. Figure 4.18 (a) and (b) display the comparison between the proposed analysis and experimental results conducted under a free-stream speed of 6.1 m/s. The proposed analysis shows the capability of capturing the thrust and torque trends according to the location of the rotors, such as the frontmost, middle, and rearmost rotors. Furthermore, the proposed analysis demonstrates good agreement with the experimental results obtained at 12.2 m/s, as demonstrated in Figs. 4.18 (c) and (d). The experimental results reveal several weaknesses of the proposed analysis. (1) The results obtained from the experiment show that the aerodynamic loads of the right and left rotors are not symmetric at a free-stream speed of 6.1m/s.

89

Such discrepancy is increased when the location of the rotor is rearmost. However, the proposed analysis predicts the symmetric results. This is because the proposed analysis assumes a rigid cylindrical wake and cannot easily account for unsymmetric trends resulting from the wake interactions (Refs. [117, 118]). Although the increase in advance ratio reduces those discrepancies, such discrepancies will still be present. (2) Based on the perspective of the thrust, the discrepancy of the rearmost rotors will be increased when the speed of the free stream is increased. The proposed analysis underestimates the thrust than that of the experimental result. Since the proposed analysis assumes that the strength of the vortex tube remains constant along the cylindrical wake, it does not take into account either the wake diffusion or decay. Such an assumption leads to the overestimation of the inflow at the rearmost rotors. Due to that, the thrust estimated by the proposed analysis is smaller than that of the experiment. Although such limitations reduce the accuracy of the proposed analysis, it is useful to capture the trend of the aerodynamic interference among the nonoverlapping multirotor configuration. In addition, the present analysis can predict the aerodynamic interference of a quadrotor configuration accurately. Thus, the proposed analysis is suitable for implementing flight simulation of the quadrotor UAV.

(a) Cross-shaped quadrotor

(b) Plus-shaped quadrotor

(c) Multirotor test configuration
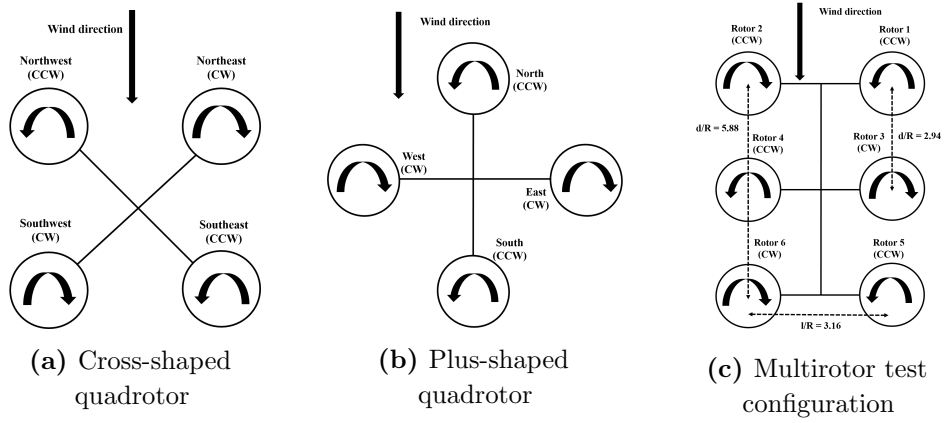
Figure 4.12 Schematics of various multirotor configurations (Ref. [91, 37])

(a) Thrust in terms of RPM

(b) Torque in terms of RPM

(c) Pitching moment in terms of RPM

(d) Rolling moment in terms of RPM

Figure 4.13 Comparison between the proposed analysis and CFD prediction: isolated rotor
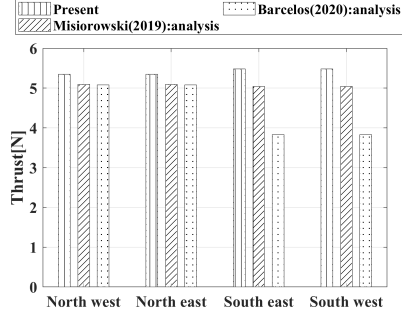
(a) Thrust in terms of the rotor location in a quadrotor
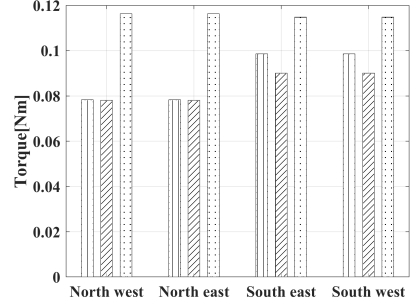
(b) Torque in terms of the rotor location in a quadrotor
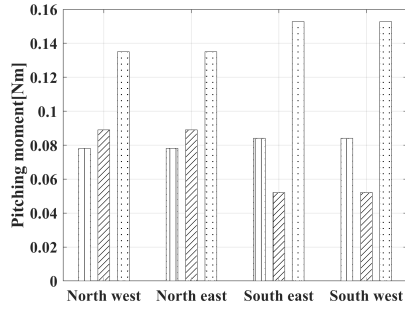
(c) Pitching moment in terms of the rotor location in a quadrotor

(d) Rolling moment in terms of the rotor location in a quadrotor

Figure 4.14   Comparison between the proposed analysis and CFD prediction: cross-shaped configuration

(a) Result of CFD prediction (Ref. [91])

(b) Result of the proposed analysis
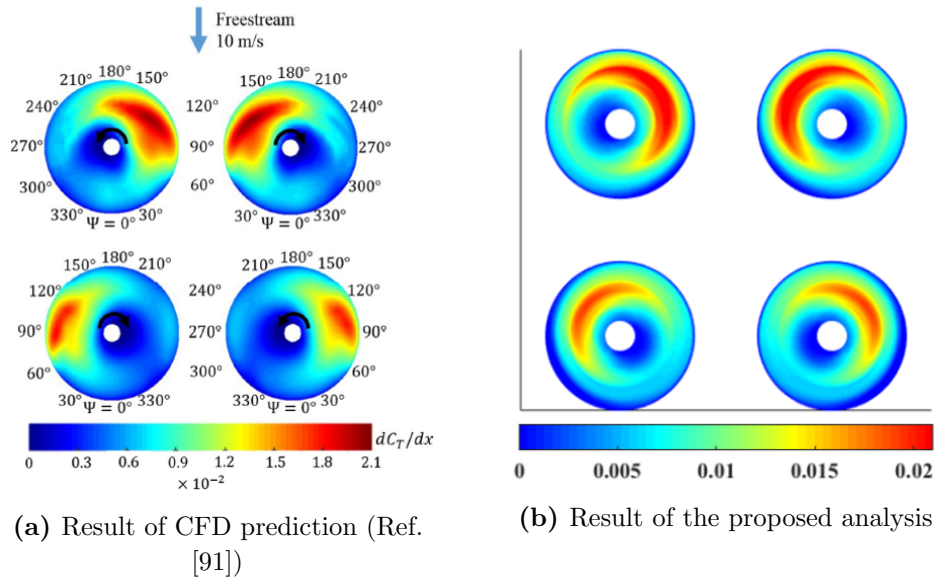
Figure 4.15 Comparison between the proposed analysis and CFD predictions: sectional thrust result of cross-shaped configuration
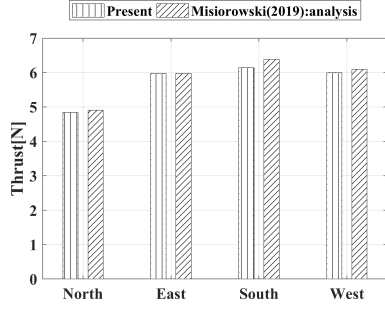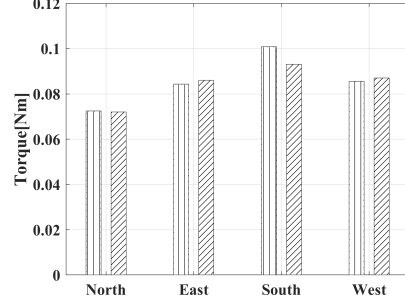
(a) Thrust in terms of the rotor location in a quadrotor

(b) Torque in terms of the rotor location in a quadrotor
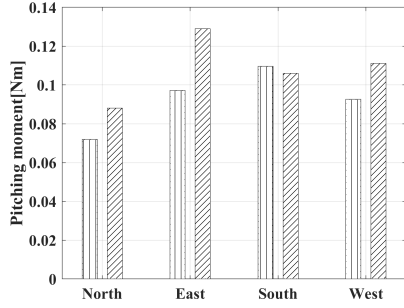
(c) Pitching moment in terms of the rotor location in a quadrotor

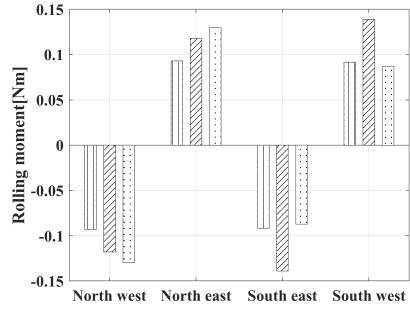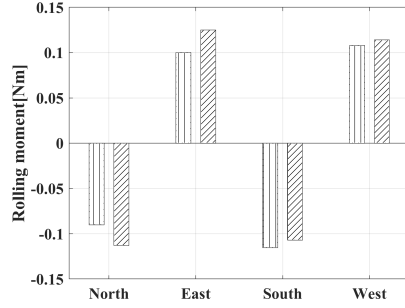**(d)** Rolling moment in terms of the rotor location in a quadrotor

Figure 4.16 Comparison between the proposed analysis and CFD prediction: plus-shaped configuration
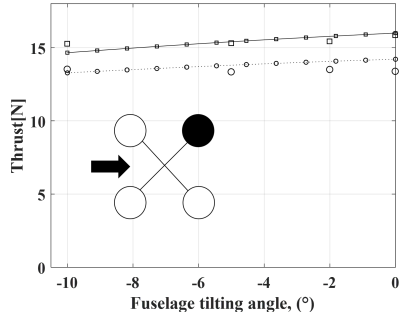
(a) Thrust in terms of the fuselage tilting angle
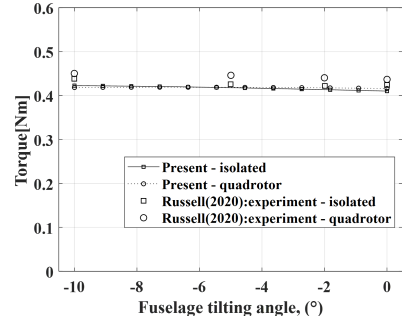
(b) Torque in terms of the fuselage tilting angle

Figure 4.17 Comparison between the proposed analysis and experimental results: quadrotor type
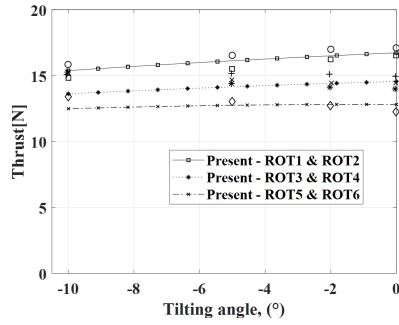
(a) Thrust: free-stream speed 6.1 m/s
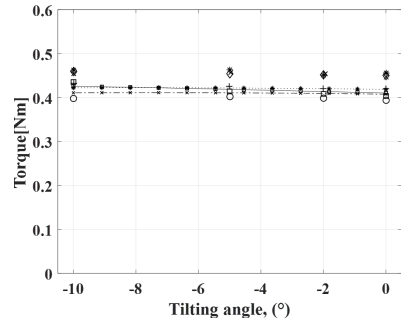
(b) Torque: free-stream speed 6.1 m/s
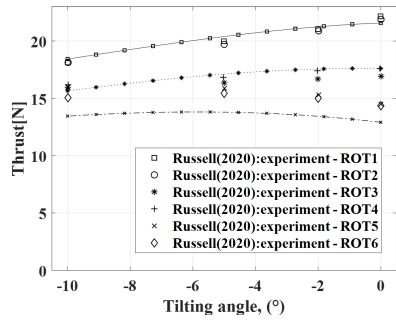
(c) Thrust: free-stream speed 12 m/s
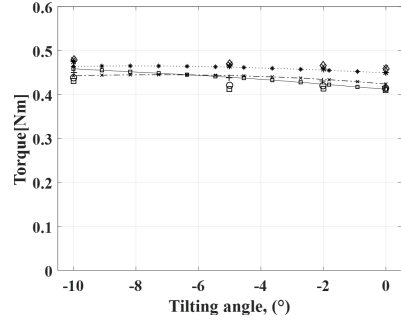
(d) Torque: free-stream speed 12.2 m/s

Figure 4.18 Comparison between the proposed analysis and experimental results: hexarotor type

95

Table 4.3 Details of the proposed analysis conditions for the quadrotor configuration (Ref. [91])

Configuration	cross type	plus type
Boom length, m	0.3048	0.3048
Rotational speed, RPM	Northwest/east: 4,058	North: 3,684
	Southwest/east: 4,495	East/West: 4,255
		South: 4,575
Free stream speed, m/s	10	10
Tilting angle (nose up: +), °	-5	-5

Table 4.4 Details of the proposed experimental conditions for the multirotor configuration (Ref. [37])

Configuration	quadrotor	hexarotor
Lateral length, l/R	3.16	3.16
Longitudinal length, d/R	2.94	2.94, 5.88
Rotational speed, RPM	2,000	2,000
Free stream speed, m/s	6.1	6.1, 12.2
Tilting angle (nose up: +), °	0, -5, -10	0, -5, -10

Table 4.5 Results for a cross-shaped quadrotor

Rotor location: North west	Present	Misiorowski (Ref. [91])	Discrepancy, %
Thurst, N	5.34	5.09	5.08
Torque, Nm	0.078	0.078	0.4
Pitching moment, Nm	0.078	0.089	-12.2
Rolling moment, Nm	-0.093	-0.118	-21.3
Rotor location: North east	Present	Misiorowski (Ref. [91])	Discrepancy, %
Thurst, N	5.34	5.09	5.08
Torque, Nm	0.078	0.078	0.4
Pitching moment, Nm	0.078	0.089	-12.2
Rolling moment, Nm	0.093	0.118	-21.3
Rotor location: South west	Present	Misiorowski (Ref. [91])	Discrepancy, %
Thurst, N	5.48	5.04	8.7
Torque, Nm	0.098	0.09	9.4
Pitching moment, Nm	0.084	0.052	-34.0
Rolling moment, Nm	-0.092	-0.139	-61.7
Rotor location: South east	Present	Misiorowski (Ref. [91])	Discrepancy, %
Thurst, N	5.48	5.04	8.7
Torque, Nm	0.098	0.09	9.4
Pitching moment, Nm	0.084	0.052	-34.0
Rolling moment, Nm	0.092	0.139	-61.7

Table 4.6 Results for a plus-shaped quadrotor

Rotor location: North	Present	Misiorowski (Ref. [91])	Discrepancy, %
Thurst, N	4.84	4.90	-1.3
Torque, Nm	0.072	0.072	0.6
Pitching moment, Nm	0.072	0.088	-18.2
Rolling moment, Nm	-0.090	-0.113	-20.2
Rotor location: South	Present	Misiorowski (Ref. [91])	Discrepancy, %
Thurst, N	6.14	6.38	-3.7
Torque, Nm	0.10	0.093	8.38
Pitching moment, Nm	0.109	0.106	3.4
Rolling moment, Nm	-0.115	-0.107	7.9
Rotor location: East	Present	Misiorowski (Ref. [91])	Discrepancy, %
Thurst, N	5.98	5.97	0.1
Torque, Nm	0.084	0.086	-1.9
Pitching moment, Nm	0.0972	0.129	-24.6
Rolling moment, Nm	0.10	0.125	-19.9
Rotor location: West	Present	Misiorowski (Ref. [91])	Discrepancy, %
Thurst, N	5.99	6.09	-1.6
Torque, Nm	0.085	0.087	-1.7
Pitching moment, Nm	0.093	0.111	-16.6
Rolling moment, Nm	0.108	0.114	-5.4

4.2.3 Further investigation of the aerodynamic interference for a multirotor UAV

To perform forward flight of a quadrotor UAV, a fuselage tilting angle will be necessary due to the flight characteristics which use a difference in thrust between the front and rear rotors. The specific tilting angle is matched with the certain forward flight of such UAV. It means that the influence of the aerodynamic interference will differ among the flight conditions. Due to that, it is crucial to investigate such influence for the identification of the interference for a quadrotor UAV. The following two investigations will be performed. First, the evaluation of the trend under the free-stream speed is performed. The specifications of UAV and operating rotational speed are based on the previous section. In addition, $0\,°$, $-15\,°$, and $-30\,°$ are used for the fuselage tilting angle. Then, a trim analysis is performed, which focuses on investigating a critical interference situation. This trim analysis, described in Section 3.1.2, is utilized to find the trim state of a quadrotor UAV. For trim analysis, the flight speed, fuselage tilting angle, and rotational speed of each rotor are selected as the trim variables. To obtain the trim result, an optimization algorithm 'fmincon' is used in MATLAB. The optimization algorithm relies on an interior point method that uses Hessian approximation. Based on the previous studies (Refs. [119, 120]), the gross weight of UAV is assumed as 2 kg. Since the fuselage drag coefficient is not explicitly specified, it is estimated based on the previous research (Ref. [76]). The relevant description will be introduced in Chapter 5.

The aerodynamic load on the front rotor is presented in Figure 4.19. A comparison between the results with and without the interference is performed. These results

show that an average discrepancy is less than 5%, and it means that the aerodynamic interference for the front rotor is insignificant. Consequently, during a forward flight of a quadrotor UAV, the interference of the front rotor may be disregarded. As shown in Figure 4.20, the trends observed from the result of the rear rotor show notable discrepancies. The result of the thrust shown in Fig. 4.20(a) exhibits that the discrepancy is increased when the free-stream speed is increased at 0° fuselage tilting angle. At a free-stream speed of 15 m/s, the discrepancies in the thrust results are 20% for 0°, 12% for -15°, and 7% for -30° fuselage tilting angle.

Figure 4.20(b) illustrates that the discrepancy in torque at 0° fuselage tilting angle shows a unique feature. When the speed is smaller than 6 m/s, the torque with interference is smaller than the result without the interference. However, when the speed is larger than 6 m/s, both results are overlapped. Then, the torque result with the interference is larger than the result without the interference. The reason for this is that the aerodynamic interference leads to an increase in the amount of the inflow when the flight speed is increased. Due to that, the lift of the rotor is decreased and the torque of the rotor is increased when the interference effect becomes significant. The results of -15° and -30° fuselage tilting angle show a decreasing trend when considering the interference. As shown in Figs. 4.20(c) and (d), the results for the pitching and rolling moments show a similar tendency as observed in the thrust. These results suggest that the interference of the rear rotor is significantly influenced by the variables such as a small fuselage tilting angle and high free-stream speed.

However, the different rotational speed between the front and rear rotors is required to achieve forward flight due to the features of a quadrotor UAV. For

that, trim analysis is performed to consider such features, and the relevant results are illustrated in Fig. 4.21. As shown in Fig. 4.21 (a), the result of a fuselage tilting angle in terms of the flight speed shows a similar trend in both approaches with and without the interference. However, the result of the rotational speed shows a different trend. Fig. 4.21(b) illustrates that the rotational speed of the front rotors is decreased than that of the result without the interference. In addition, the rotational speed of rear rotors is increased with consideration of the interference. The reason for this is that the interference reduces the thrust of the rear rotor. Thus, to balance the pitching moment of a quadrotor UAV, an increase in the rotational speed of the rear rotor and a decrease in the rotational speed of the front rotor will be required. By the trim analysis, a notable founding is observed.

Figure 4.21(b) illustrates that the discrepancy of the rear rotors with and without the interference is not significant when the flight speed is smaller than 2 m/s. As the flight speed reaches a certain value, the discrepancy will be increased and the maximum discrepancy in the rotational speed will occur at 10,° fuselage tilting angle and a flight speed of 7 m/s. As the flight speed becomes larger, the discrepancy will be decreased. To investigate this trend, an additional comparison is conducted using the rotational speed, tilting angle, and flight speed from the trim results. Figure 4.22 indicates that the thrust results have significant discrepancies when compared against the other results. Specifically, at a flight speed of 7 m/s, the inclusion of the interference causes a 9% decrease in thrust compared against the result without the interference. These findings lead to several notable observations. First, interference does not play a significant role at high speeds when the fuselage tilting angle is

large. Figure 4.20 displays the relevant trends. Second, it is noteworthy that a different trend is observed in the results obtained from both the trim analysis and the investigation under the free-stream condition. As illustrated in Fig. 4.20(a), a significant interference occurs at the rear rotor under the condition in which is a small fuselage tilting angle and high free-stream speed. However, the trim analysis suggests that the maximum interference is observed at a specific flight speed and tilting angle. The level of the interference obtained by the trim analysis is less pronounced than that during the free-stream analysis. Despite the interference being smaller than under the free-stream condition, it is still significant for the rear rotor of a quadrotor UAV. In addition, another physical quantity such as the rotor power is used to investigate the effect of the aerodynamic interference. The investigation result is shown in Fig. 4.23 and three flight conditions such as low, mid, and high speed are selected to identify the interference effect. Based on this result, the following findings are obtained. First, the low and high-speed conditions show that the rotor power is increased when aerodynamic interference is considered. But, the discrepancy between results with and without the interference is not significant. Second, the maximum discrepancy of the rotor power is observed for mid-speed condition. Specifically, the variation of the rear rotor power is significant. Furthermore, an additional investigation is performed to identify the effect of aerodynamic interference by the nth to the kth rotor. The analysis conditions are set to five cases. Case 2 indicates that only the interference relationship considers the effect of Rotor 1 on Rotor 2. The other cases are summarized in Table 4.6. The relevant result is shown in Fig. 4.24. By this result, the dominant power variation is observed in Case 4. These findings indicate that

103

the consideration of the aerodynamic interference is crucial to estimate the proper characteristics of a multirotor UAV.

However, the proposed formulation has a limitation and weakness to predict the rolling and pitching moments. As those moments significantly relate to the flight dynamics, it will be required to identify the precision of multirotor UAV flight simulation when the prediction accuracy of the rolling and pitching moments is degraded. The relevant comparison is performed and based on the trim analysis. Prior to comparison, the pitching moment obtained by the proposed analysis is overestimated than that of the CFD result as shown in Fig. 4.14. Due to that, the magnitude reduction of the proposed result is performed and applied to trim analysis. The relevant result is shown in Fig. 4.24. Results with and without correction show a similar trend and the discrepancy in the rotational speed is within a reasonable range. Based on such result, the proposed analysis is capable of predicting the dynamic trend of a multirotor UAV properly. Therefore, to obtain more precise rotor aerodynamics for the flight simulation, the aerodynamic interference among the rotors should be included.
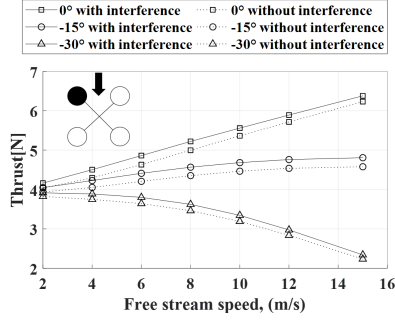
(a) Thrust of the front rotor in quadrotor
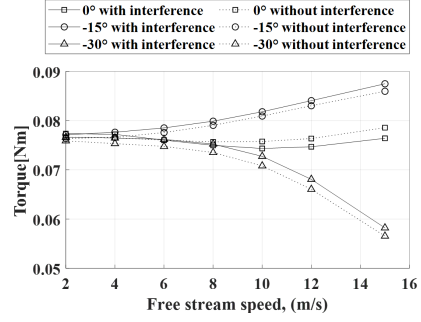
(b) Torque of the front rotor in quadrotor
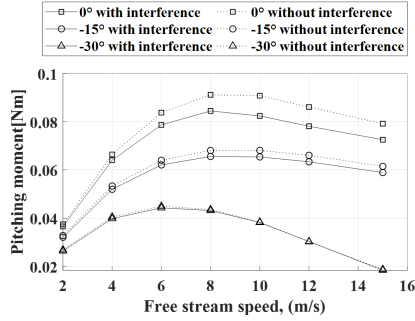
(c) Pitching moment of the front rotor in quadrotor
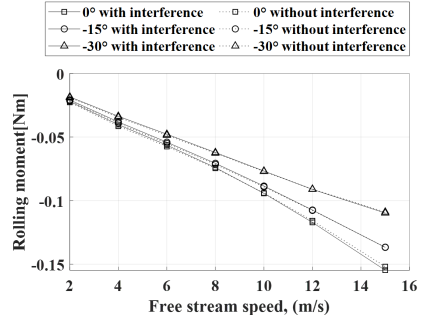
(d) Rolling moment of the front rotor in quadrotor

Figure 4.19 Results for the front rotor in terms of the free-stream speed
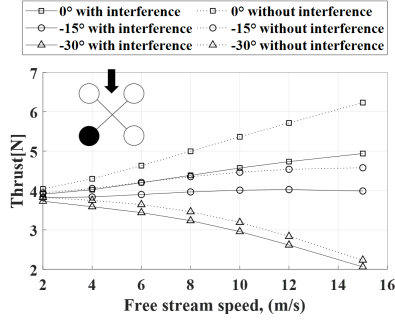
(a) Thrust of the rear rotor in quadrotor
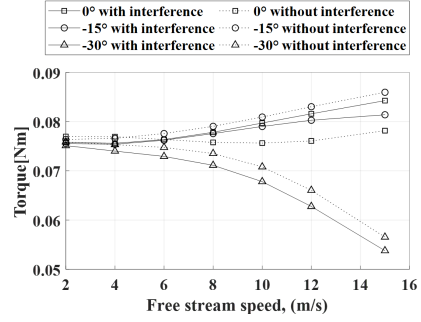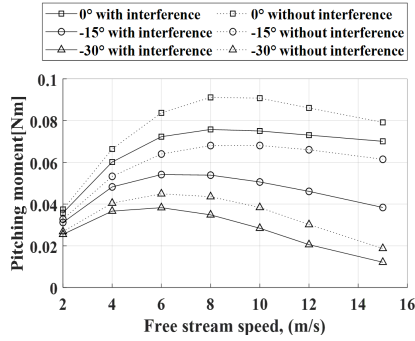
(b) Torque of the rear rotor in quadrotor

(c) Pitching moment of the rear rotor in quadrotor
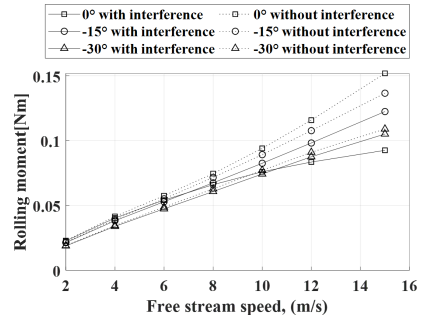
(d) Rolling moment of the rear rotor in quadrotor

Figure 4.20   Results for the rear rotor in terms of free-stream speed
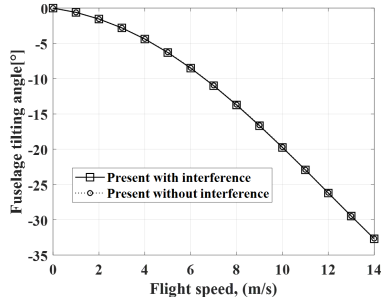
(a) Fuselage tilting angle
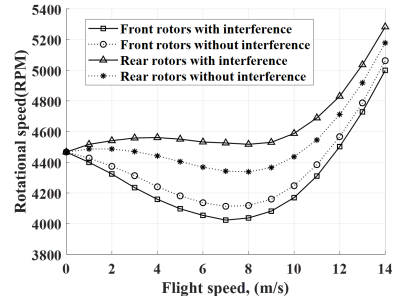
(b) Rotational speed of the rotor

Figure 4.21   Trim analysis for forward flight with and without interference in terms of forward speed
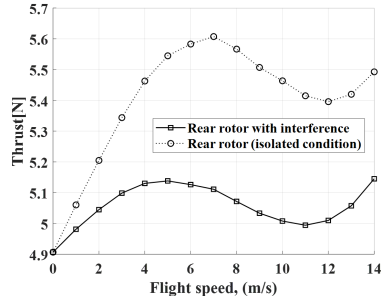
(a) Thrust of the rear rotor in quadrotor
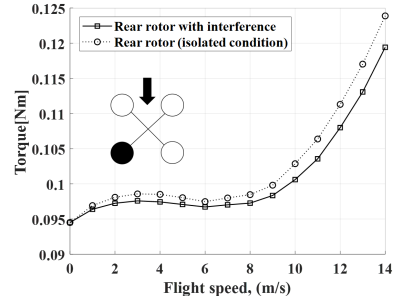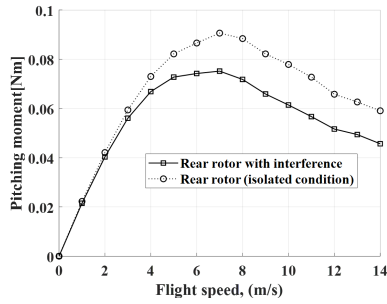
(b) Torque of the rear rotor in quadrotor

(c) Pitching moment of the rear rotor in quadrotor
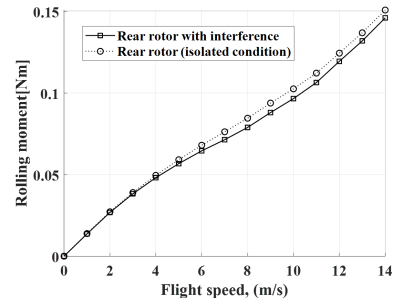
(d) Rolling moment of the rear rotor in quadrotor

Figure 4.22   Comparison results for the rear rotor based on the trim analysis
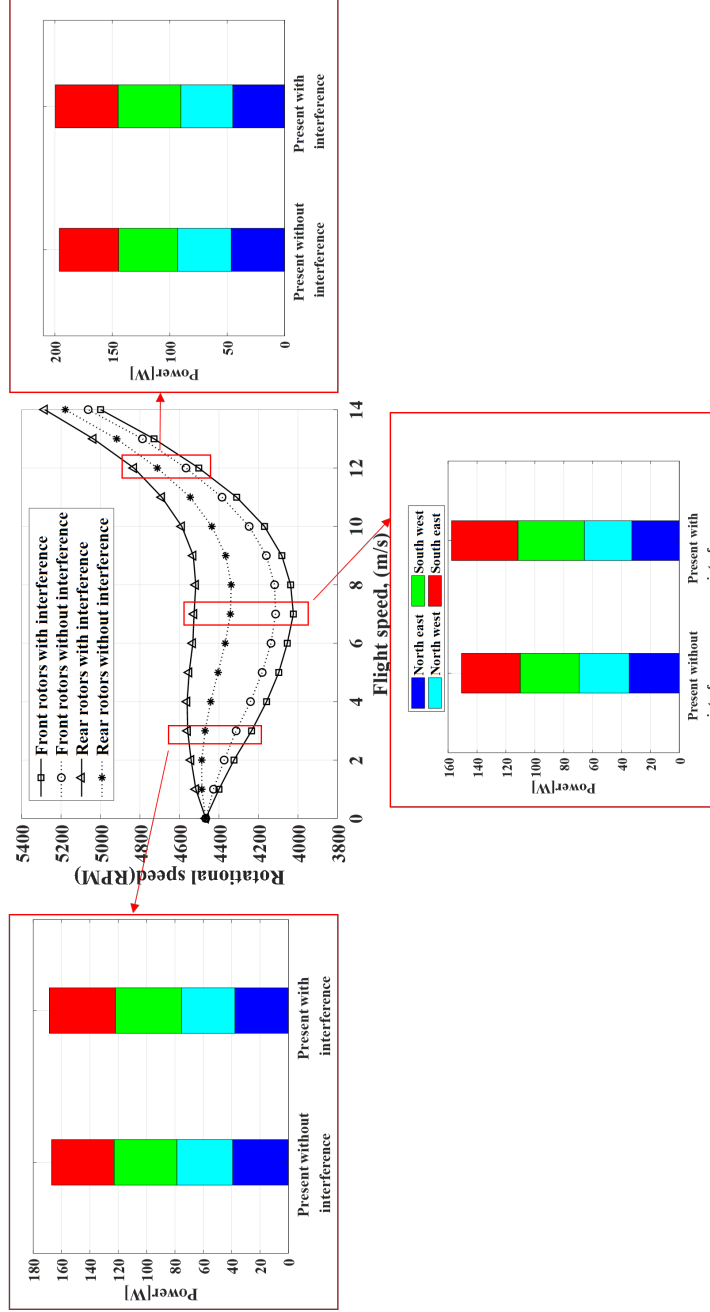
Figure 4.23 Comparison rotor power result based on trim condition of quadrotor UAV

108
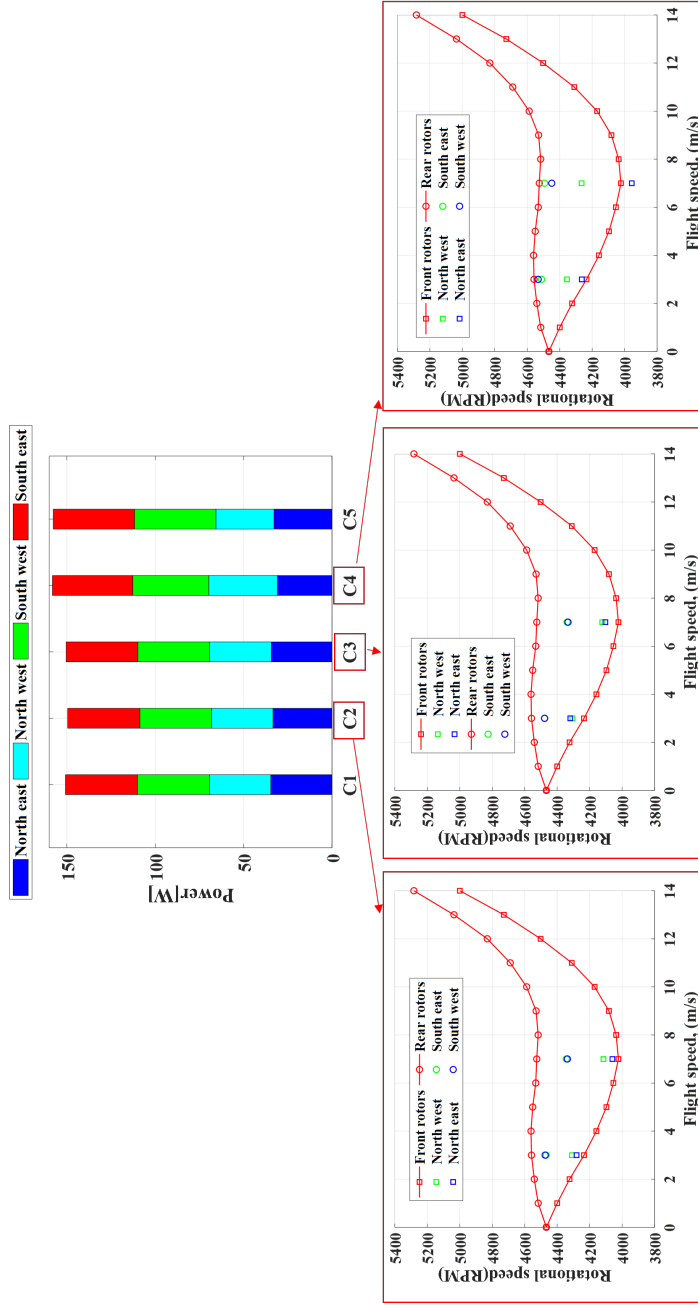
Figure 4.24 Effect of the aerodynamic interference by n^{th} to k^{th} rotor

109
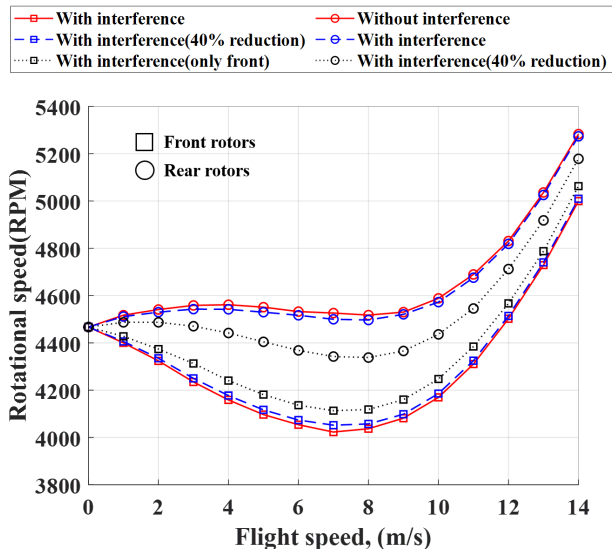
Figure 4.25 Comparison rotational speed based on trim condition of quadrotor UAV

Table 4.7   Analysis conditions

Case1, C1	No interference
Case2, C2	Rotor 1 - Rotor 2
Case3, C3	Rotor 1 - Rotor 3
Case4, C4	Rotor 1 - Rotor 4
Case5, C5	All considering

5 Verification of the Multirotor UAV Flight Simulation

5.1 Introduction of the verification procedure

This dissertation is focused on the establishment of the multirotor UAV flight simulation which can estimate the dynamic response of multirotor UAV accurately. For that in the previous section, the proposed rotor aerodynamics analysis is verified to capture the correct aerodynamic features of multirotor UAV, including the aerodynamic interference among the rotors. However, as the flight simulation is a combination of several modules such as the control law, those modules will be needed to be verified by a systematic procedure. Due to that, a systematic procedure for the present flight simulation consists of the following steps: 1) The validation for the aerodynamics of the rotor is performed. Although the proposed rotor analysis developed in this dissertation shows good agreement with the several rotor blades, there is still room to verify it for the rotor blade of the target UAV. For that, three-dimensional scanning is performed to obtain the blade geometry such as airfoil, chord length, and twist angle according to the span location (Ref. [103]). Furthermore, the experimental result for an isolated rotor is obtained to evaluate the present rotor aerodynamic

112

analysis. 2) Then, the dynamic characteristic of a multirotor UAV is verified. As that characteristic is dependent on the control law, it is necessary to be identified. However, the control schemes of the target UAV are not publicized. For that, the system identification approach is attempted to estimate such schemes using the flight tests and hardware in the loop simulation (HILS). Comprehensive Identification from Frequency Responses (CIFER) program (Ref. [102]) developed by the U.S. Army Aviation and USRA NASA Academic Mission Services (NAMS) is used for such identification procedure. 3) The fuselage aerodynamics is evaluated by the flight tests. The flight tests are performed to obtain the result of the three translational velocities such as the longitudinal, lateral, and altitude direction. 4) Based on the previous steps, the trim analysis is performed to find the physical constraint of the target UAV. Based on this process, the limitation of the rotor speed is reflected in the flight simulation. 5) The two-point path flight test is performed to validate the accuracy of the present flight simulation. Several parameters such as the trajectory, fuselage tilting angle, and velocity are compared and used for the verification. After the process for that flight test, the gust experiment is used to evaluate the fidelity of the present flight simulation. The present systematic procedure is illustrated in Fig. 5.1.
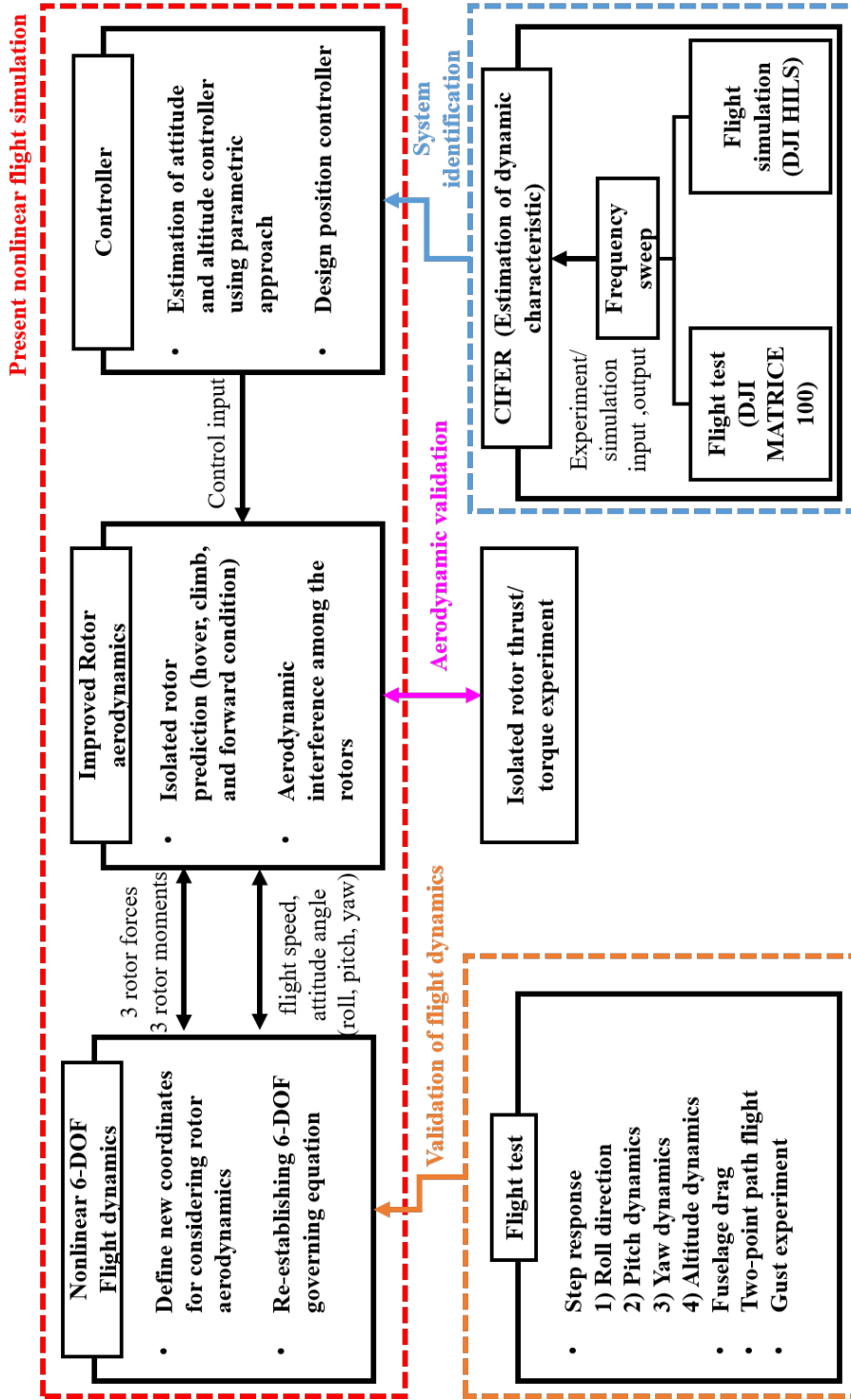
Figure 5.1   Detailed procedure for verification of the present flight simulation

114

5.2 Validation of modules in flight simulation

5.2.1 Specification of the UAV

The target UAV used in this dissertation is DJI MATRICE 100. That UAV has the following specifications: 1) Blade diameter is 13 inches. As the parameters such as blade chord length, twist angle, and airfoil according to span location are not publicized, three-dimensional scanning (Ref. [103]) is performed to obtain those parameters. XFOIL (Ref. [108]) is applied to obtain the result of the aerodynamic coefficient of each airfoil section. 2) The length of the boom is 325 mm. The configuration of UAV is a quad-rotor and cross shape. In addition, the gross weight of the UAV is 3.2 kg. 3) HILS is supported by the manufacturer to evaluate user custom code embedded in the flight control computer (FCC). In Table 5.1, the relevant specification of the UAV is summarized. Figure 5.2 (a) illustrates the target UAV. Furthermore, the configuration of the target blade and the result of three-dimensional scanning are illustrated in Figs. 5.2 (b) and (c).

(a) Entire vehicle configuration
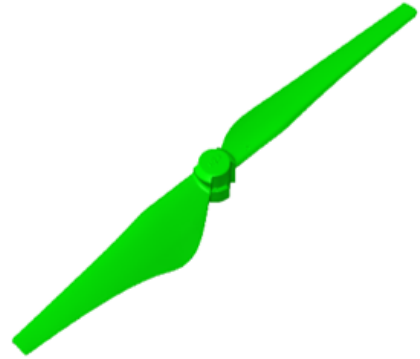
(b) Blade configuration: DJI1345T
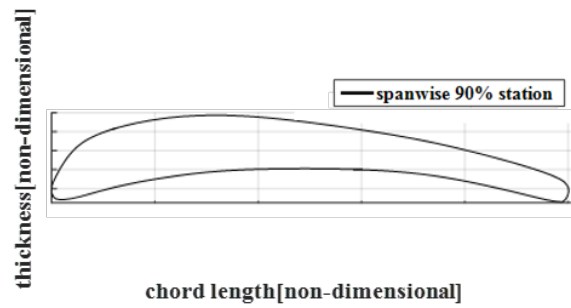
(c) Result of three dimensional scanning

Figure 5.2 Specification of the present UAV configuration

Table 5.1 Specification of the UAV

UAV geometry	value [unit]	Blade geometry	value [unit]
Boom length	0.325 [m]	Diamter	0.3302 [m]
I_{xx}(Ref. [121])	0.0554 [$kg\ m^2$]	Twist	-12.28 [°]
I_{yy}(Ref. [121])	0.0578 [$kg\ m^2$]	Unit mass	0.0515 [kg/m]
I_{zz} (Ref. [121])	0.1067 [$kg\ m^2$]	N. of rotor	4 [EA]
Gross weight	3.2 [kg]	N. of a blade per rotor	2 [EA]

5.2.2   Validation for the aerodynamics of the target rotor

The rotor aerodynamic analysis used in this dissertation is validated and compared by various rotor blades described in Section 4. In this section, the validation process for the target rotor blade, DJI1345T, is performed. It is necessary to evaluate the aerodynamic analysis of the target blade under various flight conditions such as hover, climb, and forward. However, the climb and forward experiments are not performed in this dissertation. Although there are no experiments on the wind tunnel experiment, the present aerodynamic analysis is capable of predicting the aerodynamic performance of the rotor accurately. Thus, the following procedure is performed to validate and investigate the aerodynamic performance of the target rotor blade.

First, an experiment facility to measure the static thrust and torque is established as illustrated in Fig. 5.3. As shown in Fig. 5.3 (a), the commercial kit which is capable of measuring thrust and torque is used to obtain the result. To generate the smooth stream of the rotor wake, a side wall is installed at both sides of the experiment facility. Based on this experiment, the thrust and torque obtained by the experiment are compared by the present rotor aerodynamics, and these results are shown in Fig. 5.4. Even though the torque is underestimated, there is only an average discrepancy of 9%. By this comparison, the proposed aerodynamic analysis can predict the aerodynamic load of the target rotor.

Then, the investigations of the forward flight and climb conditions for the target rotor blade are performed. Based on six fuselage tilting angles such as $0°$, $10°,20°,30°,60°$, and $90°$, the trend of the four aerodynamic loads, which are the

thrust, torque, forward, and sideward forces, are analyzed. The fuselage tilting attitude of $0\,^{\circ}$ means the edgewise flight condition and the axial climb condition can be predicted when the fuselage tilting angle is $90\,^{\circ}$. In contrast to a conventional rotorcraft, the rotational speed of the rotor is to be varied. Due to that, the aerodynamic performance of the rotor may show a different trend with respect to the rotational speed. Thus, the nominal rotational speed to maintain the hover condition is used in this procedure. That rotational speed is based on the gross weight of the target UAV and selected at 4,500. As illustrated in Figure 5.5, an increase in the fuselage tilting angle leads to a decrease in thrust, while a small tilting attitude increases thrust. When the fuselage is tilted at a $90°$ angle, equivalent to a climb position, the thrust reaches zero at an advance ratio of 0.15. Furthermore, an increase in the fuselage tilting angle causes a reduction in torque. In contrast to thrust and torque, the drag is maximum when the tilting angle is $0°$ and gradually reduces to zero as the tilting angle approaches $90°$. By these results, the aerodynamic features of the target rotor blade are investigated. In addition, the verification for the aerodynamic analysis module is accomplished to ensure the accuracy of the flight simulation.

(a) Front view of the experimental facility

(b) Rear view of the experimental facility
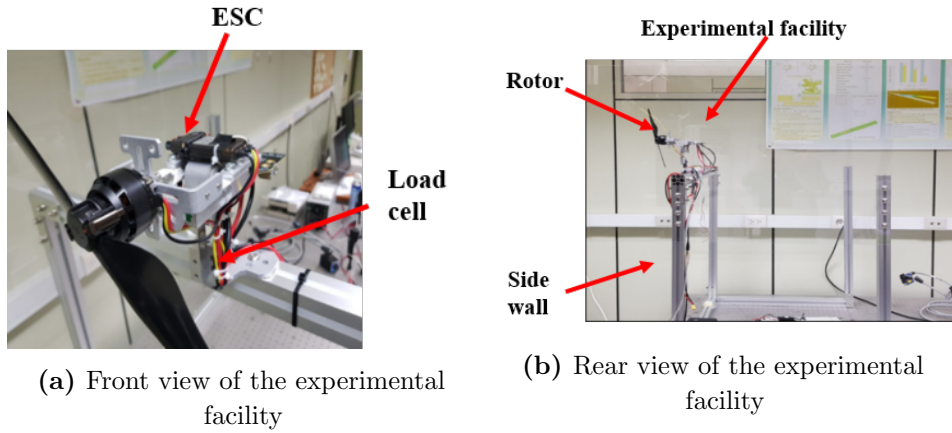
Figure 5.3   Present static experimental facility
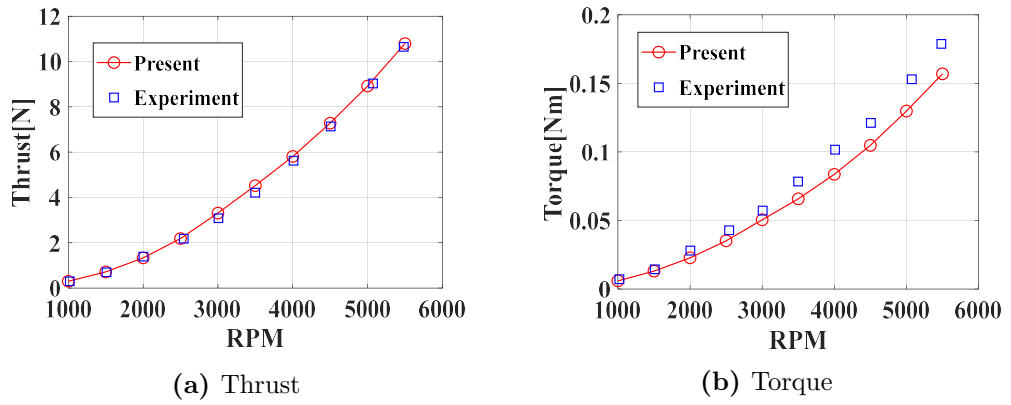
(a) Thrust

(b) Torque

Figure 5.4   Comparison of the present aerodynamics analysis in hover
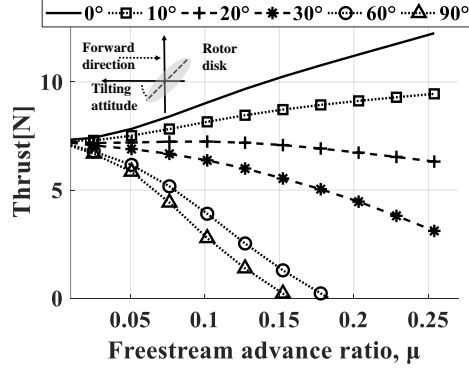
(a) Thrust
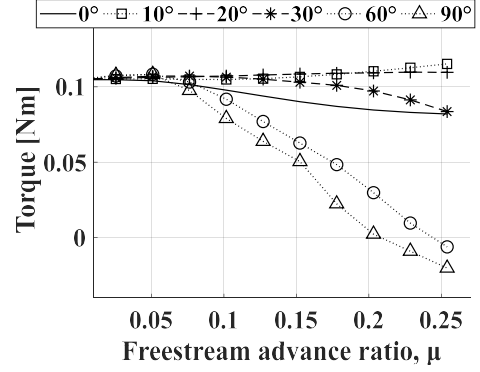
(b) Torque
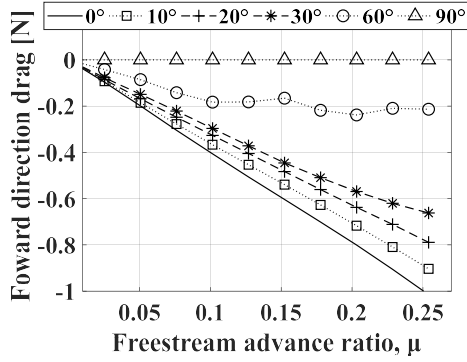
(c) Forward drag
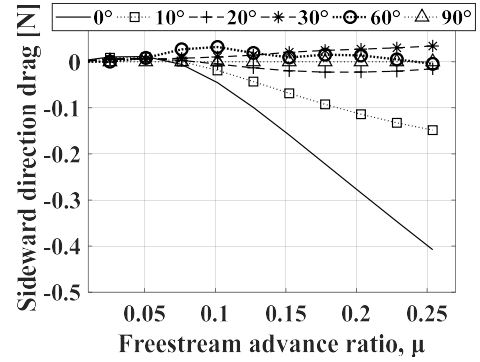
(d) Sideward drag

Figure 5.5   Results for the various flight conditions

5.2.3 Verification of the dynamic characteristics of the target UAV based on system identification

To perform the flight simulation, information on the control law will be needed. However, the attitude and altitude controllers of DJI MATRICE 100 have not been publicized. Due to that, frequency sweep tests are performed for a total of four axes: roll, pitch, yaw, and altitude. As described in Eq. 3.16, the magnitude of sweep A_{sw} is set to $3°$, and frequency $\omega_{sw_{min}}$ is 0.1 Hz for the experiment. The equilibrium tilting angle is $0°$; however, the altitude should be greater than zero. Thus, the frequency sweep experiment for the altitude is performed at 10 m and a sweep magnitude of 1 m. The initial frequency is set as 0.05 Hz, and the duration of the experiment lasts for 100 sec.

The results for the rolling direction are shown in Fig. 5.6 (a). In addition, the frequency sweep for pitching, yawing, and altitude is performed for the same procedure to obtain the results. The transfer functions for each axis are derived using CIFER. As each axis is equipped with its controller, the denominator of the transfer function is determined to be in the third order based on the linearized flight dynamics equation, and the controller is implemented in flight simulation. The control scheme consists of a cascade system, with the modified PID as the outer loop and the modified PID as the inner loop. Figures 5.6 (b), (c), and (d) show Bode diagrams and coherence of the rolling data derived by CIFER. The results show that the coherence value is close to 1, thus suggesting a good estimation. The details of the transfer function obtained from the experiment are summarized in Eq. 5.1.

$$\begin{bmatrix} \phi_{dirc} \\ \theta_{dirc} \\ \psi_{dirc} \\ Z_{dirc} \end{bmatrix} = \begin{bmatrix} \frac{1032.9}{s^3+19.67s^2+226.44s+1032.9} \\ \frac{1032.9}{s^3+19.67s^2+226.44s+1032.9} \\ \frac{2079.8}{s^3+137.35s^2+454.2s+2079.8} \\ \frac{10.64}{s^3+13.22s^2+39.11s+10.64} \end{bmatrix} \qquad (5.1)$$

The derived transfer functions for rolling, pitching, yawing, and altitude are compared with the experimental results, as shown in Fig. 5.7. The roll, pitch, and yaw axes for an input frequency of less than 3 Hz show a discrepancy of 5%, confirming the good agreement. However, the measured data of the altitude has the following issue. The precision of GPS to predict the altitude is 0.5 m supported by the manufacturer. Due to that, the data obtained by GPS may have such uncertainty when the altitude is smaller than that range. The relevant discrepancies are illustrated in Fig. 5.7 (d), which is indicated by an arrow. When estimating the transfer function using the flight test result, the tendency is consistent with the experimental results at lower frequencies. However, the transfer function obtained from the flight test does not predict the dynamic characteristics of the altitude. Due to this issue, a transfer function is additionally derived using the hardware in the loop simulation (HILS), which is provided by the manufacturer. The result of a transfer function obtained by HILS is validated by the following procedure. The tendency of the transfer function obtained by HILS is compared against both flight test result and transfer function derived by the flight test. At a low-frequency range, these results are matched well as shown in Fig. 5.7 (d). As the high-frequency range contains uncertainties, that range is not compared. Instead of that, the result of HILS shows that the decrease in the gain and the phase delay phenomenon are well captured while increasing

123

the frequency. Based on this comparison, the transfer function obtained by HILS is capable of capturing the altitude characteristics of the target UAV. Thus, the transfer function obtained by HILS is selected to estimate the controller.

Although these transfer functions obtained by the system identification include the dynamic characteristics in each direction, it is not straightforward to identify the control gains. The controller used in this dissertation is described in Eq. 5.2.

$$
\begin{bmatrix}
X^d \\
Y^d \\
Z^d \\
\dot{Z}^d \\
\phi^d \\
\theta^d \\
\psi^d \\
\dot{\phi}^d \\
\dot{\theta}^d \\
\dot{\psi}^d
\end{bmatrix}
=
\begin{bmatrix}
(k_p^X X_e - k_d^X \dot{X}) \\
(k_p^Y Y_e + k_i^Y \int Y_e - k_d^Y \dot{Y}) \\
(k_p^Z Z_e + k_i^Z \int Z_e - k_d^Z \dot{Z}) \\
f_{sat}(k_p^{\dot{Z}} \dot{Z}_e - k_d^{\dot{Z}} \ddot{Z}, \dot{Z}_{lim}) \\
f_{sat}(k_i^{\phi} \int \phi_e - k_p^{\phi} \phi - k_d^{\phi} \dot{\phi}, \phi_{lim}) \\
f_{sat}(k_i^{\theta} \int \theta_e - k_p^{\theta} \theta - k_d^{\theta} \dot{\theta}, \theta_{lim}) \\
k_i^{\psi} \int \psi_e + k_p^{\psi} \psi_e - k_d^{\psi} \dot{\psi} \\
f_{sat}(k_p^{\dot{\phi}} \dot{\phi}_e - k_d^{\dot{\phi}} \ddot{\phi}, \dot{\phi}_{lim}) \\
f_{sat}(k_p^{\dot{\theta}} \dot{\theta}_e - k_d^{\dot{\theta}} \ddot{\theta}, \dot{\theta}_{lim}) \\
f_{sat}(k_p^{\dot{\psi}} \dot{\psi}_e - k_d^{\dot{\psi}} \ddot{\psi}, \dot{\psi}_{lim})
\end{bmatrix}
\tag{5.2}
$$

where,

$$
f_{sat}(S_{in}, S_{lim}) =
\begin{cases}
-S_{lim} & (S_{in} < -S_{lim}) \\
S_{in} & (-S_{lim} \leq S_{in} \leq S_{lim}) \\
S_{lim} & (S_{in} > S_{lim})
\end{cases}
$$

Controllers consist of the position, attitude, and rate. The subscript e denotes the discrepancy between the desired input and state variable. The superscript d means

124

the desired input. k_i, k_d, and k_p are the control gain of PID. To consider the physical constraint of UAV, the saturation function will be applied. By the experiment, the response of ϕ and θ have smaller overshoot characteristics than the other control variables do. For that reason, an I-PD configuration (Ref. [122]) is applied in both ϕ and θ controllers. And an I-type controller is added to Y direction because the gust generated by the wind tunnel will occur in Y direction. To find the control gain described in Eq. 5.1, the result of an additional experiment such as the step response is applied. Each control gain is matched and corrected. The attitude and altitude dynamics in hover are verified by applying a step input to each axis. The duration of the roll or pitch is shorter than those for the other experiments because UAV advances when a step function is applied. The input angle of the roll and pitch was $5\,^\circ$, the yaw angle was $40\,^\circ$, and the altitude ascended from 5 to 7 m. First, compared against the flight simulation results shown in Fig. 5.8, the roll, pitch, and yaw angles show an average discrepancy of less than 5%, which is relatively consistent with the present simulation. In addition, the average discrepancy of the altitude is less than 2.5%, which is similar to that in the actual flight condition. This shows that the attitude and altitude dynamics are well verified. The details of the control gains are summarized in Table 5.2.

(a) Roll frequency sweep experiment

(b) Magnitude of the transfer function in roll

(c) Phase of the transfer function in roll

(d) Coherence of the transfer function in roll
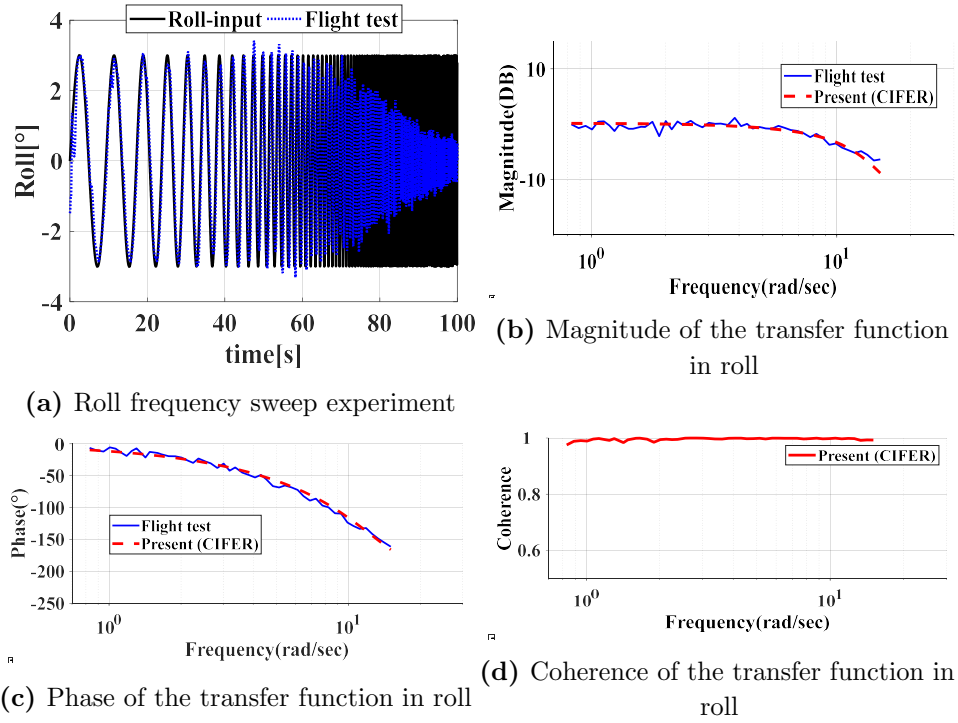
Figure 5.6 System identification results using CIFER

126
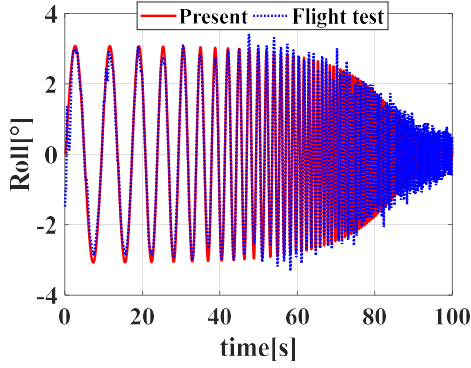
(a) Result of the roll transfer function
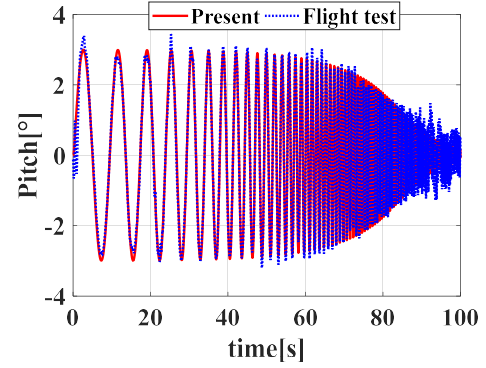
(b) Result of the pitch transfer function
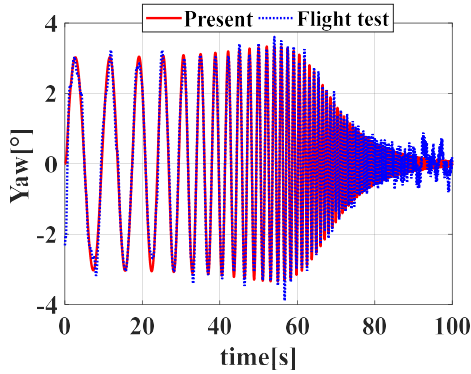
(c) Result of the yaw transfer function
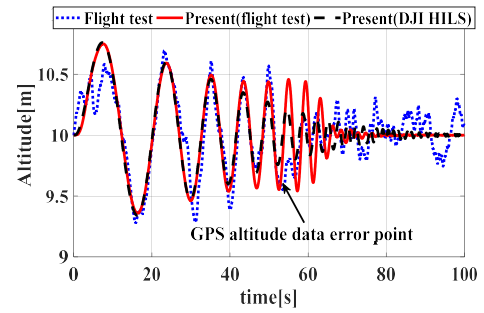
(d) Result of the altitude transfer
function

Figure 5.7　Transfer function of the attitude and altitude

127
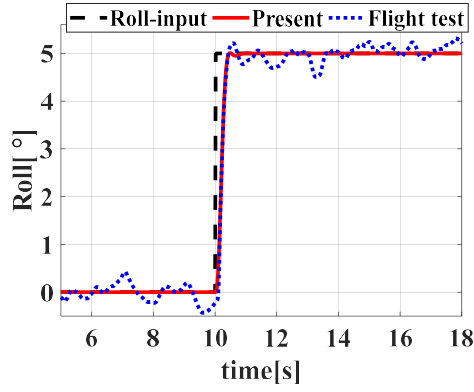
(a) Roll step response
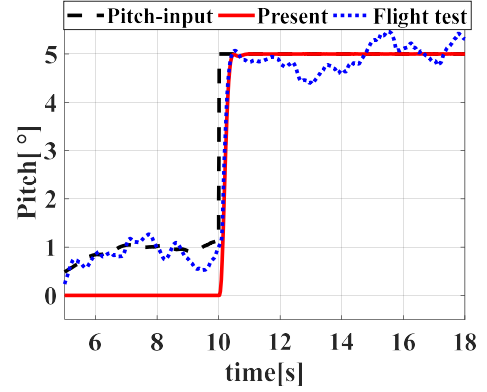
(b) Pitch step response
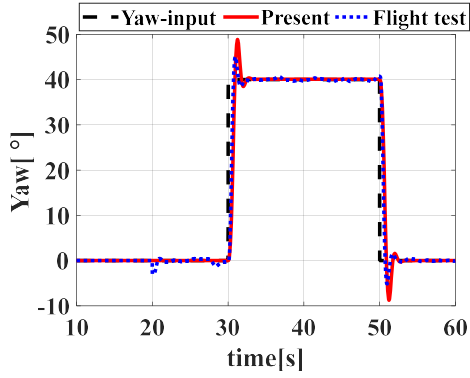
(c) Yaw step response
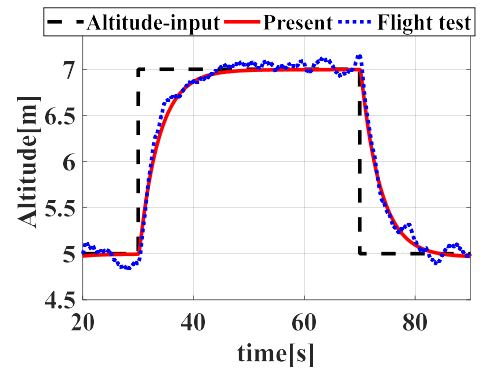
(d) Altitude step response

Figure 5.8   Validation of the flight dynamics by the step response

Table 5.2 Specification of the control gain and physical constraint

	$k_p^{(var)}$	$k_d^{(var)}$	$k_i^{(var)}$		$k_p^{(var)}$	$k_d^{(var)}$	$k_i^{(var)}$		value[unit]
X	0.32	0.50	-	θ	2.2996	0.0367	11.1839	$\dot{Z}_{lim}$	5[m/s]
Y	0.1035	0.477	0.0112	ψ	2.0217	0.2218	0.0087	ϕ_{lim}	30[°]
Z	1.1750	4.0111	0.0192	$\dot{\phi}$	8.4601	0.4637	-	θ_{lim}	5[°]
$\dot{Z}$	3.3349	4.9372	-	$\dot{\theta}$	8.4615	0.4462	-	$\dot{\phi}_{lim}$	150[°/s]
ϕ	2.2989	0.0385	11.1749	$\dot{\psi}$	9.3977	3.7972	-	$\dot{\theta}_{lim}$	150[°/s]
								$\dot{\psi}_{lim}$	150[°/s]

5.2.4   Estimation of the fuselage aerodynamics

As indicated in Section 3.1.2, it is assumed that the drag coefficient remains constant. To establish its appropriate value, it is possible to utilize either CFD analysis or experiments. Weerasinghe and Monasor (Ref. [123]) conducted both approaches and found a strong correlation between the two results. Therefore, an experimental method is applied to determine the drag coefficient in this dissertation. Measuring the drag of the fuselage in flight tests will be challenging. Thus, an alternative parameter is required to confirm the accuracy of the drag coefficient. To achieve this, the speed in each axis is examined and confirmed through the present flight simulation. Equation 3.10 is employed in the simulation to predict the speed of UAV, which aids in determining the drag coefficient in each axis. Since measuring of UAV speed is less complicated than measuring of the drag, the drag coefficient can be easily estimated. Based on this approach, the speed of UAV in the vertical direction is estimated. To achieve this, the altitude is represented as a unit step function ranging from 5 to 7 meters. The results of the predicted UAV speed demonstrate a similar trend to that observed in the experiment, and this is shown in Fig. 5.9(a). Furthermore, the longitudinal and lateral speeds are evaluated and validated as shown in Fig. 5.9(b), (c). During this process, the tilting angle of the roll and pitch direction is fixed at 5,°. It means that UAV performs the forward flight mission. Based on the comparison result between the experiment and the present approach, the average discrepancy is smaller than 5%. Consequently, despite the simplification of the proposed fuselage aerodynamics, it improves the degraded correlation with the experiment.
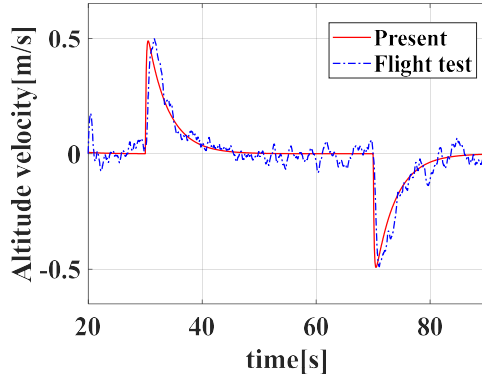
(a) Altitude drag coefficient
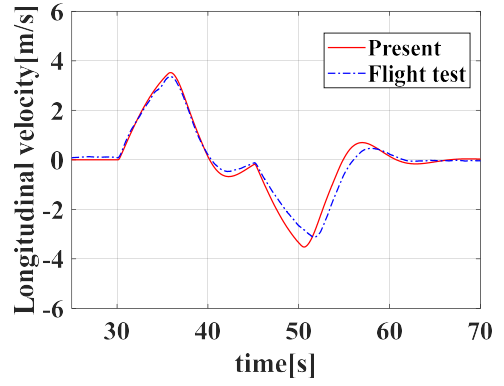
(b) longitudinal drag coefficient
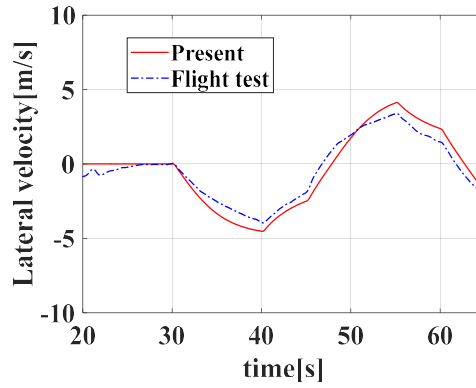
(c) laterall drag coefficientt

Figure 5.9 Results of the drag coefficient

131

5.3 Present simulation results

This section focuses on enhancing the present simulation by integrating the proposed aerodynamics to improve the correlation against the flight test. Prior to comparing with the flight test, a trim analysis will be conducted to acquire the physical constraints and these constraints are applied to the proposed flight simulation. Based on this simulation, the comparison and validation will be performed.

5.3.1 Trim analysis result

To improve the accuracy of the present flight simulation, it is necessary to identify the physical constraints of the target UAV. Due to that, the trim analysis is performed to find the constraints such as the possible rotational speed range and flight speed. In contrast to a conventional rotorcraft, the target UAV is an underdetermined system. Thus, the design variable for the flight dynamics and their upper limit is predetermined. Two flight scenarios, denoted as the climb and forward flight, are used, and the physical meaning of those flight conditions is explained. The following procedure will be carried out to obtain the trim result: 1) Based on Eq. 3.11, the objective function will be minimized. 2) The rotational speed of each rotor and fuselage tilting angle will be selected as the design variables. 3) The physical characteristics of the target UAV will be used to define the lower and upper bound for the design variables. By these steps, a trim analysis is conducted.

During the axial climb, the rotor performance is influenced exclusively by the vertical speed. Due to that, the other variables such as the forward speed and tilting fuselage angle are set to zero. The trim variables of the axial climb are the rotational

speed of each rotor. In addition, those constraints are based on the physical limitation of the rotational speed. Thus, it is necessary to specify the information on the electric motor of the target UAV. The specifications for the UAV and rotor are summarized in Table 5.3. To determine the maximum rotational speed achievable without payload, the motor KV, indicating the rotational speed per voltage, is multiplied by the battery voltage. However, if the payload is taken into account, an additional step is necessary. The approach for accounting for the blade loading effects was presented by Muzar and Lanteigne (Ref. [124]). They suggested a linearized function according to the rotational speed which intersected with the torque curve. Such function had a negative slope. As illustrated in Fig. 5.10(a), two curves intersect at 6,550 rpm. Based on this process, the upper limit for rotational speed is established at 6,550 rpm, and the trim variables are listed in Table 5.4. Figure 5.10(b) shows the trim results, revealing that the rotational speed of the rotor approaches the upper bound as the climb speed is increased. In addition, the climb speed reaches the speed limit of 8.5 m/s. According to the specifications provided by the manufacturer, the maximum climb speed is 5 m/s. The discrepancy between that specification and the present trim result stems from the inclusion of the control margins. Such discrepancy can be explained by the maximum wind resistance speed, which is close to the result obtained by the trim result.

Then, trim analysis for forward flight is performed and the trim variables such as the tilting attitude and rotor speed are selected. The steady forward flight condition is used, which is based on the global frame. To determine the maximum fuselage tilting angle, the specification of the target UAV is applied, which is summarized in

133

Table 5.3. In addition, the relevant trim variables are listed in Table 5.4. The present trim approach is compared against the conventional flight simulation developed by Hartman. He used a simplified aerodynamics for both rotor and fuselage. For the fuselage aerodynamics, Table 5.3 describes the drag coefficients in both the present and Hartman approaches. The comparison between the present and conventional approach is performed and shown in Fig. 5.10(c). By this comparison, a significant discrepancy is observed. The reason for this discrepancy is that the conventional approach neither takes into account the effects of the flight conditions on the rotor performance, nor does it consider the advanced aerodynamics of the fuselage. In Table 5.1, it is stated that the maximum speed achievable during forward flight is 17 m/s when UAV operates under the condition of no wind and no payload. As UAV carries a payload, the maximum forward speed will be smaller than 17 m/s. Such specification indicates that the present trim result estimates a similar trend to the target UAV. As shown in Fig. 5.10(d), a significant discrepancy in the rotational speed is compared and observed. The result obtained by the conventional approach proposes the same magnitude of the rotational speed with respect to the forward flight speed. That approach is not precise and does not accurately depict the actual dynamics of flight. In comparison, the present approach exhibits a similar tendency to that estimated result conducted by Niemic and Gandhi (as referred to in [100]), which incorporated the physical limitations of UAV. By the present trim analysis, the present trim analysis captures the physical constraints of the target UAV. In addition, it is crucial to consider the physical characteristics of UAV for the flight simulation, which improves the accuracy of the prediction.
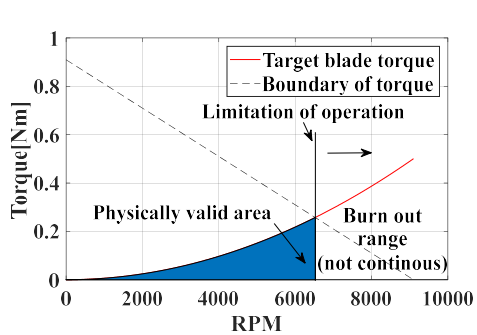
(a) Upper bound of the UAV motor
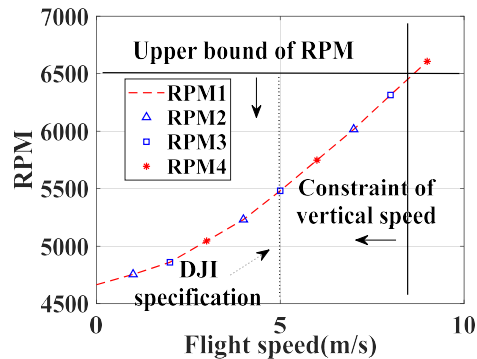
(b) Climb
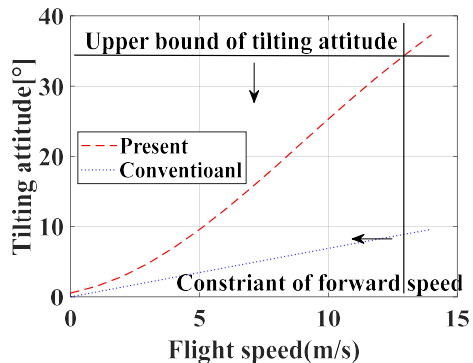
(c) Tilting attitude in terms of the forward speed
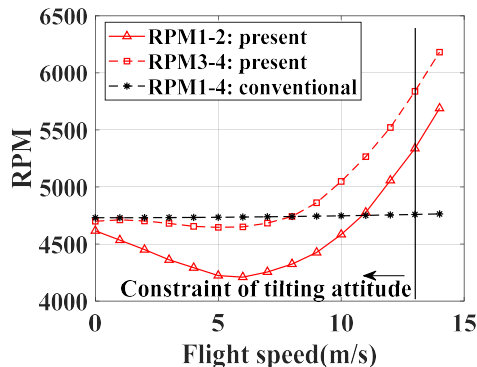
(d) RPM result in terms of the forward speed

Figure 5.10   Trim result for the climb and forward flight

Table 5.3 Trim parameters

DJI MATRICE 100 specification	
Max. anagular speed, °/s	300
Max. tilting attitude(pitch, roll), °	35
Max. climb speed, m/s	5
Max. wind resistance, m/s	10
Max. Forward flight speed(without wind and payload), m/s	17
Motor KV, rpm/V	350
Allowable voltage, V	26
Drag coefficient of the fuselage, conventional	0.38
Drag coefficient of the fuselage, present	0.12

Table 5.4   Trim variables

Trim variables for the climb	Lower bound	Upper bound
Rotor 1, RPM	3,500	6,550
Rotor 2, RPM	3,500	6,550
Rotor 3, RPM	3,500	6,550
Rotor 4, RPM	3,500	6,550
Trim variables for the forward flight	**Lower bound**	**Upper bound**
Forward angle, °	-5	35
Rotor 1, RPM	3,500	6,550
Rotor 2, RPM	3,500	6,550
Rotor 3, RPM	3,500	6,550
Rotor 4, RPM	3,500	6,550

5.3.2 Validation of the present simulation

Based on the previous improvements such as controller estimation, fuselage aerodynamics, and trim analysis, the present simulation is compared and validated against the flight test. As introduced in the previous section, several constraints obtained from the trim analysis are applied. First, the upper bound of the rotational speed is set to consider the physical trend of UAV. In addition, the limit of the fuselage tilting angle is applied to the simulation to be the same as that of the target UAV. To observe the discrepancy between the present flight simulation and conventional approach, quad-simulation, which was suggested by Hartman et al. (Ref. [92]) is used in this dissertation. The trend-based aerodynamics for the fuselage is applied to the conventional approach. Except for the aerodynamics for the rotor and fuselage, the other conditions implemented in the simulation are consistent for both conventional and the present flight simulation.

To validate the present flight simulation, a two-point flight test is performed and the concept of such a test is illustrated in Fig. 5.11. The criteria such as the mean absolute error (MAE), mean square error (MSE), and root mean square error (RMSE) is applied to evaluate the precision of both present and conventional simulations. The experiment is conducted outdoors. Furthermore, the fuselage tilting angle for forward flight is limited as $5\,^\circ$. Based on these, the results of the tilting attitudes and trajectories are compared. As demonstrated in Fig. 5.12(a) and (c), neither the present nor conventional simulations accurately predict the rolling and yawing tendencies observed in the experiment. Although both the experiment and simulations use the same command input, the discrepancy is generated by the external wind

which is not considered in the flight simulation. Figure 5.12 (b) shows the results for the pitching angle. Table 5.5 indicates that the present simulation exhibits enhanced precision, with a 20% improvement for MAE, a 56% increase for MSE, and a 34% increase for RMSE. As the longitudinal and lateral trajectories are significantly affected by the rolling and pitching angle of the fuselage, similar results are presented and found in Fig. 5.12 (d)-(e). The measured result of the altitude has uncertainty due to the precision of the global positioning system (GPS). That reason degrades the accuracy of the altitude. The relevant result for the altitude dynamics is illustrated in Fig. 5.12 (f), and both present and conventional simulations are compared. Both simulations do not capture the correct trend of the altitude. Table 5.5 compares six dynamic behaviors such as X, Y, Z, ϕ, θ, and ψ. Those comparisons reveal that the present flight simulation approach exhibits an enhanced correlation with the experiment when compared to the conventional flight simulation, except for the altitude. Specifically, the prediction accuracy for the longitudinal trajectory and pitching angles are improved as 25% for MAE, 65% for MSE, and 41% for RMSE. Although the results obtained by the present simulation overestimate the measured data of the flight test, it shows improved prediction results compared against the conventional simulation.

The results obtained by the conventional and present simulation do not consider the external wind condition. Due to that, it may induce a discrepancy between simulations and the experiment. However, it is not straightforward to measure the external wind condition without a sensor. Therefore, arbitrary wind profiles are chosen in the following manner. First, the inconsistency in the trajectory between the

experiment and simulation is investigated by utilizing an attitude input obtained from the flight test. Subsequently, arbitrary wind profiles in both lateral and longitudinal directions are generated. The wind profile that exhibits the most similar trend to the experiment is chosen and implemented in both the present and conventional simulations, as illustrated in Fig. 5.13. The results applied to the wind profiles show better accuracy than results without the wind profile. Figure 5.14 (a) and (b) show good agreements with the flight test for the result of the rolling and pitching attitudes. Since the wind profile for vertical direction is not considered, results predicted by both simulations for the altitude exhibit a similar trend when UAV performs forward flight. The relevant result is illustrated in Fig. 5.14 (f). The consideration of the wind profile improves the accuracy of the present simulation more than that of the conventional simulation as 63% for MAE, 83% for MSE, and 58% for RMSE. The detailed comparisons are listed in Table 5.6. Consequently, the present flight simulation demonstrates an improved accuracy over the conventional flight simulation. Furthermore, it is capable of predicting the dynamic behavior of a multirotor UAV. However, the approach using arbitrary wind profiles has still room to be arranged systematically. For that, the relevant approach is proposed in Section 3.2.2. The detailed verification and implementation will be described in the next section.
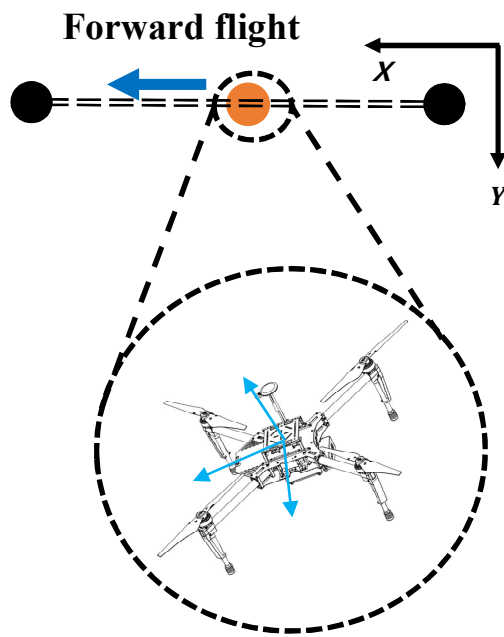
Figure 5.11 Concept of the two point flight test

(a) Rolling

(b) Pitching

(c) Yawing

(d) Lateral

(e) Longitudinal

(f) Altitude
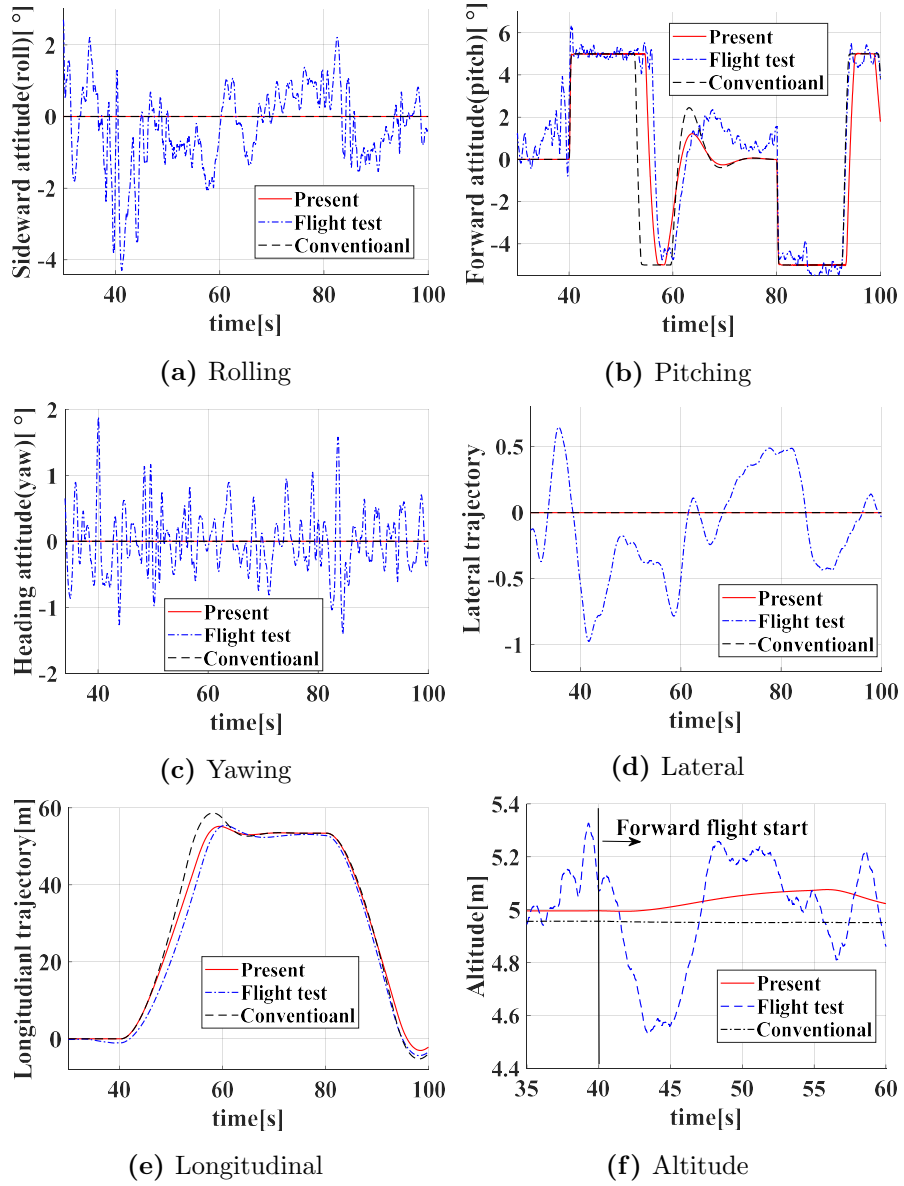
Figure 5.12   Comparison of the present simulation against the experiment(without wind)
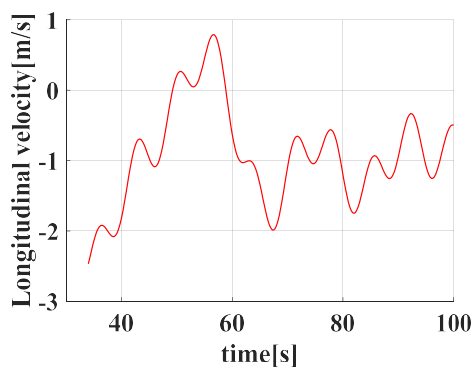
(a) Longitudinal direction wind speed
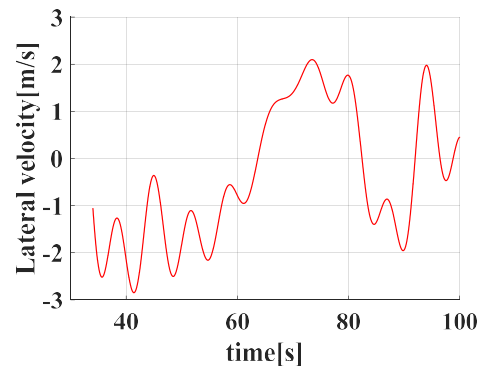
(b) Lateral direction wind speed

Figure 5.13   Wind speed profile

(a) Rolling

(b) Pitching

(c) Yawing

(d) Lateral

(e) Longitudinal

(f) Altitude
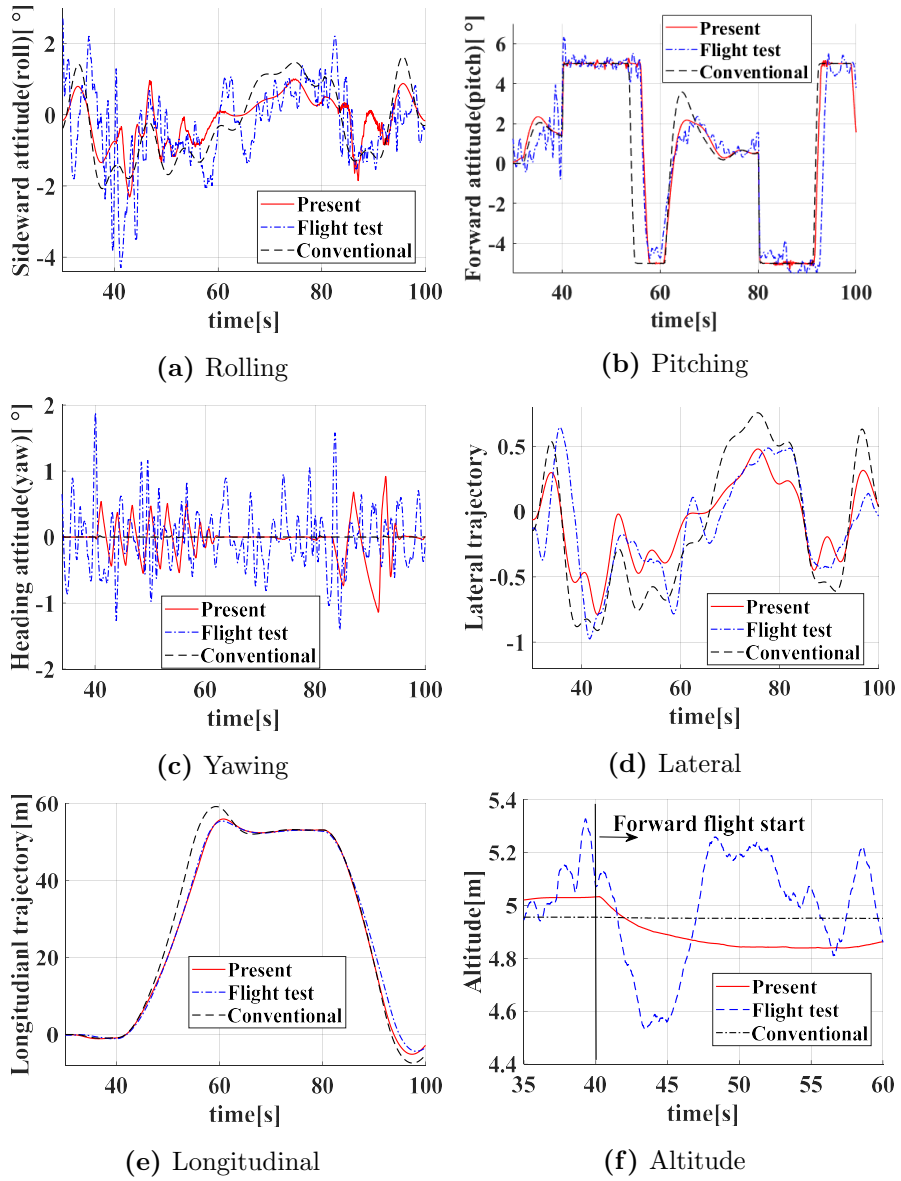
Figure 5.14 Comparison of the present simulation against the experiment(with wind)

144

Table 5.5 Comparision between the present and conventional simulaiton(without wind)

	Present	Conventional	Enhancement, %
Roll-MAE, °	0.8502	0.8502	0.0
Roll-MSE, °	1.2562	1.2562	0.0
Roll-RMSE, °	1.1208	1.1208	0.0
Pitch-MAE, °	0.9464	1.1954	20.8340
Pitch-MSE, °	2.1601	4.9973	56.7735
Pitch-RMSE, °	1.4697	2.2355	34.2531
Yaw-MAE, °	0.3518	0.3518	0.0
Yaw-MSE, °	0.2096	0.2096	0.0
Yaw-RMSE, °	0.4578	0.4578	0.0
Lateral-MAE, m	0.3187	0.3187	0.0
Lateral-MSE, m	0.1508	0.1508	0.0
Lateral-RMSE, m	0.3883	0.3883	0.0
Longitudinal-MAE, m	1.7667	2.3802	25.7745
Longitudinal-MSE, m	5.9402	17.0779	65.2169
Longitudinal-RMSE, m	2.4373	4.1325	41.0228
Altitude-MAE, m	0.1416	0.1458	2.8321
Altitude-MSE, m	0.0340	0.0324	-5.0534
Altitude-RMSE, m	0.1845	0.1800	-2.4956

Table 5.6 Comparision between the present and conventional simulaiton(with wind)

	Present	Conventional without wind profile	Conventional with wind profile	Enhancement, % without wind profile	Enhancement, % with wind profile
Roll-MAE, °	0.6974	0.8502	0.7781	17.9722	10.3714
Roll-MSE, °	0.9157	1.2562	1.0212	27.1056	10.3310
Roll-RMSE, °	0.9569	1.1208	1.0105	14.6235	5.3043
Pitch-MAE, °	0.6815	1.1954	1.0792	42.9898	36.8514
Pitch-MSE, °	1.5054	4.9973	4.8275	69.8757	68.8162
Pitch-RMSE, °	1.2270	2.2355	2.1972	45.1130	44.1562
Yaw-MAE, °	0.4169	0.3518	0.3516	-18.5048	-18.5722
Yaw-MSE, °	0.2929	0.2096	0.2100	-39.7424	-39.4762
Yaw-RMSE, °	0.5412	0.4578	0.4582	-18.2176	-18.1144
Lateral-MAE, m	0.1708	0.3187	0.2431	46.4073	29.7408
Lateral-MSE, m	0.0556	0.1508	0.1018	63.1300	45.3831
Lateral-RMSE, m	0.2359	0.3883	0.3190	39.2480	26.0502
Longitudinal-MAE, m	0.7337	2.3802	2.0100	69.1749	63.4975
Longitudinal-MSE, m	1.7270	17.0779	10.2112	89.8875	83.0872
Longitudinal-RMSE, m	1.3141	4.1325	3.1955	68.2008	58.8765
Altitude-MAE, m	0.1387	0.1458	0.1460	4.8697	5.0000
Altitude-MSE, m	0.0333	0.0324	0.0324	-2.7778	-2.7778
Altitude-RMSE, m	0.1823	0.1800	0.1801	-1.2778	-1.2215

5.4 Validation of the gust experiment

In the previous section, the present flight simulation is verified by the flight test. However, the improvements such as the gust estimation and gust experiments are needed to predict the transient behavior of UAV in urban. This section aims to investigate and evaluate the transient behavior of UAV influenced by the gust. First, the validation of the proposed estimation approach is performed. Then, the comparison between the present flight simulation and the experiment with gust is performed.

5.4.1 Description of the gust experiment

The feature of gust flown in urban areas differs from that in rural areas due to the presence of buildings, which creates a complex gust pattern (Ref. [67]). Urban canyons and other geometric structures have a significant influence on gust speed, which can affect the stability of a UAV. Furthermore, experiments for the gust are rare and only a few investigations to identify the dynamic behavior of UAV based on a prescribed gust with low strength were performed. Therefore, it is important to predict the behavior of UAV due to the gust for safe operation in urban.

The gust experiments are conducted at Goheung Aviation Center of the Korea Aerospace Research Institute (KARI). The wind tunnel facility is used as described in Ref. [77]. The experiment is performed outdoors due to two primary reasons. First, for gust experiments involving the shear stream, sufficient space surrounding the experiment is required. NASA conducted free-flight tests for forward and descent flight in a closed wind tunnel as described in Ref. [63]. However, closed wind tunnels

are not suitable for unsteady gust experiments. Secondly, it is important to consider practical flight conditions as closely as possible during flight tests. In contrast to the indoor wind tunnel tests, the surrounding atmosphere during UAV flight includes an arbitrary amount of gusts, which may affect the transient behavior of UAV. Therefore, the gust experiment is conducted outdoors.

To conduct the gust experiment, a straight flight trajectory is chosen that runs parallel to the wind tunnel passage. The UAV is positioned within the internal region of the yellow line segment, where the gust is uniformly created by the wind tunnel. The detailed information is presented in Fig. 5.15. The flight trajectory includes three parts: the starting location (Section A), the gust occurrence region (Section B), and the finish location (Section C). The UAV waits for a certain period at the starting location before it enters the wind tunnel region. After a certain period, UAV passes Section B and reaches the finish location. The UAV then returns to the starting location and the total flight time is 250 seconds. During the experiment, the maximum vehicle tilting angle for forward direction is limited to 5 ° to prevent the vehicle from traversing the wind tunnel passage too quickly. The four gust strengths such as 3, 6, 9, and 12 m/s are applied to investigate the transient behavior of UAV. Table 5.7 provides more information for the experimental conditions.
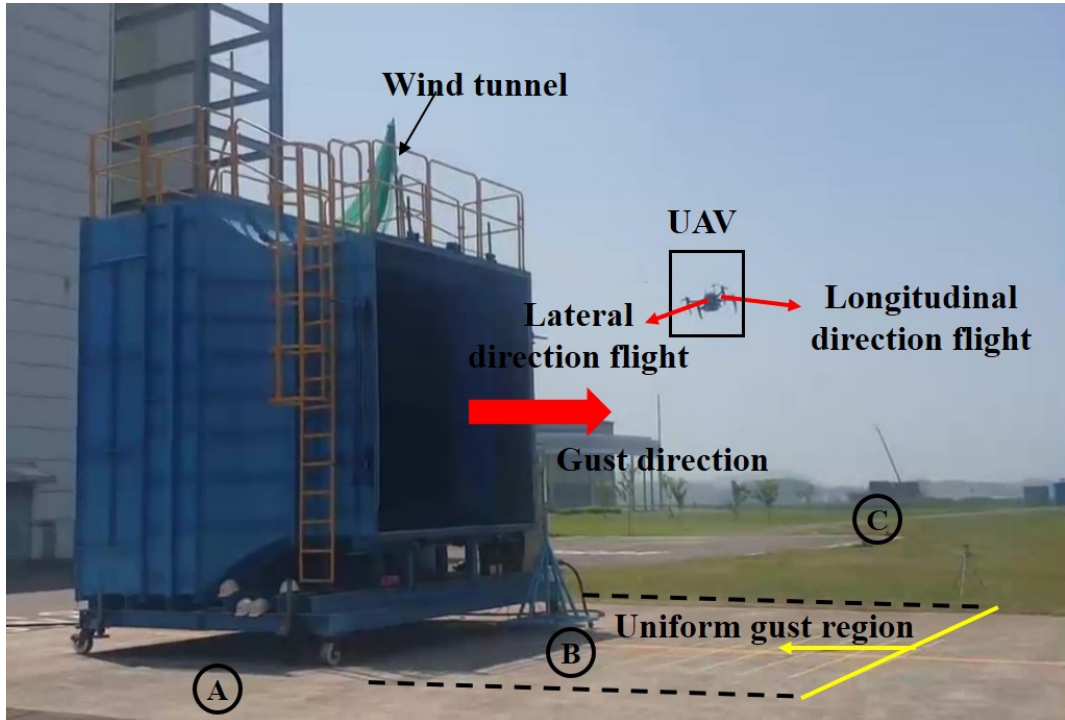
Figure 5.15 Facility for the gust experiment

Table 5.7 Specifications of the gust experiment

Experiment setting	value[unit]
Max. longitudinal vehicle tilting angle	5 [°]
Max. lateral vehicle tilting angle	30 [°]
Total flight elapsed duration	250 [s]
Prescribed gust strength	3, 6, 9, 12 [m/s]
Starting location (A)	(0,0) [m]
Gust impact range (B)	3.5 [m]
Finish location	(20,0) [m]
Flight trajectory	A→B→C→B→A

5.4.2 Validation of the proposed gust estimation

Gust estimation based on the simulation

Prior to comparing the proposed simulation with the gust experiment, it is necessary to confirm the proposed gust estimation approach. For that, it is crucial to determine the gust profile accurately. As a result, Dryden and shear gust formulation (Ref. [65]) is utilized for validation. These formulations are commonly applied to evaluate the influence of the gust which is affected aircraft. The shear formulation is utilized to determine the magnitude of the gust, which is expressed in terms of height above the ground and represented as a specific value. Generally, the gust is characterized by turbulence, which has a stochastic feature. To account for this, Dryden formulation is applied. This formulation is defined in MIL-F-8785C (Ref. [65]), as well as in MIL-HDBK-1797/1797B (Refs. [125]-[126]). MIL-F-8785C presents two turbulence approaches: Dryden and Von Karman. If a comparable structural analysis is being carried out, it should apply von Karman approach. As comparable structural analysis is not required, Dryden approach is suitable. Thus, this dissertation uses Dryden approach because of the rigid structural characteristics of a multirotor UAV. As stated in Section 3.2.2, the present approach estimates both longitudinal and lateral directions separately. The relevant formulation is presented in Eq. 5.3. g_{shear} and g_{dryden} denotes the strength of the shear and Dryden, respectively. The details of such formulation are described in Refs. [65], [126].

$$g_{total} = g_{shear} + g_{dryden} \tag{5.3}$$

Using these formulations, gust estimation is conducted for both hover and forward flight. Figure 5.16 exhibits a comparison of the results obtained for hovering, where both longitudinal and lateral gust profiles are evaluated and validated. These results show consistency. Next, the validation process for forward flight is carried out, with further details as follows. First, UAV performs the forward flight after 30 seconds, and it moves a straight-line flight trajectory. The comparison result of the forward flight is shown in Fig. 5.17, and shows good agreement with the gust profile based on Eq. 5.3. Figure 5.17 (a) shows that the proposed gust estimation captures the high-frequency perturbation characteristics of the longitudinal gust profile. However, in Figure 5.17 (b), these characteristics are less captured when compared to the result obtained for the longitudinal direction. There is the following reason for such discrepancy. As summarized in Table 5.2, the types of controllers for the longitudinal and lateral positions are different. To reinforce the gust resistance, I-PD control law is used in the lateral position. Since an I-type controller reduces the system response, the capability to capture the higher frequency perturbation of the gust is degraded than the longitudinal position controller. To further investigate such degradation, an analysis using fast Fourier transform (FFT) is conducted to determine the maximum frequency of the gust that can be captured by the proposed method, which is found to be accurate up to a maximum frequency of 0.5 Hz. Despite this limitation, the gust trend observed using the proposed approach shows good agreement with that obtained using Dryden and shear gust formulations. Moreover, it is worth noting that in real-world condition, the frequency of gusts is generally lower than 0.5 Hz (Ref. [127]). Therefore, it is concluded that the proposed estimation approach can accurately estimate the gust profile.
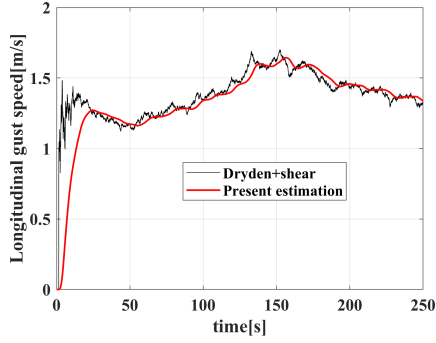
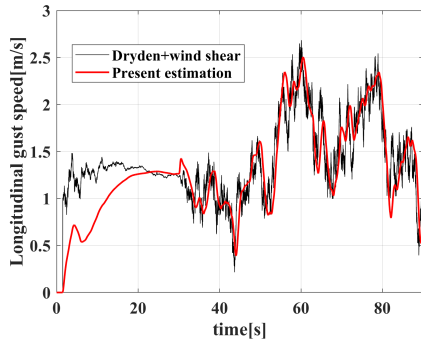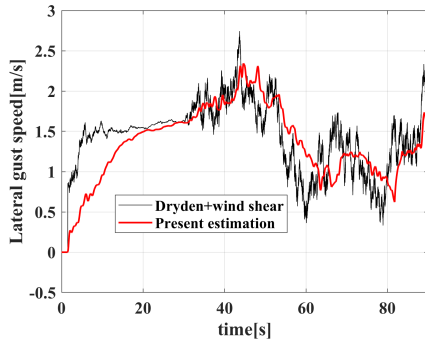**(a)** Longitudinal gust profile
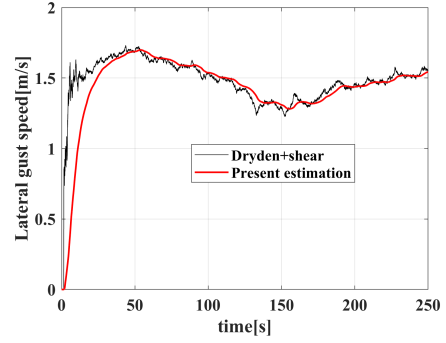
(b) Lateral gust profile

Figure 5.16   Results of the gust estimation in hover

(a) Longitudinal gust profile

(b) Lateral gust profile

Figure 5.17   Results of the gust estimation in forward flight

Gust estimation based on the flight test

In the previous section, the proposed gust estimation approach is validated. Using this approach, the estimation of the gust profile of the flight test is performed. The trajectory of the flight is divided into three sections, denoted as A, B, and C, as shown in Fig. 5.15. However, as the gust in Section B is uniform and is prescribed by the wind tunnel, the gust which exists in Sections A and C is estimated by the proposed approach. The result is exhibited in Fig. 5.18 for both the longitudinal and lateral directions.

However, since there is no direct measurement of gust during the experiment, the proposed estimation approach can not be fully validated. Instead, the average gust measurement obtained during KARI met-mast (Ref. [128]) is applied to the verification procedure. KARI met-mast recorded the strength of the gust for two years at Goheung Aviation Center and captured the trend of the average gust in terms of months. The present gust experiment in this dissertation is conducted at 11:00 on June 4, 2019. According to the measurement result, the average gust for the flight test is approximately 2.7 m/s. Fig. 5.18 demonstrates that the proposed estimation approach predicts an average gust strength of 2.62 m/s, which has a 3% discrepancy compared to the expected value of 2.7 m/s based on the measurement result. Table 5.8 presents the comparison between the predicted and measured gust strength. By this comparison, the proposed approach is capable of predicting the gust under outdoor conditions with reasonable accuracy. Furthermore, since there is a prevailing wind at the Goheung Aviation Center, the proposed approach can also

capture and predict both the gust and prevailing wind effects. The obtained gust profile is then used for the flight simulation.
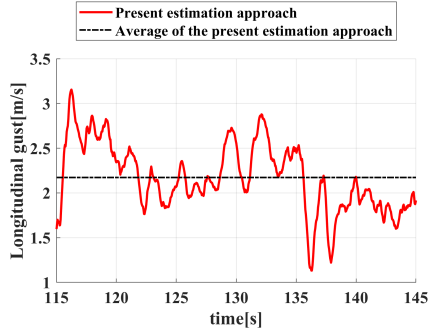
(a) Longitudinal gust profile at Section A
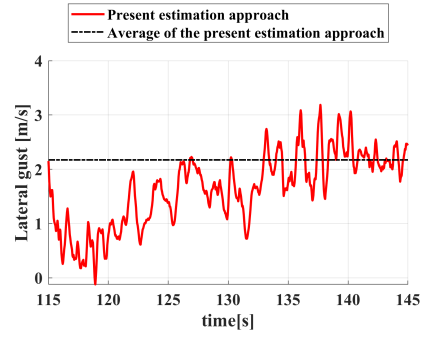
(b) Lateral gust profile at Section A
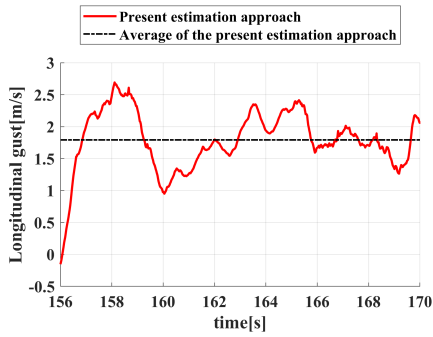
(c) Longitudinal gust profile at Section C
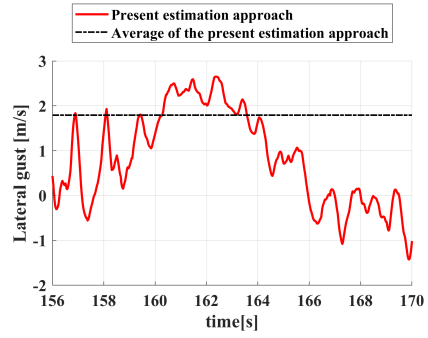
(d) Lateral gust profile at Section C

Figure 5.18 Results of the gust estimation based on the flight test

Table 5.8 Comparison of the average value of the gust result

	Proposed result	Measurement obtained by KARI met-test	Discrepancy, %
Average gust strength, m/s	2.62	2.7	3

5.4.3 Comparison between the proposed simulation and flight test

In this section, three sets of results are obtained and compared: the flight test, a flight simulation under ideal conditions with only the prescribed gust at Section B, and a flight simulation that incorporates the gust predicted by the proposed estimation method. Table 5.10 summarizes the details. In Fig. 5.19, the results of the longitudinal direction flight are compared. Figures 5.19 (a), (b), and (c) show that the simulation results for an ideal condition, which only includes the gust prescribed by the wind tunnel, have a certain amount of discrepancy compared to the flight test. On the other hand, the proposed simulation results show good agreement with the flight test. At a speed of 6 m/s, the discrepancy between the simulation with an ideal condition and the gust experiment is increased more than that of the result obtained at 3 m/s. However, when including the gust profile, the discrepancy is decreased, as shown in Figs. 5.19 (d), (e), and (f). Based on these results, the proposed simulation with a gust profile is capable of capturing the accurate transient behavior of UAV.

The comparison results for the lateral direction flight are presented in Figure 5.20. It is observed that the correlation for an ideal condition is generally poor and worsens with an increase in gust speed. In particular, a significant amount of discrepancy is exhibited in the result of the fuselage tilting angle and flight speed in the lateral direction. Such discrepancy is increased with higher gust strength as indicated by the arrows in Figure 5.20(k). In contrast to the ideal condition, the proposed flight simulation with the gust profile shows good agreement with the flight test. The result of tilting attitude and flight speed obtained by this simulation maintains accuracy regardless of gust strength. However, the result of the lateral trajectory exhibits

significant discrepancies between the proposed simulation and the gust experiment. This is the reason that the order of magnitude of the lateral trajectory is smaller than the GPS precision for maintaining the hovering location. Such precision of GPS is 2.5 m provided by the manufacturer. It means that the measurements of the trajectory may have uncertainties during hovering. Due to that, the prediction result at Sections A and C may be degraded because the corresponding flight condition at those sections is hovering. Therefore, an additional investigation and comparison are performed at Section B. The lateral location of the UAV in the wind tunnel is determined from the gust experiment. This location is used as a reference for both an ideal condition and a flight simulation that takes into account the gust. The comparison of these results is shown in Fig 5.21 and shows a good correlation.

To assess the accuracy of the proposed flight simulation, the goodness of fit is applied. This approach is a numerical value representing the similarity between the predicted results and the gust experiment. Furthermore, the cost function to be implemented for the goodness of fit is set to the normalized root mean square error (NRMSE). The value obtained by the goodness of fit has the range from negative infinity to positive unity. The positive unity means that the discrepancy between the predicted results and the flight test is zero. Figure 5.22 shows a comparison between the goodness of fit for longitudinal and lateral flight directions. As the prescribed gust increases, the goodness of fit for an ideal condition decreases. The flight simulation including the gust profile leads to an improved result, indicating that the proposed prediction is relatively consistent with the gust experiment. The goodness of fits for both longitudinal and lateral directions flight are 0.97 and 0.82 respectively.

159

Although the precision accuracy for lateral direction is less than the longitudinal result, the proposed simulation is capable of capturing the lateral behavior of the UAV sufficiently. Consequently, the proposed flight simulation can predict the transient behavior of UAV with high gust strength.

Table 5.9 Comparison of the average value of the gust result

	Section A and C	Section B
Ideal condition	no external gust	prescribed gust created by the wind tunnel (uniform gust)
including the gust profile	gust profile estimated by proposed approach	Same as above

(a) Trajectory at 3 m/s gust situation

(b) Vehicle tilting angle at 3 m/s gust situation

(c) Flight speed at 3 m/s gust situation

(d) Trajectory at 6 m/s gust situation

(e) Vehicle tilting angle at 6 m/s gust situation

(f) Flight speed at 6 m/s gust situation

(g) Trajectory at 9 m/s gust situation

(h) Vehicle tilting angle at 9 m/s gust situation

(i) Flight speed at 9 m/s gust situation

(j) Trajectory at 12 m/s gust situation

(k) Vehicle tilting angle at 12 m/s gust situation

(l) Flight speed at 12 m/s gust situation

Figure 5.19   Comparison between the proposed simulation and flight test: longitudinal direction flight

162

(a) Trajectory at 3 m/s gust situation

(b) Vehicle tilting angle at 3 m/s gust situation

(c) Flight speed at 3 m/s gust situation

(d) Trajectory at 6 m/s gust situation

(e) Vehicle tilting angle at 6 m/s gust situation

(f) Flight speed at 6 m/s gust situation

(g) Trajectory at 9 m/s gust situation

(h) Vehicle tilting angle at 9 m/s gust situation

(i) Flight speed at 9 m/s gust situation

(j) Trajectory at 12 m/s gust situation

(k) Vehicle tilting angle at 12 m/s gust situation

(l) Flight speed at 12 m/s gust situation

Figure 5.20 Comparison between the proposed simulation and flight test: lateral direction flight

163
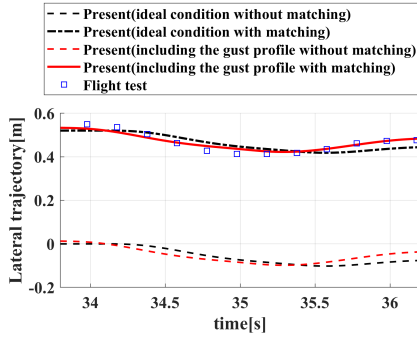
(a) Trajectory at 3 m/s gust situation
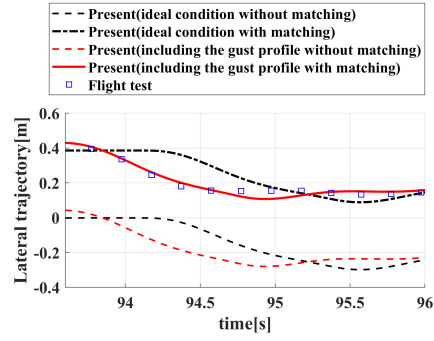
(b) Trajectory at 6 m/s gust situation
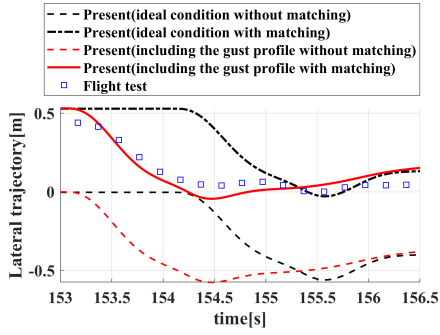
(c) Trajectory at 9 m/s gust situation
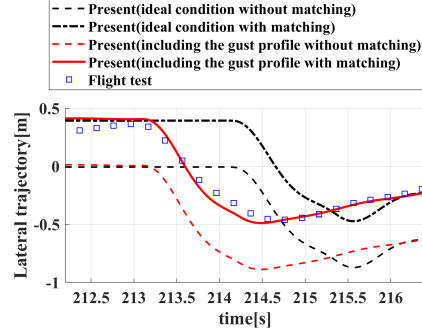
(d) Trajectory at 12 m/s gust situation

Figure 5.21   Comparison between the simulation and flight test: lateral trajectory matching the entrance position

(a) Goodness of fit result for the longitudinal direction flight

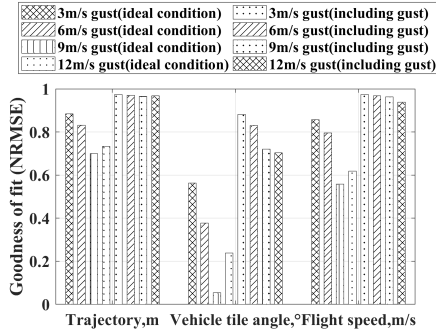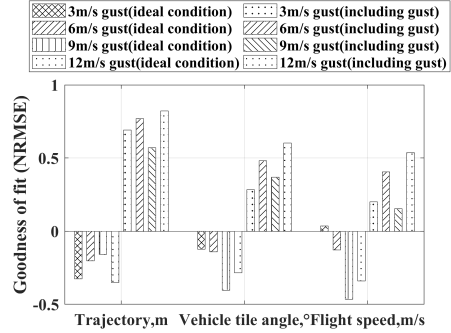**(b)** Goodness of fit result for the lateral direction flight

Figure 5.22   Results for the goodness of fit: longitudinal and lateral flight

5.5 Further investigation of the present flight simulation

Based on the previous sections, the proposed flight simulation is validated by the flight test and gust experiment. In this section, the effect induced by rigid blade flapping and aerodynamic interference among the rotors is investigated and evaluated. Then, the high-intensity gust condition is applied to investigate the transient behavior of a multirotor UAV

5.5.1 Effect of the rigid blade flapping and aerodynamic interference among the rotors

This dissertation develops and applies the proposed rotor aerodynamic analysis to predict the transient behavior of UAV accurately. Such rotor analysis shows that the rigid blade flapping and interference significantly affect the aerodynamic characteristics of UAV rotor. Thus, it is necessary to identify the effect of the rigid blade flapping and aerodynamic interference which affect the flight dynamics and performance of UAV. The analysis consists of the following two steps. First, the effect of the rigid blade flapping is evaluated. A two-point flight condition is applied. The range between the two points is 3 km, and the three fuselage tilting angles such as $5\,^\circ$, $15\,^\circ$, and $25\,^\circ$ are used to constraint the forward speed of UAV. Then, the investigation of the interference effect is performed. The operating condition to compare the effect with and without the interference is the same which is selected in the rigid blade flapping investigation analysis. Fig. 5.23 exhibits the findings from the rigid blade flapping analysis. As shown in Fig. 5.23(a), the results of the pitching angle with and without the flapping propose a similar trend. Figures 5.23(b) and (c)

demonstrate that discrepancies in the longitudinal speed and trajectory exist. When considering the flapping, the longitudinal trajectories are found to be lower than the result without the flapping. The discrepancies are related to the longitudinal speed and are decreased when the flight speed is increased. The findings demonstrate that the effect of the rigid blade flapping reduces as the flight speed is increased. This is due to the fact that the rotor drag is reduced as the fuselage tilting angle is increased. The relevant investigation is illustrated in Fig. 4.7. In addition, the fuselage drag becomes a predominant factor during high forward flight, and the performance of UAV is more reliant on the aerodynamics of the fuselage. The altitude of UAV is affected by the fuselage tilting angle and such a result is illustrated in Fig. 5.23 (d). These results show that the altitude of UAV is less affected by the rigid blade flapping. Furthermore, the decrease rate of the altitude is large when the rigid flapping is not considered. As the predicted result of the longitudinal speed without the flapping is larger than the result with the flapping, the amount of the inflow that is perpendicular to the tip path plane is increased. Due to that, the thrust of UAV rotor is decreased and it brings a further decreased altitude result.

Then, the effect of the aerodynamic interference is investigated. In Figs. 5.24 (a)–(d), the results for the fuselage tilting angle, longitudinal trajectory, longitudinal speed, and altitude are compared and show a similar tendency in either both results with and without the interference effect. The comparison result of the fuselage tilting angle shows the same transient behavior. In contrast to the investigation for the rigid blade flapping, the longitudinal trajectory and speed exhibit an identical tendency regardless of the aerodynamic interference. Although the discrepancy is observed

from the result of the altitude, it is not significant and becomes decreased when the fuselage tilting angle is increased. Specifically, the behavior of the altitude shows the same tendency at 25 ° fuselage tilting angle, which is illustrated in Fig. 5.24 (d). This is the reason why the aerodynamic interference among the rotor is decreased when the fuselage tilting angle is increased. The relevant result is exhibited in Fig. 4.20. In contrast to these results, the estimation of the rotational speed of both front and rear rotors has a significant discrepancy, as shown in Fig. 5.25. The front rotor rotational speed with the interference is smaller than the that of the front rotor without the interference. In addition, the result of the rear rotor shows an opposite tendency of this comparison. As described in Section 4, the rear rotor is affected by the wake of the front rotor. As this wake induces additional inflow of the rear rotor, the aerodynamic load such as thrust will be decreased. Thus, the rotational speed of the rear rotor is increased to maintain the fuselage tilting angle.

Based on these investigations, two findings are obtained. First, the rigid blade flapping is related to the dynamic characteristics such as flight speed. The aerodynamic load such as drag is significantly affected by the rigid blade flapping described in Chpater 4. As it influences the total drag of UAV, discrepancy is observed whether or not the flapping of the blade. Due to that, it is necessary to consider the rigid blade flapping for improving the accuracy of the flight simulation. Second, it is found that the consideration of the aerodynamic interference does not have a significant influence on the flight dynamics and performance of the target UAV when UAV performs forward flight. This finding indicates that it is permitted to omit the aerodynamic interference effect to predict the dynamic response of a quad-rotor

167

UAV. Since a quad-rotor UAV needs a fuselage tilting angle to perform the forward flight, such effect is less considerable than the other multirotor UAV configurations. However, the rotational speed of the rotor still shows the discrepancy between with and without the interference. Thus, to obtain an accurate result of a quadrotor UAV, consideration of the aerodynamic interference will be indispensable.
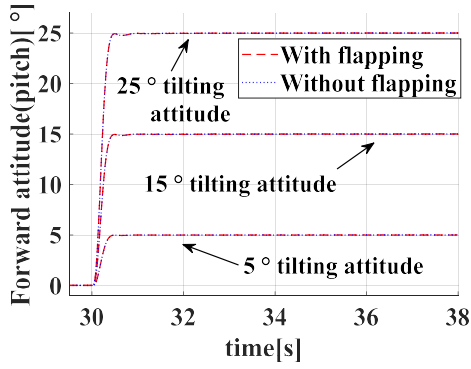
(a) Pitching
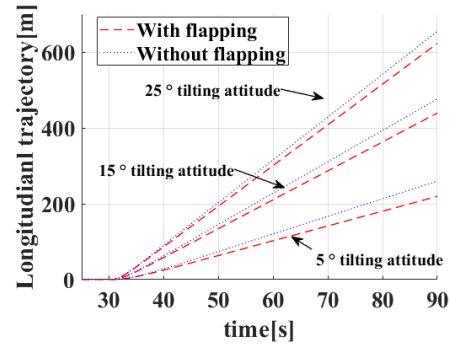
(b) Longitudinal trajectory
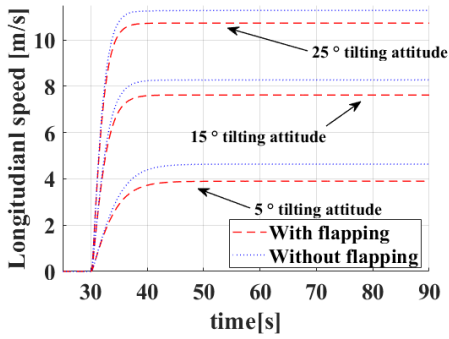
(c) Longitudinal speed

(d) Altitdue

Figure 5.23 Effect of the rigid blade flapping
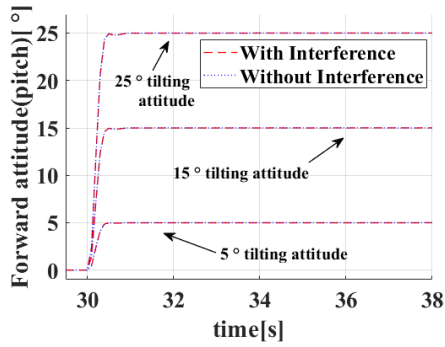
(a) Pitching
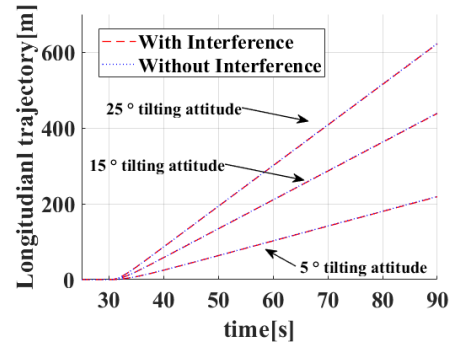
(b) Longitudinal trajectory
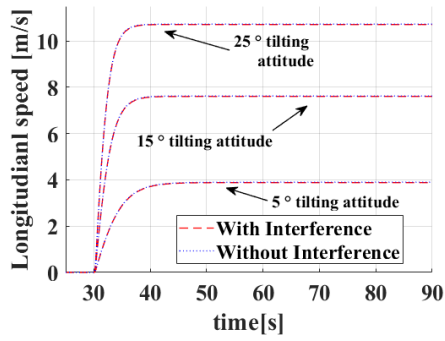
(c) Longitudinal speed
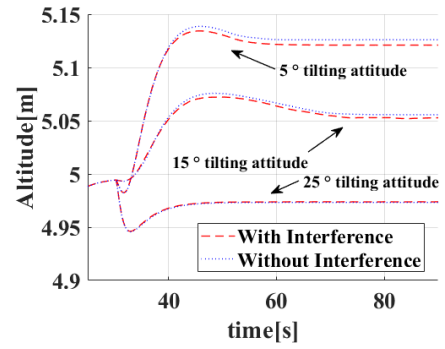
(d) Altitdue

Figure 5.24   Effect of the aerodynamic interference
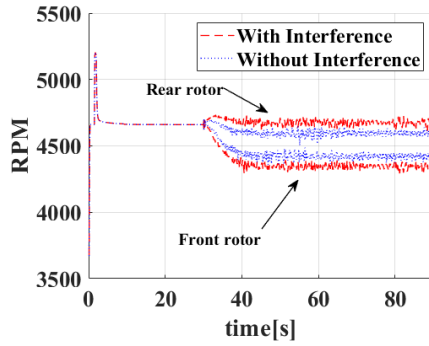
(a) Fuselage tilting angle: 5 °
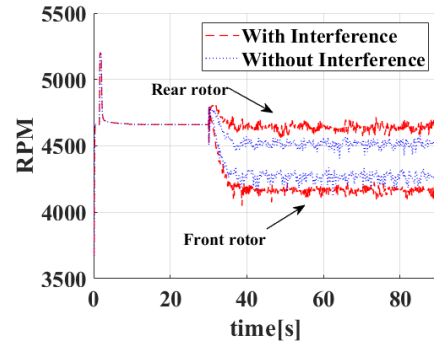
(b) Fuselage tilting angle: 15 °
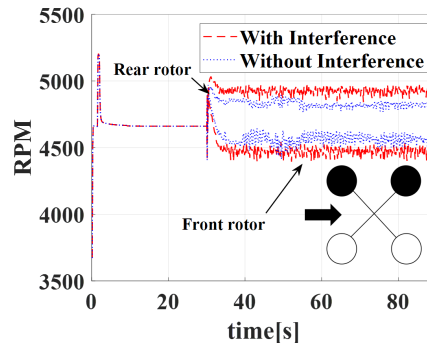
(c) Fuselage tilting angle: 25 °

Figure 5.25   Comparison between the rotational speed of the front and rear
rotors including whether interference or not

171

5.5.2 Investigation of the transient behavior due to gust while increased intensity

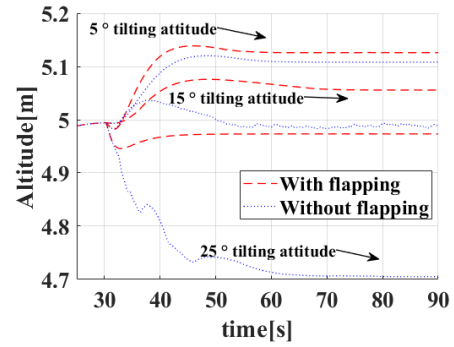The comparison described in Section 5.4 indicates that the proposed flight simulation can capture the transient behavior of a multi-rotor UAV affected by the gust. Although the verification procedure for the present flight simulation is performed, it is necessary to investigate the gust condition that occurs in an urban region. In an urban region, unique features such as an urban canyon induce the venturi effect. Sprin (Ref. [129]) found that the average height, length of the building, and the width between buildings affect the strength of the venturi effect. When the distance between buildings is less than 3m, the venturi effect is combined with the channelization effect. Due to that effect, the flow direction of the gust is parallel to the buildings. Furthermore, it results in a considerable increase in the speed of the stream. Fig. 5.26 illustrates these effects, which are frequently observed in urban and metropolitan regions. Consequently, when UAV traverses those areas, it may encounter high-intensity of gust, as shown in Fig. 5.26.

Therefore, this section investigates the transient behavior of a multi-rotor UAV under high-intensity gust conditions. The analysis considers both the distance between buildings and the intensity of gusts, which are described as follows. When the gust passes through the urban canyon, the strength of the gust is at least 8 m/s (Ref. [5]). Based on that, the gust strength used in this investigation is the four cases as 9, 12, 15, and 18 m/s. The width of the urban canyon is selected as another parameter, which should be greater than half of the typical building height according to Ref. [129]. The previous studies (Refs. [130], [131], [132]) investigated and suggested the

average building heights ranging from 15 to 30 m in urban areas. Using those studies, an average building height is selected to be 20m and the width of the urban canyon is determined. These details are listed in Table 5.10. As shown in Fig. 5.26, the mission profile is illustrated, which passes through the venturi effect zone.

Table 5.10 describes the situations which are used in this investigation. The gust strength and distance are abbreviated as G and D respectively. Figure 5.27 shows the comparison results of the lateral trajectory, lateral speed, and altitude, which are focused on the effect of the distance between the buildings. These results only exhibit the dynamic behavior of UAV with certain gust intensities as 9 and 18 m/s. The lateral trajectory shows the increasing trend when distance is increased. Specifically, the result with an 18 m/s gust situation proposes the fuselage tilting angle is reached to the maximum tilting angle. As shown in Fig. 5.27 (e), the relevant description is presented. There is a significant discrepancy in the magnitude of lateral trajectories predicted between the results. Furthermore, the trend for altitude varies depending on the gust strength, with an increase in altitude for 9 m/s gusts and a decrease for 18 m/s gusts. The details of these trends are illustrated in Figs. 5.28 (c) and (f). To compare these discrepancies for lateral trajectory and altitude quantitatively, the maximum intensity situation such as G4-D4 is used to normalize the other situations. The comparison of these normalized discrepancies is presented in Fig. 5.29. The results suggest that the discrepancies in lateral trajectory and altitude are influenced by the distance between buildings and the increase in gust intensity.

Based on these results, the rotor aerodynamics proposed in this dissertation is significant in predicting the transient behavior of UAV due to gusts with high

intensity. Further, it indicates that the rotor aerodynamics based on the simplified equation may be not appropriate to predict the nonlinear dynamic behavior of UAV influenced by the gust. To identify that, the thrust comparison for both the present analysis and the simplified equation is performed. G4-D4 listed in Table 5.10 is used for this comparison. The coefficient of the simplified formulation is based on the result of hover as shown in Fig. 5.4. The relevant result is exhibited in Fig. 5.30. The result shows that the thrust discrepancy is not significant when UAV does not pass through the gust region. However, the discrepancy becomes 23% when UAV enters the gust region. In addition, the result of lateral trajectory and altitude are compared in Fig. 5.31. These results show significant discrepancies which are 44% and 10%, respectively. These investigations indicate that the simplified equation becomes inaccurate as the gust strength increases. Furthermore, the dynamic behavior of UAV has significant discrepancies compared with the present rotor aerodynamics. As a result, it can be concluded that the simplified equation is unsuitable to predict the behavior of UAV due to a larger intensity gust. Based on these investigations, it is crucial to use the present rotor aerodynamics for capturing the transient behavior of a multi-rotor UAV affected by a larger intensity gust. In addition, it is important to predict such dynamic behavior of a multirotor UAV in real time. Using two approaches such as Euler and Runge-Kutta, the comparison is performed and shown in Fig 10. The total analysis time is 50 sec and the time step of flight simulation is 5×10^{-4}. Generally, Runge-Kutta has higher accuracy than that Euler approach. However, the discrepancies between those two methods are not significant, the result of Euler approach is used. The present simulation needs 5 min to obtain the simulation result. In contrast to

the present flight simulation, the simulation based on simple aerodynamics takes 2 min to compute the flight dynamics. The reason is that the present flight simulation is not optimized. Thus, it is necessary to optimize the algorithm and code to improve the computational time.
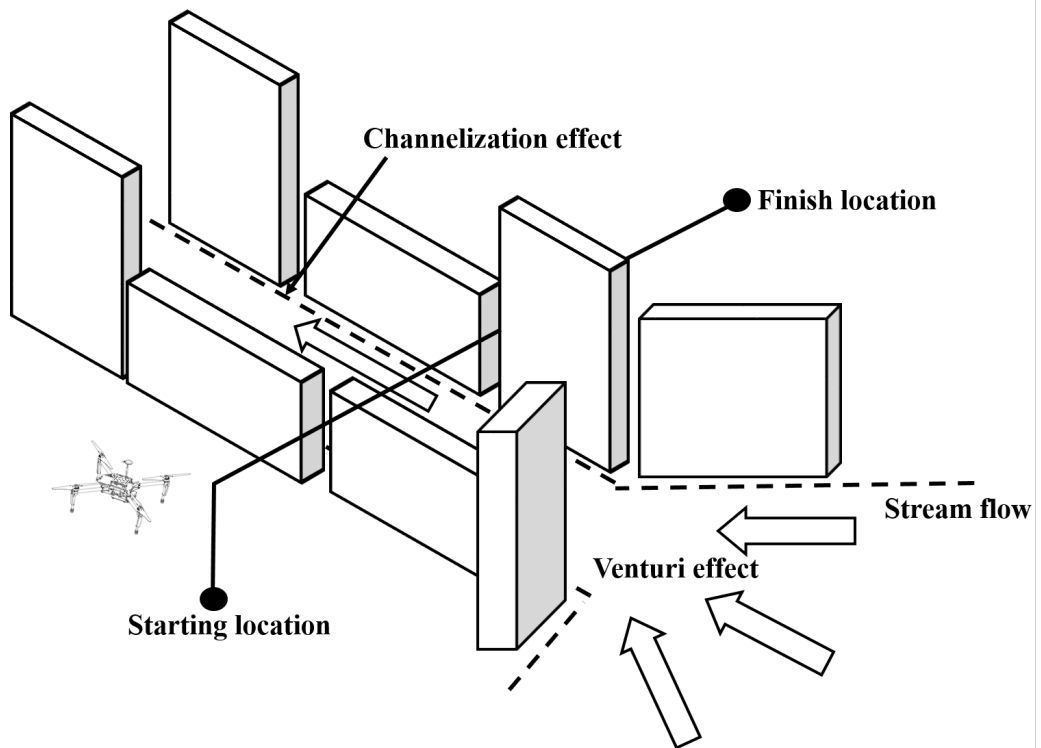
Figure 5.26 Concept of the venturi and channelization effect in an urban infrastructure
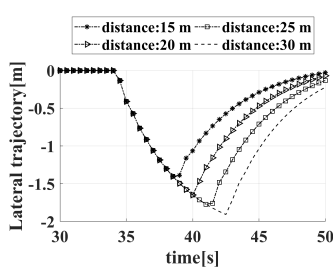
(a) Trajectory at 9 m/s gust situation
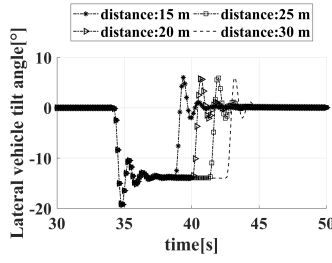
(b) Vehicle tilting angle at 9 m/s gust situation
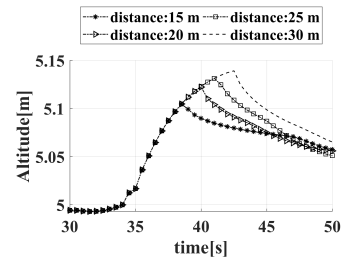
(c) Altitude at 9 m/s gust situation
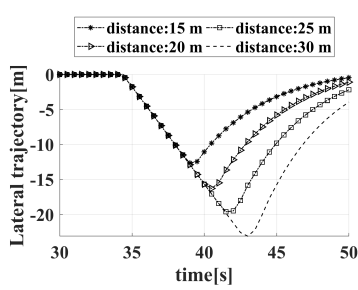
(d) Trajectory at 18 m/s gust situation
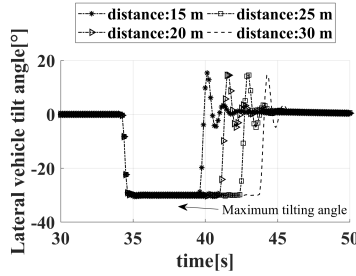
(e) Vehicle tilting angle at 18 m/s gust situation
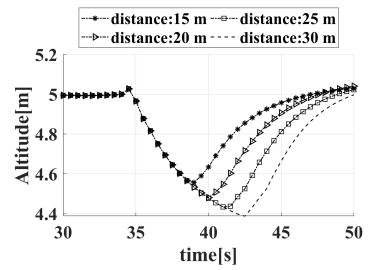
(f) Altitude at 18 m/s gust situation

Figure 5.27   Effect upon the transient behavior in terms of the distance
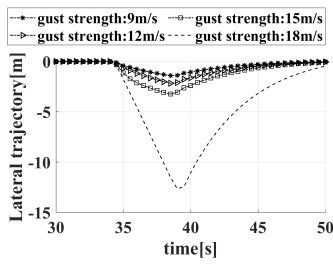
(a) Trajectory (distance: 15 m) **(b)** Vehicle tilting angle (distance: 15 m) **(c)** Altitude (distance: 15 m)
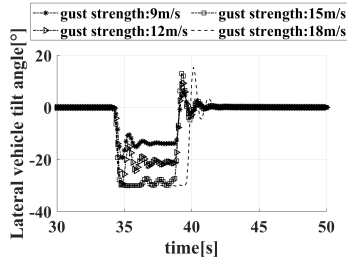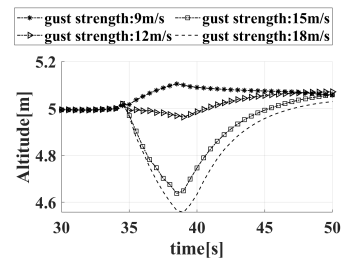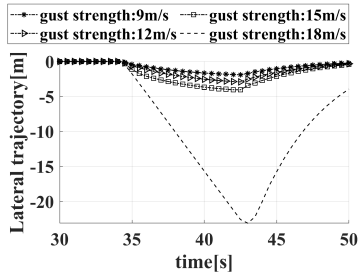
(d) Trajectory (distance: 30 m) **(e)** Vehicle tilting angle (distance: 30 m) **(f)** Altitude passing (distance: 30 m)
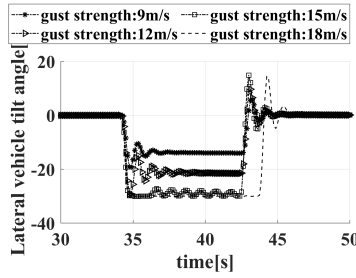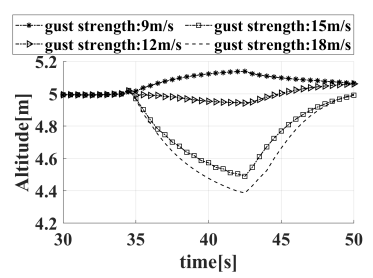
Figure 5.28   Effect upon the transient behavior in terms of the gust speed
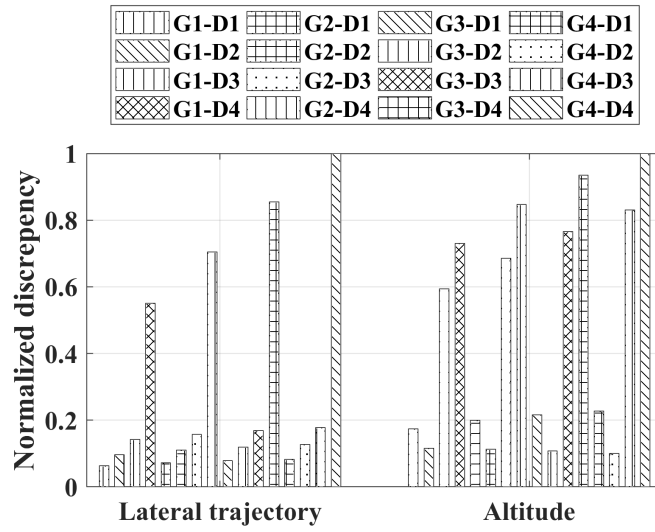
Figure 5.29 Results for the trajectory and altitude in terms of the gust strength and distance
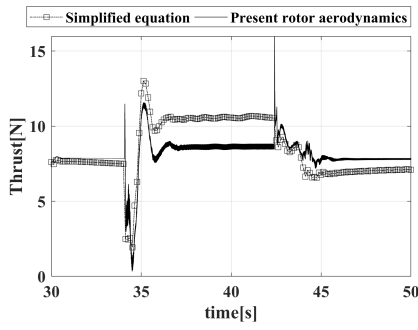
(a) Thrust result for Rotor 1
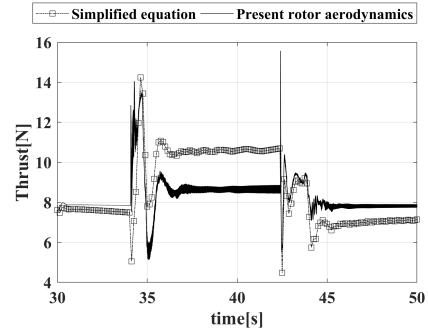
(b) Thrust result for Rotor 2
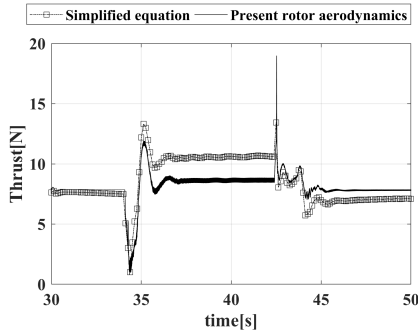
(c) Thrust result for Rotor 3
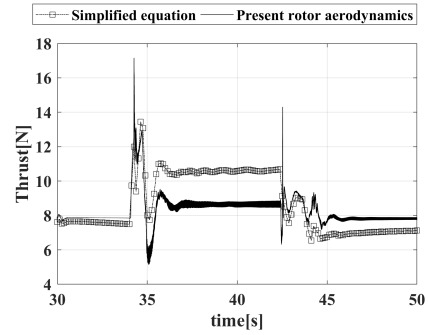
(d) Thrust result for Rotor 4

Figure 5.30 Comparison between the rotor aerodynamics and simplified equation under the increased gust intensity
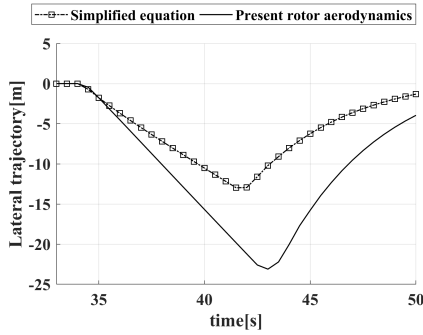
(a) Trajectory
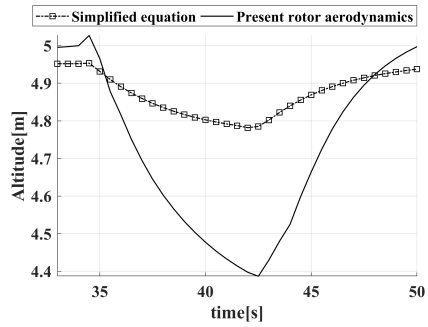
(b) Altitude

Figure 5.31 Comparison of the transient behavior between the rotor aerodynamics and simplified equation

180
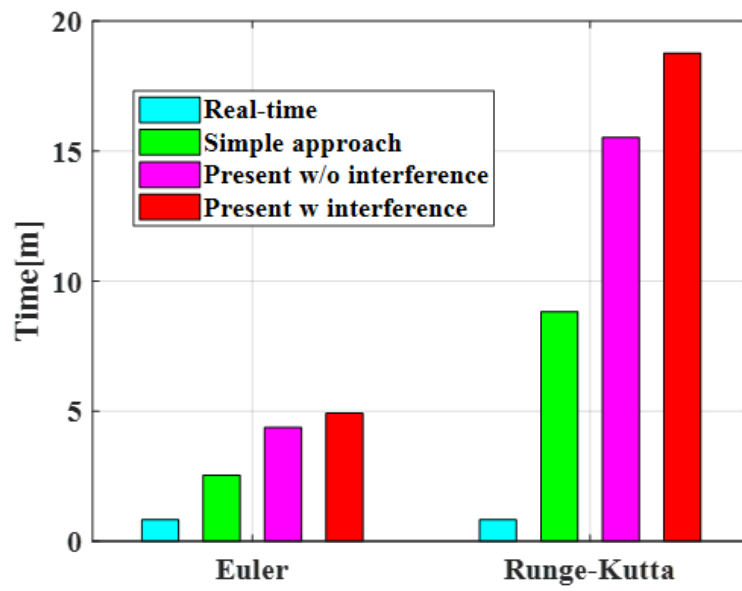
Figure 5.32   Computational time result

Table 5.10 Comparison of the average value of the gust result

Gust \ Distance	D1	D2	D3	D4
G1	(9[m/s], 15[m])	(9[m/s], 20[m])	(9[m/s], 25[m])	(9[m/s], 30[m])
G2	(12[m/s], 15[m])	(12[m/s], 20[m])	(12[m/s], 25[m])	(12[m/s], 30[m])
G3	(15[m/s], 15[m])	(15[m/s], 20[m])	(15[m/s], 25[m])	(15[m/s], 30[m])
G4	(18[m/s], 15[m])	(18[m/s], 20[m])	(18[m/s], 25[m])	(18[m/s], 30[m])

6 Conclusion

This dissertation establishes a real-time multirotor UAV flight simulation based on the proposed rotor aerodynamic analysis considering aerodynamic interference among the rotors. To improve the accuracy of the flight simulation, the proposed rotor aerodynamics which includes the unsteady rotor aerodynamic analysis and extended formulation for the aerodynamic interference is developed. Such rotor aerodynamics is validated and shows good agreement with both experiment and high-fidelity analysis. In addition, the integration approach with the present rotor aerodynamics and nonlinear flight dynamics is proposed to establish a flight simulation. To evaluate the present flight simulation, a systematic procedure is performed and validated step by step. Furthermore, the transient behavior of UAV is investigated and compared against the gust experiment. The major contributions of this dissertation are listed as follows.

- For improving the accuracy of a multirotor UAV flight simulation, this dissertation suggests the present rotor aerodynamic analysis which includes the rigid blade flapping, and dynamic inflow. In addition, the importance of the rigid blade flapping to capture the correct tendency of the aerodynamic drag is founded and proposed. Based on this analysis, aerodynamic loads for an

isolated rotor of a multirotor UAV are estimated and validated suitably under hover, climb and forward flight conditions.

- A novel formulation is proposed to consider the aerodynamic interference among the rotors. This formulation is based on the dynamic vortex tube approach. In addition, this formulation is expanded to take into account the rotational direction and side-slip angle to be implemented in the flight simulation. To avoid numerical integration, Taylor series expansion which uses multiple nominal points is applied. Using this formulation, the physical trends of the aerodynamic interference among the rotors are captured and verified by various multirotor configurations such as the tandem, side-by-side, quadrotor, and hexarotor which are non-overlapping.

- Specifically, the result obtained by the present interference formulation shows good agreement with the high-fidelity analysis and experimental results. However, there is still room for the verification of a side-by-side configuration because the evaluation for an intermediate angle from $0\,^\circ$ to $90\,^\circ$ is not performed. Thus, an additional evaluation will be necessary for those situations of a side-by-side configuration. Although several validations are required, the proposed formulation is a suitable approach to consider the interference among the rotors.

- The integration procedure between the proposed aerodynamic analysis and flight dynamics is performed to predict an accurate behavior of a multirotor UAV. A systematic procedure is established to validate the proposed flight simulation. By this procedure, the complex features of a multirotor UAV

including the dynamics, controller, and aerodynamics are identified step by step. Thus, the result obtained by the present flight simulation shows good agreement with the flight test. Furthermore, it is found that the present flight simulation is more accurate than that of the conventional simulation which uses a simplified aerodynamics.

- The gust experiment that corresponds to urban operations is performed and compared with the present flight simulation. In addition, an efficient approach is proposed to estimate an unidentified gust. This estimation approach exhibits good agreement for both simulation results and flight test. Furthermore, the transient behavior of UAV due to the gust is compared. The result predicted by the present simulation is well-corrected for both longitudinal and lateral dynamics. Therefore, the present flight simulation is capable of capturing the transient behavior of UAV due to the gust.

- Further investigations are performed to identify the effect of rigid blade flapping and aerodynamic interference effect. As the rigid blade flapping affects the forward speed of UAV, it is an important factor to consider in the long flight mission. In contrast to the rigid blade flapping, the result with interference and without interference has few discrepancies. However, the rotational speed of the rotors shows significant discrepancies. Due to this result, consideration of the aerodynamic interference among the rotors is necessary to predict the accurate dynamics of the rotor.

- In addition, an investigation for quadrotor UAV due to the large intensity gust is performed. By this investigation, it is found that the altitude of UAV is

influenced by the gust strength and exposed distance significantly. Furthermore, the accuracy of the simplified rotor aerodynamics is dramatically decreased when the intensity of the gust is increased. Thus, it is important to consider the proper rotor aerodynamics to predict the transient behavior of a multirotor UAV under a gust with large intensity.

In the future, the accuracy of the proposed rotor aerodynamics will be enhanced to capture the trend of rolling and pitching moments. According to these enhancements,the proposed rotor aerodynamics will apply the other multirotor configuration such as a co-axial rotor. The computational time of the proposed flight simulation has a significant discrepancy against the real-time. Due to that, the rotor formulation and flight simulation will be optimized to reduce computational time to satisfy the real-time requirement. In addition, the proposed formulation will be used in the UTM system to predict the dynamic behavior due to the gust. Furthermore, the proposed flight simulation will be further developed to treat arbitrary multirotor configurations. Then, the dynamic behavior of those configurations will be investigated and validated by the proposed flight simulation.

Reference

[1] Annoymous, "Summary of Small Unmanned Aircraft Rule (Part 107)," Federal Aviation Administration, 2016

[2] Ancel, E., Capristan, F.M., Foster, J.V., and Condotta, R.C., "Real-time Risk Assessment Framework for Unmanned Aircraft System (UAS) Traffic Management (UTM)," 17th AIAA Aviation Technology, Integration, and Operations Conference, Denver, Colorado, June, 2017.

[3] Ancel, E., Capristan, F.M., Foster, J.V., and Condotta, R.C., "In-Time Non-Participant Casualty Risk Assessment to Support Onboard Decision Making for Autonomous Unmanned Aircraft," AIAA Aviation 2019 Forum, Dallas, Texas, June, 2019.

[4] Hali, B., and Alanna, W., "Urban Airflow: What Drone Pilots Need to Know," Natioanl Research Council Canada LTR-AL-2020-0075, 2021

[5] Blocken, B., Stathopoulos, T., and Beeck, J., "Pedestrian-level wind conditions around buildings: Review of wind-tunnel and CFD techniques and their accuracy for wind comfort assessment," Building and Environment, Vol. 100, No. 1, pp.50–81, 2019

[6] Zajic, D., Fernando, H., Calhoun, R., Princevac, M., Brown, M., and Pardjak, E., "Flow and Turbulence in an Rrban Canyon," Journal of Applied Meteorology and Climatology, Vol. 55, No.1, pp. 203–223, 2016

[7] Zhang, Y., Chen, Z., Zhang, X., Sun, Q., and Sun, M., "A novel control scheme for quadrotor UAV based upon active disturbance rejection control," *Aerospace Science and Technology*, Vol. 79, 2018, pp. 601–609.

[8] Waslander, S., and Wang, C., "Wind Disturbance Estimation and Rejection for Quadrotor Position Control," AIAA Infotech@Aerospace Conference, Seattle, Washington, Jan, 2009

[9] Suarez, F., and Domingeuez, S., and Campoy, P., "L1 adaptive control for Wind gust rejection in quad-rotor UAV wind turbine inspection," 2017 International Conference on Unmanned Aircraft Systems (ICUAS), Miami, FL, June, 2017.

[10] Labbadi, M. and Cherkaoui, M., "Robust adaptive backstepping fast terminal sliding mode controller for uncertain quadrotor UAV," *Aerospace Science and Technology*, Vol. 93, 2019.

[11] Foster, V., and Hartman, C., "High-Fidelity Multi-Rotor Unmanned Aircraft System Simulation Development for Trajectory Prediction Under Off-Nominal Flight Dynamics," 17th AIAA Aviation Technology, Integration, and Operations Conference, Denver, Colorado, June, 2017.

[12] Syed, A.., and Wail, G., "Intelligent Flight Control of an Autonomous Quadrotor," *Motion control*, IntechOpen, Rijeka, 2010, Chapter 12.

[13] Garcia, R. A., Rubio, F.R., and Ortega, M. G., "Robust PID control of the quadrotor helicopter," *IFAC Proceedings Volumes*, Vol. 45, No. 3, pp. 229–234, 2012

[14] Thibault, S., Holman, D., Garcia, S., and Trapani, G., "CFD Simulation of a quad-rotor UAV with rotors in motion explicitly modeled using an LBM approach with adaptive refinement," 55th AIAA Aerospace Sciences Meeting, Grapevine, TX, Jan, 2017.

[15] Diaz, P.V., and Yoon, S., "High-fidelity computational aerodynamics of multi-rotor unmanned aerial vehicles," 2018 Sci-tech Forum AIAA Aerospace Sciences Meeting, Kissimmee, Florida, Jan, 2018.

[16] Misiorowski, M., Gandhi, F. and Oberai, A.A., "A Computational Study on Rotor Interactional Effects for a Quadcopter in Edgewise Flight," 74th Annual Forum of the American Helicopter Society, Phoenix, Arizona, May, 2018.

[17] Barcelos, D., Kolaei, A., and Bramesfeld, G., "Aerodynmaic Intercations of Quadrotor Configurations," *Journal of Aircraft*, Vol. 57, (6), 2020.

[18] Peters, D.A., "How Dynamic Inflow Survives in the CompetitiveWorld of Rotorcraft Aerodynamics The Alexander Nikolsky Honorary Lecture," *Journal of the american helicopter society*, Vol. 54, 2009.

[19] Gur, O., and Rosen, A., "Comparison between blade-element models of propellers," The Aeronautical Journal, Vol. 112, No. 1138, 2008, pp. 689–704

[20] Michael, O., Cale, Z., and Mike, L., "Analytical/Experimental Comparison for Small Electric Unmanned Air Vehicle Propellers," 26th AIAA Applied Aerodynamics Conference, Honolulu, Hawaii, Jan, 2008.

[21] Brandt, B. J,. and Selig, S., "Propeller Performance Data at Low Reynolds Numbers," 49th AIAA Aerospace Sciences Meeting, Orlando, FL, Jan, 2011.

[22] Khan, W., and Nahon, M., "Toward an accurate physics-based UAV thruster model," IEEE/ASME Transactions on Mechatronics, Vol. 18, No. 4, pp. 1260–1279, 2013.

[23] Robert, W., and Gavin, K., and Michael, S., " Reynolds number effects on the performance of small-scale propellers," 32nd AIAA applied aerodynamics conference, Atlanta, GA, Jan, 2014.

[24] Khan, W., and Nahon, M., "A propeller model for general forward flight conditions," International Journal of Intelligent Unmanned Systems, Vol. 3, No. 1, pp. 72–92, 2015.

[25] MacNeill, R., and Verstraete, D., "Blade element momentum theory extended to model low Reynolds number propeller performance," The Aeronautical Journal, Vol. 121, No. 1240, pp. 835–857, 2017

[26] McCrink, M., and Gregory, J., "Blade element momentum modeling of low-Reynolds Electric propulsion systems," Journal of Aircraft," Vol. 54, No.1, pp.163–176, 2017.

[27] Shetty, O., and Selig, M., "Small-scale propellers operating in the vortex ring state," 49th AIAA Aerospace Sciences Meeting including the New Horizons Forum and Aerospace Exposition, Orlando, FL, Jan, 2011.

[28] Theys, B., Dimitriadis, G., Hendrick, P., and Schutter, J., "Experimental and numerical study of micro-aerial-vehicle propeller performance in oblique flow," Journal of Aircraft," Vol. 54, No.3, pp.1076–1084, 2017.

[29] Leishman, J. G., *Principles of Helicopter Aerodynamics*, Cambridge University Press, New York, 2006, Chapter 3.

[30] Shao, M., Lu, Y., Xu, X., Guan, S., and Lu, J., "Experimental study on noise reduction of multi-rotor by phase synchronization," Journal of Sound and Vibration, Vol. 539, pp. 1–18, 2022

[31] Tinney, C.E., and Sirohi, J., "Multirotor Drone Noise at Static Thrust," AIAA Journal, Vol. 56, No. 7, pp. 2816–2826, 2018

[32] Xu, X., Lu, Y., Shao, M., and Lan, C., "Fast prediction method for multirotor global tonal noise based on acoustic modal analysis," Mechanical Systems and Signal Processing, Vol. 183, pp.1–31, 2023

[33] Zhou, W., Zhe, N., Li, H., and Hu, H., "An Experimental Investigation into Rotor-to-Rotor Interactions of Small UAV," AIAA Aviation Forum, 35th AIAA Applied Aerodynamics Conference, Denver, CO, Jun, 2017.

[34] Shukla, D., Komerath, N., "Low Reynolds number multirotor aerodynamic wake interactions," *Experiments in Fluids*, Vol. 60, (77), 2019, pp.1–14.

[35] Chen, G.H., Nunez, G.F., Russell, C.R., Avera, M.P., and Dotterweich, J.M., "Wind Tunnel Test Results for an Overlapped Quadrotor Configured UAS," AHS International 74th Annual Forum and Technology Display, Phoenix, Arizona, May, 2018.

[36] Russell, C.R., Jung, J. and Wilink, G., and Glasner, B., "Wind Tunnel and Hover Performance Test Results for Multicopter UAS Vehicles," 72nd Annual Forum of the American Helicopter Society, West Palm Beach, FL, May, 2016.

[37] Russell, C.R., and Conley, S., "The Multirotor Test Bed – A New NASA Test Capability for Advanced VTOL Rotorcraft Configurations ," Vertical Flight Society's 76th Annual Forum and Technology Display, Virtual, Oct, 2020.

[38] Atte, A., Wylie, D., and Rauleder, J., "Experimental Evaluation of Multi-Rotor Aerodynamic Interactions," Vertical Flight Society's 78th Annual Forum and Technology Display, Ft. Worth, Texas, May, 2022.

[39] Zhao, J., and He, C., " Real-Time Simulation of Coaxial Rotor Configurations with Combined Finite State DynamicWake and VPM," 70th Annual Forum and Technology Display of the American Helicopter Society International, Montreal, Quebec, Canada, May, 2014.

[40] He, C., and Rajmohan, N., "State-Space Inflow Model Identification from Viscous Vortex Particle Method for Advanced Rotorcraft Configurations," 73rd Annual Forum and Technology Display of the American Helicopter Society International, Fort Worth, Texas, May, 2017.

[41] He, C., Gladfelter, M., Chang, C., Tischler, M. B., and Juhasz, O., "VPM Derived State Space Inflow Model for Multi-rotor Air Vehicle Modeling and Simulation," Vertical Flight Society 75th Annual Forum and Technology Display, Philadelphia, PA, May, 2019.

[42] Rand, O., Khromov, V., Hersey, S., Celi, R., Juhasz, O., and Tischler, M. B., "Linear Inflow Model Extraction from High-Fidelity Aerodynamic Models for Flight Dynamics Applications," 71st Annual Forum and Technology Display of the American Helicopter Society International, Virginia Beach, Virginia, May 2015.

[43] Rand, O. and Khromov, V., "Parametric Study of Dynamic Inflow for Single and Coaxial Rotor Systems," *Journal of the American Helicopter Society*, Vol. 63, (4), 2018, pp. 1-–14.

[44] Keller, J. D., McKillip Jr., R. M., Wachspress, D. A., Tischler, M. B., and Juhasz, O., "A Free Wake Linear Inflow Model Extraction Procedure for Rotorcraft Analysis," 73rd Annual Forum and Technology Display of the American Helicopter Society International, Fort Worth, Texas, May, 2017.

[45] Keller, J. D., McKillip Jr., R. M., Wachspress, D. A., Tischler, M. B., and Juhasz, O., "Linearized Inflow and Interference Models from High Fidelity FreeWake Analysis for Modern Rotorcraft Configurations," Vertical Flight Society 75th Annual Forum and Technology Display, Philadelphia, PA, May, 2019.

[46] Prasad, J. V. R., Kong, Y. B., and Peters, D. A., "Analytical Methods for Modeling Inflow Dynamics of a Coaxial Rotor System," 42nd European Rotorcraft Forum, Lille, France, Sep, 2016.

[47] Kong, Y. B., Prasad, J. V. R., Sankar, L. N., and Kim, J, "Finite State Coaxial Rotor Inflow Model Improvements via System Identification," 72nd Annual Forum and Technology Display of the American Helicopter Society International, West Palm Beach, FL, May, 2016.

[48] Kong, Y. B., Prasad, J. V. R., and Peters, D. A., "Development of a Finite State Dynamic Inflow Model for Coaxial Rotor Using Analytical Methods," 73rd Annual Forum and Technology Display of the American Helicopter Society International, Fort Worth, Texas, May, 2017.

[49] Kong, Y. B., "Development of a Finite State Coaxial Rotor Dynamic Inflow Model," Ph.D. dissertation, School of Aerospace Engineering, Georgia Institute of Technology, Atlanta, GA, Aug 2018.

[50] Kong, Y. B., Prasad, J. V. R., and He, C., "Finite State Coaxial Rotor Inflow Model Enhancements Using VVPM-Extracted Influence Coefficients," *Journal of the American Helicopter Society*, Vol. 65, (2), 2020, pp. 1-–17.

[51] Guner, F., "Development and Analysis of Finite State Multi-Rotor Dynamic Inflow Models," Ph.D. dissertation, School of Aerospace Engineering, Georgia Institute of Technology, Atlanta, GA, May 2021.

[52] Luo, J., Zhu, L., and Yan, G., "Novel Quadrotor Forward-Flight Model Based on Wake Interference," *AIAA Journal*, Vol. 53, (12), 2015, pp.3522—3533.

[53] Nguyen, D.H., Liu, Y., and Mori, K., "Experimental Study for Aerodynamic Performance of Quadrotor Helicopter," *Transactions of the Japan Society for Aeronautical and Space Sciences*, Vol. 61, No. 1, 2018, pp.29–39.

[54] Han, D., and Barakos, G.N., "Aerodynamic Interference Model for Multirotors in Forward Flight," *Journal of Aircraft*, Vol. 57, No. 6, 2020, pp.1220–1223.

[55] Johnson, W., *Helicopter Theory*, Dover, New York, 1994, Chapter 4.

[56] Guner, F., and Prasad, J.V.R., "Combined Momentum and Simple Vortex Theory Inflow Model for Multi-Rotor Configurations," *Journal of the American Helicopter Society*, Vol. 67, 02207, 2022.

[57] Heyson, H.H., "Equations For The Induced Velocities Near A Lifting Rotor With Nonuniform Azimuthwise Vorticity Distribution," NASA TND-394, 1960.

[58] Kim, H., Lim, D., and Lee, K., "Flight Performance with Respect to Rotor Rotation Directions of Multirotor Aircraft," *AIAA Journal*, Vol. 61, (5), 2023, pp.2189—2207.

[59] Usov, D., Appleton, W., Filippone, A., and Bojdo, N., "Low-Order Aerodynamic Model for Interference in Multirotor Systems," *Journal of Aircraft*, Vol. 59, (6), 2022, pp.1450—1462.

[60] Guner, F., "A Multirotor Inflow Model Based on Combined Momentum Theory and Simple Vortex Theory (CMTSVT) for Flight Simulations," Vertical Flight Society 78th Annual Forum and Technology Display, Ft. Worth, Texas, May, 2022.

[61] Guner, F., "Hover Performance Predictions of Coaxial Rotor Configurations Using the Updated CMTSVT Multirotor Inflow Model," 48th European Rotorcraft Forum, Winterthur, Switzerland, Sep, 2022.

[62] Sutherland, M., Etele, J., and Fusina, G., "Urban Wake-Field Generation using Large-Eddy Simulation for Application to Quadrotor Flight," *Journal of Aircraft*, Vol. 53, No.3, 2016, pp.1224–1236.

[63] Foster, V., Miller, J., Busan, C., Langston, L., Hartman, C., "Recent NASA Wind Tunnel Free-Flight Testing of a Multirotor Unmanned Aircraft System," AIAA Aviation 2020 Forum, Orlando, FL, Jan, 2020.

[64] Davoudi, B., Taheri, E., Duraisamy, K., Jayaraman, B., and Kolmanovsky, I., " Quad-Rotor Flight Simulation in Realistic Atmospheric Conditions," *AIAA Journal*, Vol. 58, No.5, 2020, pp. 1992–2004

[65] Annoymous, Flying Qualities of Piloted Airplanes. U.S. Military Specification MIL-F-8785C, U.S. Department of Defense, 1980

[66] Shastry, A., Kothari, M., and Abhishek, A., "Generalized Flight Dynamic Model of Quadrotor Using Hybrid Blade Element Momentum Theory," *Journal of Aircraft*, Vol. 55, No.5, 2018, pp.2162–2168.

[67] Hali, B., and Alanna, W., Urban Airflow: What Drone Pilots Need to Know, Natioanl Research Council Canada LTR-AL-2020-0075, 2021.

[68] Schajnoha, S., Larose, G., Labbad, M., Barber, H., and Wall, A., "The Safety of Advanced Air Mobility and The Effects of Wind in the Urban Canyon," Vertical Flight Society's 78th Annual Forum, Ft. Worth, TX, May, 2022.

[69] Craig, W., Yeo, D., and Paley, D., "Geometric Attitude and Position Control of a Quadrotor in Wind," *Journal of Guidance, Control, and Dynamics*, Vol. 43, No. 5, 2020, pp. 870–883.

[70] Raza, S., and Etele, J., "Autonomous Position Control Analysis of Quadrotor Flight in Urban Wind Gust Conditions," AIAA SciTech Forum, San Diego, California, Jan, 2016.

[71] Raza, S., Sutherland, M., Etele, J., Fusina, G., "Experimental validation of quadrotor simulation tool for flight within building wakes," *Aerospace Science and Technology*, Vol. 67, No. 3, 2017, pp. 169–180.

[72] Javier, G., Craig, A., Cornel, S., and Stephan, F., "Sensing Wind from Quadrotor Motion," *Journal of Guidance, Control, and Dynamics*, Vol. 42, No. 4, 2019, pp. 836–852.

[73] Azid, S., Kumar, K., Cirrincion, M., and Fagiolini, A., "Wind gust estimation for precise quasi-hovering control of quadrotor aircraft," *Control Engineering Practice*, Vol. 116, 2021, pp. 104930.

[74] Park, S., Yoo, J., and Shin, S., "Improved Aerodynamic Analysis for Multirotor-Type UAS Flight Simulation Using Dynamic Inflow and Rigid Blade Flapping," *Journal of Aerospace Engineering*, Vol. 33, (4), 2020, pp.04020021-1–12.

[75] Park, S., Im, B., Lee, D., and Shin, S., "Aerodynamic interference analysis for a non-overlapping multirotor UAV based on dynamic vortex tube," *Journal of the American Helicopter Society*, Vol. 68, 042010, 2023, pp.1–21.

[76] Park, S., Yoo, J., Lee, S., and Shin, S., "Real-Time Flight Simulation for Multirotor UAV Integrated with the Dynamic Inflow Aerodynamics," *Journal of the American Helicopter Society*, Vol. 66, 042008, 2021, pp.1–14.

[77] Park, S., Yoo, J., Lee, S., and Shin, S., "Prediction on Nonlinear Flight Dynamics of a Quad-rotor UAV with rotor aerodynamic analysis under Gust," Vertical Flight Society's 76th Annual Forum, Virtual, Oct, 2020.

[78] Park, S., Lee, S., Im, B., Lee, D., and Shin, S., "Improvement of a multi-rotor UAV flight response simulation influenced by gust," *Aerospace Science and Technolog*, Vol. 134, 108156, 2023, pp.1–17

[79] Bramwell, A., Balmford, D., Done, G., *Bramwell's helicopter dynamics*, Elsevier, 2001.

[80] Pitt, D. M. and Peters, D. A. "Theoretical prediction of dynamic-inflow derivatives," 6th European Rotorcraft and Powred Lift Aircraft Forum, Bristol, England., 1980.

[81] Peters, D.A., and HaQuang, N., "Dynamic Inflow for Practical Applications," *Journal of the American Helicopter Society*, Vol. 33, (4), 1988, pp. 64–68

[82] Mangler, K., "Calculation of the Induced Velocity Field of a Rotor," Royal Aircraft Establishment, Reoprt No. Aero 2247, 1984.

[83] Pitt, D., "Rotor Dynamic Inflow Derivatives and Time Constants From Various Inflow Models," Ph.D. dissertation, School of Aerospace Engineering, Institute of Washington University, Saint Louis, Missouri, December 1980.

[84] Peters, D.A., "How Dynamic Inflow Survives in the CompetitiveWorld of Rotorcraft Aerodynamics The Alexander Nikolsky Honorary Lecture," *Journal of the american helicopter society*, Vol. 54, 2009.

[85] Glauert, H., *Airplane propellers*, Springer, 1935.

[86] Hoffmann, G., Huang, H., Waslander, S., and Tomlin, C., "Quadrotor helicopter flight dynamics and control: Theory and experiment," AIAA guidance, navigation and control conference and exhibit, Hilton Head, South Carolina, Jun, 2007.

[87] Zhao, J., Prasad, J.V.R., and Peters, D.A., "Rotor Dynamic Wake Distortion Model for Helicopter Maneuvering Flight," *Journal of the American Helicopter Society*, Vol. 49, (4), 2004, pp. 414-–424.

[88] Zhao, J., "Rotor Dynamic Wake Distortion Model for Helicopter Maneuvering Flight," Ph.D. dissertation, School of Aerospace Engineering, Georgia Institute of Technology, Atlanta, GA, March 2005.

[89] Goulos, I., "An Improved Analytical Approach for Modeling the Effect of Rotor Wake Curvature Using Finite-State Induced Flow Models," *Journal of the American Helicopter Society*, Vol. 61, 032010, 2016.

[90] Peirce, B.O., *A Short Table of Integrals. Third rev. ed.,*, Ginn & company, New York, Boston, 1929, pp. 10, 24, 34, and 80.

[91] Misiorowski, M., Gandhi, F., and Oberai, A. A., "A Computational Study on Rotor Interactional Effects for a Quadcopter in Edgewise Flight," *AIAA Journal*, Vol. 57, (12), 2019, pp.5309—5319.

[92] Hartman, D., Landis, K., Mehrer, M., Moreno, S. and Kim, J., "Quadcopter dynamic modeling and simulation (Quad-Sim)," *https://github.com/dch33/Quad-Sim.*, 2014.

[93] Christian, A., and Lawrence, J., "Initial Development of aQuadcopter Simulation Environment for Auralization," 72nd Annual Forum of the American Helicopter Society, West Palm Beach, FL, May, 2016.

[94] Zhang, S., Wei, D., Huynh, M.Q., Quek, J.X., Ma, X., and Xie, L., "Model Predictive Control Based Dynamic Geofence System for Unmanned Aerial Vehicles," 2017 Sci-Tech Forum AIAA Aerospace Sciences Meeting, Grapevine, Texas, Jan, 2017.

[95] Bhattarai, S., Poudel, K.R., Bhatta, N., Mahat, S., and Bhattrai, S., "Modeling and Development of Baseline Guidance Navigation and Control System for Medical Delivery UAV," 2018 Sci-Tech Forum AIAA Aerospace Sciences Meeting, Kissimmee, Florida, Jan, 2018.

[96] Javier, G., Craig, A., Cornel, S., and Stephan, F., "Sensing Wind from Quadrotor Motion," *Journal of Guidance, Control, and Dynamics*, Vol. 42, No. 4, 2019, pp. 836–852.

[97] Padfield, G. D., *Helicopter Flight Dynamics: Including a Treatment of Tiltrotor Aircraft - Third edition*, John Wiley and Sons, Oxfod, UK, 2018, Chapter 3.

[98] Vahdanipour, M. and Khodabandeh, M., "Adaptive fractional order sliding mode control for a quadrotor with a varying load," *Aerospace Science and Technology*, Vol. 86, 2019, pp. 737–747.

[99] Schiano, F., Mora, J. A., Rudin, K., Beardsley, P., Siegwart, R., and Siciliano, B., "Towards Estimation and Correction of Wind Effect on a Quadrotor UAV," 2014 International Micro Air Vehicle Conference and Competition, Delft, Netherlands, August, 2014.

[100] Niemiec, R., and Gandhi, F., "Multirotor Controls, Trim, and Autonomous Flight Dynamics of Plus- and Cross-Quadcopters," *Journal of aircraft*, Vol. 54, (5), 2017. pp. 1910–1920.

[101] Austin, D.T., Beatrice, R., Jay, S., and Sheryl, M.G., "Multirotor Trim using Loose Aerodynamic Coupling," VFS Aeromechanics for Advanced Vertical Flight Technical Meeting, San Jose, CA, Jan, 2020.

[102] Mark, B., Robert, K., *Aircraft and Rotorcraft System Identification Engineering Methods with Flight Test Examples*, AIAA Education Series, 2012

[103] Park, S., Eun, W., and Shin, S., "Hybrid Analysis for Quadrotor Type UAV and Modified Blade Element Momentum Theory Considering Gust and Flight Condition," AIAA Scitech 2019 Forum, San Diego, California, Jan, 2019.

[104] Allison, S., Bai, H., and Jayaraman, B., "Wind estimation using quadcopter motion: A machine learning approach," *Aerospace Science and Technology*, Vol. 98, 2020, pp.105699 1–13.

[105] Xiang, X., Wang, Z., Mo, Z., Chen, G., Pham, K., and Blasch, E., "Wind field estimation through autonomous quadcopter avionics," 2016 IEEE/AIAA 35th Digital Avionics Systems Conference (DASC), Sacramento, CA, June, 2016

[106] Pramod, A., Deepan, L., Gabriel, F., Donald, B., and Moshe, K., "Wind Measurement and Simulation Techniques in Multi-Rotor Small Unmanned Aerial Vehicles," IEEE Access, Vol. 8, 2020, pp.54910-54927.

[107] Geoffrey, W. and Jordan, A. and Nate, L. and Jamey, D., "Wind Characterization Using Onboard IMU of sUAS," 2018 Atmospheric Flight Mechanics Conference, Atlanta, Georgia, June, 2018.

[108] Drela, M., "XFOIL: An analysis and design system for low Reynolds number airfoils," Low Reynolds Number Aerodynamics. Lecture Notes in Engineering, Berlin, Heidelberg, 1989

[109] Russell, C., and Sekula, M., "Comprehensive Analysis Modeling of Small-Scale UAS Rotors," 73rd AHS International Annual Forum and Technology Display, Fort Worth, TX, May, 2017.

[110] Nowicki, N., "Measurement and Modelling of Multicopter UAS Rotor Blades in Hover," NASA/CR-2016-219428, 2016.

[111] Huang, H., Hoffmann, G., Waslander, S., and Tomlin, C., "Aerodynamics and control of autonomous quadrotor helicopters in aggressive maneuvering," 2009 IEEE international conference on robotics and automation, Fort Worth, TX, May, 2009.

[112] Kolaei, A., Barcelos, D., and Bramesfeld, G., "Experimental analysis of a small-scale rotor at various inflow angles," *International Journal of Aerospace Engineering*, 2018

[113] Barcelos, D., Kolaei, A., and Bramesfeld, G., "Performance Prediction of Multirotor Vehicles Using A Higher Order Potential Flow Method," 2018 AIAA aerospace sciences meeting, Kissimmee, Florida, Jan, 2018.

[114] Hwang, J., Jung, M., and Kwon, O., "Numerical Study of Aerodynamic Performance of a Multirotor Unmanned-Aerial-Vehicle Configuration," *Journal of Aircraft*, Vol. 52, (3), 2015, pp.839–846.

[115] Yoon, S., Diaz, P.V., Boyd Jr, D.D., Chan, W.M., and Theodore, C.R., "Computational Aerodynamic Modeling of Small Quadcopter Vehicles," AHS International's 73rd Annual Forum and Technology Display, Ft. Worth, Texas, May, 2017.

[116] Jung, Y., Chang, K., Park, S., Ho, V.T., Shim, H., and Kim, M., "Reverse Engineering and Database of Off-the-Shelf Propellers for Middle-Size Multirotors," *Unmanned Systems*, Vol. 9, (4), 2021, pp.321–332.

[117] Conley, S., Russell, C., Kallstrom, K., Koning, W., and Romander, E., "Comparing RotCFD Predictions of the Multirotor Test Bed with Experimental Results," Vertical Flight Society's 76th Annual Forum and Technology Display, Virtual, Oct, 2020.

[118] Shirazi, D., "Comparison of the CHARM Predictions of the Multirotor Test Bed with Wind Tunnel Experimental Results," VFS Aeromechanics for Advanced Vertical Flight Technical Meeting, San Jose, CA, Jan, 2022.

[119] Niemiec, R., and Gandhi, F., "Multi-rotor Coordinate Transforms for Orthogonal Primary and Redundant Control Modes for Regular Hexacopters and Octocopters," 42nd Annual European Rotorcraft Forum, Lille, France, Sep, 2016.

[120] Niemiec, R., and Gandhi, F., "Effect of Elastic Blade Deformation on Trim and Vibratory Loads of a Quadcopter," AHS 73rd Annual Forum, Fort Worth, Texas, May, 2017.

[121] Jeaong, H., Jo, S., Suk, J., Kim, S., Lee, Y., Chung, I., "Modeling of aerodynamic database and robust control using disturbance observer for quadcopter," *Journal of Institute of Control, Robotics and Systems*, Vol. 24, (6), 2018. pp. 519-531.

[122] Ogata, K., *Mordern Control Engineering*, Pearson, 2010.

[123] Weerasinghe, S.R., and Monasor, M., "Simulation and Experimental Analysis of Hovering and Flight of a Quadrotor," 13th International Conference on Heat Transfer, Fluid Mechanics and Thermodynamics, Portoroz, Slovenia, July, 2017.

[124] Muzar, D., and Lanteigne, E., "Experimental Characterization of Brushless DC Motors and Propellers for Flight Application," Proceedings of The Canadian Society for Mechanical Engineering International Congress 2016, Kelowna, Canada, June, 2016.

[125] Annoymous, Flying Qualities of Piloted Aircraft. Department of Defense Handbook. mil-hdbk-1797, U.S. Department of Defense 1997.

[126] Annoymous, Flying Qualities of Piloted Aircraft. Department of Defense handbook. mil-hdbk-1797b, U.S. Department of Defense 2012.

[127] Srivastava N., Divyam, J., Ghosha, U., Priyaa, M., Saxenab, N., and Kumarc, M., "Statistical and spectral analysis of wind over a strategic location," *Journal of Water and Climate Change*, Vol. 13, No. 9, 2022, pp. 3305-3322.

[128] Lee C., and Ryu, K., "Analysis of wind data of goheung aircraft flight test center," Korean Society for Aeronuatical and Space Sceinces 2020 Fall Conference, The Korean Society for Aeronautical and Space Sciences, Jeju, Korea, Oct, 2020.

[129] Sprin, A., "Air Quality at Street-Level: Strategies for Urban Design," *Boston Redevelopment Authority*, 1986

[130] Schlapfer, M., Lee, J., and Bettencourt, L., "Urban skylines: building heights and shapes as measures of city size," *Preprint at https://arxiv.org/abs/1512.00946.*, 2015.

[131] Toparlar, Y., Blocken, B., Maiheu, B., and Heijst, G., "Impact of urban microclimate on summertime building cooling demand: A parametric analysis for Antwerp, Belgiume," *Applied Energy*, Vol. 228, 2018, pp.852–872

[132] Phan, A., Chu, T., Bui, Q., Nguyen, T., and Nguyen, V., "Preliminary Result of 3D City Modelling For Hanoi, Vietnam," 2018 5th NAFOSTED Conference on Information and Computer Science (NICS), Ho Chi Minh, Vietnam, June, 2018.

Appendix

In this section, the induced velocity due to the inner vortex tube is described. The

geometry of the vortex tube and strength of the vortex are defined as follows:

$$
\left\{
\begin{aligned}
&\boldsymbol{P_O^{1c+}} = \begin{bmatrix} K_{A1} + \frac{(1+c(\Psi_0(-1)^{rc})}{2}) \\ K_{A2} + \frac{s(\Psi_0(-1)^{rc})}{2} \\ K_{A3} \end{bmatrix}, \boldsymbol{P_O^{1c-}} = \begin{bmatrix} K_{A1} + \frac{(-1+c(\Psi_0(-1)^{rc})}{2}) \\ K_{A2} + \frac{s(\Psi_0(-1)^{rc})}{2} \\ K_{A3} \end{bmatrix}, \\[2em]
&\boldsymbol{P_O^{1s+}} = \begin{bmatrix} K_{A1} + \frac{(c(\Psi_0(-1)^{rc})}{2}) \\ K_{A2} + \frac{(-1)^{rc}+s(\Psi_0(-1)^{rc})}{2} \\ K_{A3} \end{bmatrix}, \boldsymbol{P_O^{1s-}} = \begin{bmatrix} K_{A1} + \frac{(c(\Psi_0(-1)^{rc})}{2}) \\ K_{A2} + \frac{-(-1)^{rc}+s(\Psi_0(-1)^{rc})}{2} \\ K_{A3} \end{bmatrix}, \\[2em]
&\qquad K_{A1} = \eta s(\chi)c(\theta_{xy}), \quad K_{A2} = \eta s(\chi)s(\theta_{xy}), \quad K_{A3} = -\eta c(\chi)
\end{aligned}
\right.
$$

$$\tag{A.1}$$

$$
\begin{bmatrix} \boldsymbol{\gamma_{1c+}} \\ \boldsymbol{\gamma_{1c-}} \\ \boldsymbol{\gamma_{1s+}} \\ \boldsymbol{\gamma_{1s-}} \end{bmatrix} = \begin{bmatrix} s(\Psi_0(-1)^{r_c}) & -c(\Psi_0(-1)^{r_c}) & 0 \\ -s(\Psi_0(-1)^{r_c}) & c(\Psi_0(-1)^{r_c}) & 0 \\ s(\Psi_0(-1)^{r_c}) & -c(\Psi_0(-1)^{r_c}) & 0 \\ -s(\Psi_0(-1)^{r_c}) & c(\Psi_0(-1)^{r_c}) & 0 \end{bmatrix} \begin{bmatrix} \bar{\gamma_{1c}} \\ \bar{\gamma_{1c}} \\ \bar{\gamma_{1s}} \\ \bar{\gamma_{1s}} \end{bmatrix} \tag{A.2}
$$

By using Eqs. 2.6 to 2.8 and Eqs. A.1 to A.2, the analytical formulation can be expressed as follows:

$$f_{taylor}^{k,1c+} = -\frac{\pi\left[2c(K_2^{k,1c+} + K_5^{K,1c+}) - 2s(K_2^{k,1c+})\left(ls(\alpha_{xy}) - \frac{s(K_2^{k,1c+})}{2} - r_1s(K_3^{k,1c+})\right) + \sqrt{2}c(\theta_{xy} - K_2^{k,1c+})s(\chi)K_1^{k,1c+}\right]}{3(K_4^{k,1c+} + \sqrt{2}s(\chi)(c(\theta_{xy} - K_2^{k,1c+}) + c(\theta_{xy}) - r_1c(\theta_{xy} - K_3^{k,1c+})2 - 2lc(\alpha_{xy} - \theta_{xy}))K_1^{k,1c+} + 2)} \tag{A.3}$$

where,

$$K_1^{k,1c+} = \sqrt{c(K_2)^{k,1c+} - lc(\alpha_{xy} - K_2^{k,1c+})2 - 2lc(\alpha_{xy}) - 2r_1c(K_2^{k,1c+} - K_3^{k,1c+}) + K_6^{k,1c+} + 1}$$

$$K_2^{k,1c+} = \frac{\pi(-1)^{rc}(2k-1)}{12}, \quad K_3^{k,1c+} = (-1)^{r_n}\Psi$$

$$K_4^{k,1c+} = 2c(K_2^{k,1c+}) - lc(\alpha_{xy} - K_2^{k,1c+})4 - 4lc(\alpha_{xy}) - 4r_1c(K_2^{k,1c+} - K_3^{k,1c+}) + 2K_6^{k,1c+}$$

$$K_5^{k,1c+} = \frac{c(K_2^{k,1c+})}{2} - lc(\alpha_{xy}) - r_1c(K_3^{k,1c+}) + \frac{1}{2}$$

$$K_6^{k,1c+} = 2l^2 + 2r_1^2 - 2r_1c(K_3^{k,1c+}) + lr_1c(\alpha_{xy} - K_3^{k,1c+})4$$

$$f_{taylor}^{k,1c-} = -\frac{\pi\left[2c(K_2^{k,1c-} - K_5^{K,1c-})\left(ls(\alpha_{xy}) - \frac{s(K_2^{k,1c-})}{2} - r_1s(K_3^{k,1c-})\right) - \sqrt{2}c(\theta_{xy} - K_2^{k,1c-})s(\chi)K_1^{k,1c-}\right]}{3(K_4^{k,1c-} - \sqrt{2}s(\chi)(c(\theta_{xy}) - c(\theta_{xy} - K_2^{k,1c-})2 + r_1c(\theta_{xy} - K_3^{k,1c-})2 + 2lc(\alpha_{xy} - \theta_{xy}))K_1^{k,1c-} + 2)} \tag{A.4}$$

where,

$$K_1^{k,1c-} = \sqrt{2lc(\alpha_{xy}) - lc(\alpha_{xy} - K_2^{k,1c-})2 - c(K_2^{k,1c-}) - 2r_1c(K_2^{k,1c-} - K_3^{k,1c-}) + K_6^{k,1c-} + 1}$$

$$K_2^{k,1c-} = K_2^{k,1c+}, \quad K_3^{k,1c-} = K_3^{k,1c+}$$

$$K_4^{k,1c-} = 4lc(\alpha_{xy}) - lc(\alpha_{xy} - K_2^{k,1c-})4 - 2c(K_2^{k,1c-}) - 4r_1c(K_2^{k,1c-} - K_3^{k,1c-}) + 2K_6^{k,1c-}$$

$$K_5^{k,1c-} = lc(\alpha_{xy}) - \frac{c(K_2^{k,1c-})}{2} + r_1c(K_3^{k,1c-}) + \frac{1}{2}$$

$$K_6^{k,1c-} = K_6^{k,1c+}$$

$$f_{taylor}^{k,1s+} = -\frac{\pi[\frac{2s(K_9^{k,1s+})(s(K_9^{k,1s+})}{2} - ls(\alpha_{xy}) + \frac{(-1)^{r_c}}{2} - r_1s((-1)^{r_n}\Psi)) - 2c(K_9^{k,1s+})(lc(\alpha_{xy}) - \frac{c(K_9^{k,1s+})}{2} + r_1c((-1)^{r_n}\Psi)) + K_{10}^{k,1s+}]}{(3((K_1^{k,1s+})^2 + s(\chi)(c(\theta_{xy} - K_9^{k,1s+}) + (-1)^{r_c}s(\theta_{xy}) - 2r_1c(\theta_{xy} - (-1)^{r_n}\Psi) - 2K_1^{k,1s+}lc(\alpha_{xy} - \theta_{xy}))}$$

(A.5)

where,

$$K_1^{k,1s+} = \sqrt{4l^2 + 4r_1^2 + 1 + K_5^{1s+} + K_8^{1s+} + K_6^{1s+} - K_7^{1s+} + K_4^{1s+} - K_2^{1s+} - K_3^{1s+}}$$

$$K_2^{k,1s+} = 4(-1)^{r_c}ls(\alpha_{xy}), \quad K_3^{k,1s+} = 4(-1)^{r_c}r_1s((-1)^{r_n}\Psi), \quad K_4^{k,1s+} = 8lr_1c(\alpha_{xy} - (-1)^{r_n}\Psi)$$

$$K_5^{k,1s+} = 2(-1)^{r_c}s(K_9^{1s+}), \quad K_6^{k,1s+} = 4lc(\alpha_{xy} - K_9^{1s+}), \quad K_7^{k,1s+} = 4r_1c(K_9^{1s+} - (-1)^{r_n}\Psi)$$

$$K_8^{k,1s+} = (-1)^{2r_c}, \quad K_9^{k,1s+} = \frac{\pi(-1)^{r_c}(2k-1)}{12}, \quad K_{10}^{k,1s+} = c(\theta_{xy} - K_9^{k,1s+})s(\chi)K_1^{k,1s+}$$

$$f_{taylor}^{k,1s-} = -\frac{\pi\left[\frac{2c(K_9^{k,1s-})\left(\frac{-c(K_9^{k,1s-})}{2} + lc(\alpha_{xy}) + r_1 c((-1)^{r_n}\Psi)\right) + 2s(K_9^{k,1s-})\left(ls(\alpha_{xy}) - \frac{s(K_9^{k,1s-})}{2} + \frac{(-1)^{r_c}}{2} + r_1 s((-1)^{r_n}\Psi)\right) - K_{10}^{k,1s-}}{\left(3\left((K_1^{k,1s-})^2 - s(\chi)\left((-1)_c^r s(\theta_{xy}) - c(\theta_{xy} - K_9^{k,1s-}) + 2r_1 c(\theta_{xy} - (-1)^{r_n}\Psi) + 2lK_1^{k,1s-}c(\alpha_{xy} - \theta_{xy})\right)\right)\right)}\right]$$

(A.6)

where,

$$K_1^{k,1s-} = \sqrt{4l^2 + 4r_1^2 + 1 - K_5^{1s-} + K_8^{1s-} - K_6^{1s-} - K_7^{1s-} + K_4^{1s-} + K_2^{1s-} + K_3^{1s-}}$$

$$K_2^{k,1s-} = K_2^{k,1s+}, \quad K_3^{k,1s-} = K_3^{k,1s+}, \quad K_4^{k,1s-} = K_4^{k,1s+}, \quad K_5^{k,1s+} = K_5^{k,1s-}$$

$$K_6^{k,1s+} = K_6^{k,1s-}, \quad K_7^{k,1s+} = K_7^{k,1s-}, \quad K_8^{k,1s+} = K_8^{k,1s-}, \quad K_9^{k,1s+} = K_9^{k,1s-}$$

$$K_{10}^{k,1s-} = c(\theta_{xy} - K_9^{k,1s-})s(\chi)K_1^{k,1s-}$$

211

초 록

다중로터 무인항공기(UAV)는 제조 및 제어가 용이하다는 장점이 있다. 이러한 장점들로 인해, 무인 항공기는 민간 및 군사 분야에서 널리 사용되어 왔다. 최근, 도시에서의 무인 항공기 운영에 대한 수요가 증가함에 따라 무인 항공기의 주요 용도가 개인 취미에서 도시 인프라와 관련된 상업적 운영으로 변경되고 있다. 그러나 돌풍으로 인한 비행 불안정, 추락 사고 등의 위험 때문에 도심에서 무인 항공기를 운용하는 것은 쉽지 않다. 돌풍과 관련된 위험을 정량화하기 위해 UAV의 동적 거동을 정확하게 예측하는 것이 중요하다. 따라서, 본 논문은 동적 거동의 정확성을 보장할 수 있는 다중로터 무인 항공기 비행 시뮬레이션 개발을 목표로 한다. 예측 정확도를 높이기 위해 다음과 같은 사항들을 본 비행 시뮬레이션에 적용하였다. 첫번째로, 로터의 공기역학 하중을 도출하기 위해 적용이 용이한 로터 해석 기법을 제시하였다. 이 로터 분석에서는 동적 유입류 기법과 강성 블레이드 플랩핑이 고려되었다. 그러나 기존의 동적 유입류 기법은 단일 로터에 대해서만 개발되었기 때문에 로터 간의 공기역학적 간섭을 고려하기 위해 효율적이며 간략화된 새로운 방식의 정식화를 유도하였다. 그런 다음 비행 역학과 제안된 로터 공기 역학을 결합하여 비행 시뮬레이션을 구축한다. 트림 분석을 통해 얻은 로터의 회전 속도 및 동체 틸팅 각도 제한과 같은 몇 가지 제약 조건이 현재 비행 시뮬레이션에 적용된다. 또한, 현재 시뮬레이션을 위해 식별되지 않은 돌풍을 추정하는 간단한 접근법을 개발 및 적용하였다. 현재 비행 시뮬레이션에 대한 검증 절차는 단계별로 수행된다.

현재 로터 공기역학에서 얻은 결과는 단일 로터와 다중 로터 구성에 대한 실험 결과와 고충실도 분석를 이용하여 비교 및 검증이 수행된다. 그런 이후, 제어기 및 동적 특성과 같은 구성 요소에 대한 검증이 수행된다. 해당 검증을 통해 얻어진 결과를 바탕으로 제안된 비행 시뮬레이션이 비행 실험 결과와 비교된다. 특히, 도심 환경을 모사한 돌풍 실험은 현재 시뮬레이션을의 정확성을 평가하는 데 사용하였다. 또한 강체 블레이드 플랩핑, 공기역학적 간섭, 그리고 돌풍 강도에 대한 영향들이 조사 및 분석되었다. 이를 통해 무인 항공기의 동적 거동을 추정하기 위해 적합한 로터 공기역학 해석기법이 중요한 고려사항임을 확인하였다.